

2018

High-density microfibers as a deep brain bidirectional optical interface

<https://hdl.handle.net/2144/32998>

"Downloaded from OpenBU. Boston University's institutional repository."

BOSTON UNIVERSITY
SCHOOL OF MEDICINE

Dissertation

**HIGH-DENSITY MICROFIBERS AS A DEEP BRAIN
BIDIRECTIONAL OPTICAL INTERFACE**

by

L. NATHAN PERKINS

B.A., University of Southern California, 2007
M.S., Massachusetts Institute of Technology, 2011

Submitted in partial fulfillment of the
requirements for the degree of
Doctor of Philosophy

2018

© 2018 by
L. NATHAN PERKINS
All rights reserved

Approved by

First Reader

David A. Boas, PhD
Professor of Biomedical Engineering
Professor of Electrical and Computer Engineering

Second Reader

Timothy J. Gardner, PhD
Associate Professor of Biology

Third Reader

Thomas Bifano, PhD
Professor of Mechanical Engineering
Professor of Materials Science and Engineering
Professor of Biomedical Engineering

Homo sapiens is the species that invents symbols in which to invest passion and authority, then forgets that symbols are inventions.

Joyce Carol Oates

Acknowledgments

The research presented here was only possible due to the support and contributions of many. I am especially grateful to all my colleagues and collaborators at both the Laboratory of Neural Circuit Formation and the Bio Optical & Acoustic Spectroscopy Lab. Both labs provided close knit and collaborative environments; fellow researchers lent expertise, guidance and moral support that helped advance this work. A few lab members directly contributed to the experiments, surgeries and research steps described in this thesis—specifically Dawit Semu, Kivılcım Kılıç, Jun Shen, Blaire Lee and Will Liberti—and I am grateful to have worked alongside each of them.

The faculty members throughout the University were an amazing resource, and I am appreciative of how willingly professors gave their time and knowledge. Tim Gardner lay the groundwork for this research and provided the inspiration for the techniques introduced in the thesis; he indulged my diverse research interests and provided a lab environment where I felt both intellectually challenged and encouraged. David Boas helped me bring this research to conclusion by filling in modeling and experimental gaps; his commitment to seeing progress and brainstorming next steps helped advance my work. In addition to my advisors, my committee and other faculty members provided valuable support and mentorship—I am especially appreciative of the contributions of Ian Davison and Janusz Konrad.

I'm also grateful to the larger Graduate Program of Neuroscience and BU community, especially Sandi and Shelley, who were always available and supportive.

Finally, I am continually in awe and appreciative of the support I receive from my family—Penny and Bill—and my partner—Tommy. To each of them, thank you!

— Nathan

HIGH-DENSITY MICROFIBERS AS A DEEP BRAIN BIDIRECTIONAL OPTICAL INTERFACE

L. NATHAN PERKINS

Boston University School of Medicine, 2018

Major Professor: David A. Boas, PhD
Professor of Biomedical Engineering
Professor of Electrical and Computer Engineering

ABSTRACT

Optical interrogation and manipulation of neural dynamics is a cornerstone of systems neuroscience. Genetic targeting enable delivering fluorescent indicators and opsins to specific neural subpopulations. Optic probes can fluorescently sense and convey calcium, voltage, and neurotransmitter dynamics. This optical toolkit enables recording and perturbing cellular-resolution activity in thousands of neurons across a field of view.

Yet these techniques are limited by the light scattering properties of tissues. The cutting edge of microscopy, three-photon imaging, can record from intact tissues at depths up to 1 mm, but requires head-fixed experimental paradigms. To access deeper layers and non-cortical structures, researchers rely on optical implants, such as GRIN lenses or prisms, or the removal of superficial tissue.

In this thesis, we introduce a novel implant for interfacing with deep brain regions constructed from bundles of hundreds or thousands of dissociated, small diameter ($<8\ \mu\text{m}$) optical fibers. During insertion into the tissue, the fibers move independently, splaying through the target region. Each fiber achieves near total internal reflection,

acting as a bidirectional optical interface with a small region of tissue near the fiber aperture.

The small diameter and flexibility of the fibers minimize tissue response, preserving local connectivity and circuit dynamics. Histology and immunohistochemistry from implants into zebra finch basal ganglia (depth 2.9 mm) show the splaying of the fibers and the presence of NeuN-stained cells in close proximity to the fiber tips.

By modeling the optical properties of the fibers and tissue, we simulate the interface properties of a bundle of fibers. Overlap in the sensitivity between nearby fibers allows application of blind source separation to extract individual neural traces. We describe a nonnegative independent component analysis algorithm especially suited to the interface.

Finally, experimental data from implants in transgenic mice yield proof of principle recordings during both cortical spreading depolarization and forepaw stimulation.

Collectively, the data presented here paint a compelling picture of splaying microfibers as a deep brain interface capable of sampling or perturbing neural activity at hundreds or thousands of points throughout a 3D volume of tissue while eliciting less response than existing optical implants.

Contents

Acknowledgments	v
Abstract	vi
1 Introduction	1
1.1 Background	2
1.1.1 Optical techniques	2
1.1.2 Interface technology	5
1.1.3 Accessing deep brain regions	8
1.2 Proposed Solution	9
2 Histology of implanted optical microfibers shows consistent splaying throughout the target region, with minimal tissue response	11
2.1 Introduction	11
2.2 Methods	14
2.2.1 Fibers	14
2.2.2 Histology	16
2.2.3 Modeling	21
2.2.4 Fluorescent beads	23
2.3 Results	24
2.3.1 Histology	24
2.3.2 Modeling	30
2.3.3 Fluorescent beads	36
2.4 Discussion	36

3	Extracting individual neural activity recorded through splayed optical microfibers	42
3.1	Introduction	42
3.2	Methods	44
3.3	Results	49
3.4	Discussion	62
4	In vivo recordings show calcium dynamics recorded via splaying optical microfibers	66
4.1	Introduction	66
4.2	Methods	68
4.2.1	Fibers	68
4.2.2	Surgery	69
4.2.3	Recording	70
4.2.4	Analysis	72
4.3	Results	73
4.4	Discussion	77
5	Interface and software for near-real-time processing and feedback	82
5.1	Introduction	82
5.2	Methods	83
5.2.1	Chronic fiber interface	83
5.2.2	Acquisition hardware	86
5.2.3	Near-real-time software	86
5.2.4	Analysis pipeline	90
5.3	Results	91
5.3.1	Chronic fiber interface	91
5.3.2	Analysis performance	91

5.4	Discussion	93
6	Conclusions	97
6.1	Splaying optical microfibers as an interface	97
6.2	Future work	99
6.2.1	Additional in vivo recordings	99
6.2.2	Controlling implant and splay	100
6.2.3	Stimulation and structured illumination	100
6.2.4	Multiplexing	101
6.2.5	Head mounted optics	102
	References	105
	Curriculum Vitae	116

List of Figures

2·1	Diagram of bundle of microfibers as an optical interface.	15
2·2	Histology showing microfibers splayed throughout target region. . . .	25
2·3	Diameter of fiber splay as a function of fiber count and depth.	27
2·4	Histology showing microfibers at different implant depths.	28
2·5	NeuN and DAPI staining of tissue at fiber implant tips.	29
2·6	Distribution of distance from fiber to NeuN-stained cell.	31
2·7	Profile of single fiber.	33
2·8	Distribution of neurons accessible via fiber bundle.	34
2·9	Recording of diffusing fluorescent beads via fiber bundle.	37
3·1	Diagram of optics and fiber interface	50
3·2	Comparison of light profile with model results	51
3·3	Modeled distribution of fibers and neurons	53
3·4	Effect of fiber count on number of neurons contributing signal	54
3·5	Contribution of neurons to fiber in descending order	56
3·6	Contribution of neuron to fibers in descending order	57
3·7	Application of source separation to simple model	58
3·8	Fraction of accurately matched signals across parameters	60
3·9	Performance of source separation on threshold crossing task	61
4·1	Recording of FITC in vasculature	74
4·2	Recording of fluorescence during CSD	75
4·3	Images of fiber bundle during CSD	76

4.4	Recording of fluorescence during forepaw stimulation	78
5.1	Polyimide to reinforce fiber bundle	84
5.2	Commutator for awake behaving recording	85
5.3	Software for capture and near-real-time analysis	88
5.4	Latency for video processing	92
5.5	Latency for audio processing	94
6.1	Miniature microscope	103

List of Abbreviations

ACSF	Artificial Cerebrospinal Fluid
AST	Abstract Syntax Tree
AUC	Area Under the Curve
BMI	Brain Machine Interface
BSA	Bovine Serum Albumin
CDF	Cumulative Density Function
CMOS	Complementary Metal-Oxide-Semiconductor
CNR	Contrast-to-Noise Ratio
CSD	Cortical Spreading Depolarization
CSF	Cerebrospinal Fluid
CSV	Comma Separated Values
DMD	Digital Micromirror Device
DPH	Days Post Hatch
FFT	Fast Fourier Transform
FITC	Fluorescein Isothiocyanate
FPS	Frames Per Second
GECI	Genetically Encoded Calcium Indicator
GFP	Green Fluorescent Protein
GRIN	Gradient-Index
IACUC	Institutional Animal Care and Use Committee
ICA	Independent Component Analysis
IV	Intravenous
LED	Light Emitting Diode
NA	Numerical Aperture
PBS	Phosphate Buffered Saline
PCA	Principal Component Analysis
ROC	Receiver Operating Characteristic
ROI	Region of Interest
SIFT	Scale-Invariant Feature Transform
SNR	Signal-to-Noise Ratio
STFT	Short-Time Fourier Transform
TTL	Transistor-Transistor Logic
USB	Universal Serial Bus

Chapter 1

Introduction

Optical techniques have been a pivotal tool in the process of observing and manipulating neural activity, achieving a stable interface for interacting with cells over a large field of view, thanks in large part to the genetic probes that enable resolving individual neural contributions (Emiliani et al., 2015). Novel genetic probes, such as voltage indicators, are only broadening the questions that can be answered via optical techniques by achieving greater temporal resolution and revealing subthreshold activity (Gong et al., 2015).

Despite these strengths, optical techniques are severely constrained by light scattering. In response to the limitations of scattering, a number of innovative approaches have been developed, with varying tradeoffs in terms of quality and feasibility. Multi-photon microscopy techniques enable imaging up to 1 mm below the surface, but require animals to be head-fixed and hence limit behavior paradigms (Horton et al., 2013). Attempts to adapt multi-photon microscopy to freely behaving animals have achieved neither the stability nor the ease of implementation desired (Helmchen et al., 2001; Flusberg et al., 2005).

Alternatively, more superficial brain regions can either be removed (Dombeck et al., 2010) or circumvented by implanting an optical probe, such as a GRIN lens (Barretto et al., 2009), a microprism (Andermann et al., 2013) or a communications-grade optical fiber for fiber photometry (Guo et al., 2015). These techniques can be effective (Betley et al., 2015), but damage superficial tissue and limit imaging to a

planar cross-section of the desired brain region.

In this thesis, we propose using bundles of splaying microfibers as a new optical interface, which has the potential to provide a high channel count, minimally invasive, stable, bidirectional optical interface for deep brain regions. The thesis is organized as follows: first, in chapter 1, we briefly review existing optical methods and associated tradeoffs, framing the role of the splaying optical microfibers in the larger methodological landscape. Second, in chapter 2, we describe the implant in detail and histologically evaluate the implant, assessing both the splaying properties of the bundles and the presence of neurons in close proximity to the fibers. Next, we describe optical models of both the individual fibers and the interface properties of the bundles in chapter 3. In chapter 4, we describe initial in vivo applications of the interface and show fluorescence data recorded through the fibers. Finally, in chapter 5, we describe peripheral developments (both hardware and software) that enable application of the technique in longitudinal experimental work.

1.1 Background

1.1.1 Optical techniques

Due to advantages inherent to optical techniques for recording and manipulating neural activity, these techniques have become indispensable to advancing systems neuroscience. Specifically, optical methods allow sensing and perturbing neural activity at a cellular spatial resolution and, due to new indicators, at a sub-action potential temporal resolution. In addition, optical techniques can be deployed in long-term experiments to track cellular dynamics over time in awake behaving animals, allowing directly probing the circuits relevant to complex behaviors.

Probes and indicators. Crucial to the success of optical techniques are the development of genetically encoded probes. These proteins enable optically interfacing

with existing cells.

One of the earliest and most pervasive probes is GCaMP, a combination of green fluorescent protein (GFP) isolated in jellyfish, and a calcium binding chain. When calcium binds to the protein, conformational changes in the chain alter the efficiency of the fluorescent protein and, as a result, increase its fluorescence (Nakai et al., 2001; Barnett et al., 2017). By illuminating cells expressing such a probe with the excitation wavelength and measuring the fluorescent emissions, it is possible to sense changes in intracellular calcium and, hence, the calcium-mediated depolarization associated with action potentials. Subsequent iterations on the protein have increased its efficiency, speed and brightness (Chen et al., 2013).

The capacity to measure intracellular calcium enables inquiries into a range of signaling and encoding questions, but also is inherently limited to suprathreshold cellular dynamics. New probes are being developed to sense other dimensions of cellular activity, including pH indicators, neurotransmitter indicators and voltage indicators (Lin and Schnitzer, 2016). Voltage indicators have tremendous potential to allow visualizing both subthreshold and suprathreshold cellular dynamics at high temporal resolutions (Han et al., 2013; St-Pierre et al., 2014; Gong et al., 2015). But given the highly localized voltage differentials (only present at the cell membrane) and the much shorter time course of voltage fluctuations, these probes must be more precisely localized and much brighter to enable high frame rate acquisition and detection.

In addition to sensing other cellular dynamics, new fluorophores are being developed and deployed that leverage the potential to multiplex signals across wavelengths. For example, calcium and voltage indicators are being developed that use red or near-infrared fluorophores (Tischbirek et al., 2015; Dana et al., 2016). Such new fluorophores offer the potential to multiplex signals across non-overlapping wavelengths: this can enable sensing two properties simultaneously (e.g., calcium and voltage),

or can enable sensing from two subpopulations simultaneously, or can enable both sensing and modulating activity simultaneously. In addition to the ability to multiplex signals across wavelengths, new fluorophores can extend optical access to deeper brain regions by moving to wavelengths with lower absorption (Tischbirek et al., 2015; Dana et al., 2016).

Beyond sensing, novel genetic probes enable manipulating neural activity. Starting with Channelrhodopsin-1 (Nagel et al., 2002), which encodes a light-gated photon channel derived from the phototaxis mechanism in green algae, such probes have enabled modulating the excitability and membrane potential of neurons through controlled exposure to specific excitatory wavelengths (Boyden et al., 2005; Deisseroth et al., 2006; Yizhar et al., 2011).

Genetic targeting. All of these fluorescent probes and light gated channels are genetically encoded, which allows for precise targeting and expression of the protein in specific neural subpopulations of living animals. Transgenic animals are available with expression in cell types of interest, while new viral vectors enable targeting expression in neurons based on connectivity (Tervo et al., 2016). New techniques, such as relying on immediate early genes, allow targeting expression to those neurons involved in specific circuits and memories (Liu et al., 2012). All of these advances in genetic targeting enable precisely interfacing with a narrowly defined neural population, allowing researchers to interrogate the dynamics relevant to a specific behavior or circuit.

Field of view. Optical interrogation and manipulation of neural circuits offers a number of additional advantages beyond the probes and targeting flexibility. One of the big advantages is the ability to interface with neurons over a large field of view, providing simultaneous access to thousands of neurons (Mohammed et al., 2016).

New iterations have scaled this up to hemisphere- or skull-sized imaging windows, exposing millions of neurons (Kim et al., 2016). Through the large field of view, optical techniques provide the ability to track information encoding or behavioral modulation throughout a region or across regions, providing a more holistic vantage of the neural activity. Of course, with this breadth of data, new analysis challenges emerge, as it becomes more difficult to identify the salient activity.

Longitudinal access. Optical access not only achieves a large spatial field of view, it also enables long term tracking of individual neurons. Cells can be tracked across days to understand how neural encoding and activity changes with time. For example, recording calcium activity in the song bird premotor area exposed instability in neural encoding (Liberti III et al., 2016) that was not visible in previous electrophysiology experiments, where single cells can often only be tracked on the scale of hours (Hahnloser et al., 2002).

Awake behaving experiments. This goes hand-in-hand with the longitudinal access, but it is worth explicitly emphasizing that optically interfacing with the brain does not preclude awake behaving experiments. Many interface technologies, discussed in the next section, allow recording animals in freely behaving paradigms. In the song bird example just mentioned, this ability to record neural activity in freely behaving animals is crucial, as the birds will rarely sing if constrained (Liberti III et al., 2017).

1.1.2 Interface technology

The last section identified a range of genetically encoded probes that enable optical access to neural activity. A complimentary area of technology development has focused on the hardware and techniques for recording or stimulating the described

probes. There are a number of techniques used to precisely interface with the neurons in question, each of which achieves different tradeoffs in terms of sensitivity, signal localization and experimental constraints. We highlight three widely used technologies below.

Multi-photon microscopy. Multi-photon microscopy provides powerful and precise access to fluorescent indicators, achieving greater precision in the depth axis through two-photon absorption and improving penetration by exciting with higher wavelength light (Xu et al., 1996). In addition, the two-photon absorption decreases the amount of excitation light required, reducing the chance of bleaching (Denk et al., 1990). Three-photon microscopy further builds on these principles, achieving greater penetration, allowing imaging indicators at depths exceeding 1 mm (Horton et al., 2013; Wang et al., 2017).

Despite these strengths, multi-photon microscopy faces key constraints. Given the expenses associated with constructing and maintaining a two-photon microscope, there are substantial fixed costs and few labs have the capacity to run simultaneous experiments. In addition, the types of experiments are constrained, often relying on recording in animals that are head fixed. Head-mounted two photon microscopes show potential (Helmchen et al., 2001; Flusberg et al., 2005), but these have not achieved the reliability or stability necessary for widespread use.

Single photon microscopy and miniature microscopes. Single photon microscopy requires more excitation—risking more photobleaching—and does not have the depth penetration or resolution of multi-photon microscopy, but it carries a number of important advantages. Most notably, single photon microscopy can readily be scaled to small applications, allowing recording from freely behaving animals through miniature head-mounted microscopes (Ghosh et al., 2011; Cai et al., 2016; Liberti III

et al., 2017). These setups come with a lower price tag and enable recording animals during less constrained behaviors.

Variations on the standard miniature microscopes are being developed that incorporate some of the advantages of multi-photon microscopy, such as new head-mounted light-field microscopes capable of high speed volumetric imaging (Skocek et al., 2018).

Fiber photometry. Another technology used for optically interfacing with the brain is fiber photometry. The technique relies on using a large diameter (125 μm or more), multi-mode fiber to deliver excitation light and collect fluorescence from a specific region (Adelsberger et al., 2005; Cui et al., 2013; Adelsberger et al., 2014). Such an approach sacrifices the spatial resolution of microscopy for high sensitivity, high temporal resolution bulk recording. For example, it enables recording bulk fluorescence from axonal projections (Gunaydin et al., 2014). Such fiber setups are also frequently used to deliver excitation light to opsins in a target region, in order to modulate neural activity (Warden et al., 2014).

Multi-site fiber photometry has scaled these techniques up to 8–12 fibers, each of which can be implanted in a different site. Collectively, the fibers enable simultaneous recording of bulk fluorescence across brain regions (Guo et al., 2015).

Waveguides and new implant. The three methods above have widespread usage, but there are a number of new approaches being development that combine optical and electrical components to move both illumination and detection to an implantable probe. With such devices, it is possible to use less light power, more easily image large volumes and use waveguides to achieve targeted excitation (Warden et al., 2014; Wu et al., 2015; Segev et al., 2017).

1.1.3 Accessing deep brain regions

The range of optical techniques described in the previous section are widely used to optically record or manipulate neural activity. Yet all of these techniques are constrained by the light scattering and absorption of the brain, which either limits the techniques to more superficial regions or requires more invasive implants to access deep brain regions.

Multi-photon microscopy. Two- and three-photon microscopy achieve greater penetration through use of wavelengths that have lower scattering coefficients in tissue (Wang et al., 2017). This is especially true for three-photon microscopy, that is able to record fluorescent indicator activity from depths exceeding 1 mm. But as stated before, these methods are generally limited to head-fixed experimental paradigms.

Implantable optics. To reach further than is accessible with three-photon microscopy, or to image from a deep brain region in a freely behaving animal, researchers currently rely on implantable optics. Specifically, GRIN lenses (Barretto et al., 2009) and prisms (Andermann et al., 2013) are frequently used to access deeper brain structures.

But as we have learned from an existing body of literature related to electrode development, implants with a cross section greater than 50 μm can cause neuronal damage and death over a region up to 100 μm from the implant (Seymour and Kipke, 2007). The insertion trauma and the motion of the brain relative to the implant after insertion can trigger tissue encapsulation, disruption of oxygenation and excitotoxic cell death (Szarowski et al., 2003; Polikov et al., 2005; McConnell et al., 2009; Freire et al., 2011). Implants that have a small cross section ($<10 \mu\text{m}$) and that are more flexible can avoid this tissue response (Seymour and Kipke, 2006; Harris et al., 2011; Kozai et al., 2012; Patel et al., 2015a). Unfortunately, most optical implants have

diameters exceeding 500 μm (in order to achieve a wide field of view) and are rigid.

As a result, GRIN lenses and other optical implants damage or destroy the tissue in the immediate path and are often encapsulated in glia due to the induced tissue response (Lee et al., 2016). The interface will collect fluorescence activity from neurons just beyond this region of encapsulation. Yet the full impact of the implant is often unknown. Due to dense local connectivity, tissue damaged by the implant and foreign body response can impact network dynamics in the imaging plane (Hayn and Koch, 2015; Hayn et al., 2017; Goss-Varley et al., 2017).

Tissue removal. Another approach worth mentioning, but sharing many of the limitations of optical implants, is removal of superficial tissue (Dombeck et al., 2010). By removing superficial tissue, it is possible to directly access the region of interest and apply standard imaging techniques (such as a head-mounted microscope or multiphoton imaging). But the contribution of superficial regions and local connectivity are both jeopardized or obliterated in such an approach.

1.2 Proposed Solution

In order to translate the benefits inherent in superficial imaging techniques, such as long-term stability, high-channel counts and minimal tissue damage, to deep brain regions, we propose the use of arrays of dissociated optical microfibers that can be implanted in brain tissue. The principle of these optical fibers is based on self-splaying carbon fiber microthread arrays developed for electrophysiology (Guitchounts et al., 2013; Markowitz et al., 2015). The optical fiber bundles contain hundreds or thousands of multimode optical microfibers as small as 6.8 μm in diameter, displacing significantly less brain tissue as compared with existing optical fiber implants. As each fiber travels independently and finds a path of least resistance, the fibers separate and splay, expanding the potential recording area while minimizing tissue damage. Each

fiber maintains near total internal reflection, allowing the fiber to optically interface with genetically encoded indicators and probes in the tissue surrounding the fiber aperture.

The fibers are constructed by sourcing commercial leached fiber bundles produced as flexible endoscopes, which are composed of thousands of small diameter glass microfibers, where each fiber has a low index of refraction cladding for light confinement. By cutting the fiber bundle in half, we gain access to the individual fibers, which can be directly implanted into the tissue. Outside of the brain, the fibers converge to a polished imaging surface where the fibers are arranged in a tight lattice that can be mounted under a traditional fluorescence microscope objective.

This approach achieves a number of the usual advantages of optically interfacing with tissue, while foregoing the substantial tissue impact associated with large, monolithic implants such as GRIN lenses. By implanting hundreds or thousands of optical microfibers, it is possible to record or stimulate neurons over a large region of tissue. Given that the fibers splay during insertion, a bundle can spread out over 1 mm at a depth of 3 mm, sampling fluorescent activity over a large 3D volume. Because each fiber is flexible and has a small cross section, the individual fibers will not have the same impact as a larger, more rigid implant, preserving more of the local connectivity and network dynamics. Finally, because each fiber has near total internal reflection, it will deliver excitation light to and collect fluorescence from a small amount of tissue near the fiber aperture.

Bundles of optical microfibers have the potential to extend multichannel, bidirectional optical techniques to deeper brain regions without having to remove or obliterate the adjacent brain regions. In the next chapter, we present a more detailed description of the fibers and review histological evidence showing the distribution of fibers in tissue and the presence of neurons in close proximity to the fiber tips.

Chapter 2

Histology of implanted optical microfibers shows consistent splaying throughout the target region, with minimal tissue response

2.1 Introduction

Optical techniques for recording and manipulating neural activity play a crucial role in advancing systems neuroscience, due to the broad field of view, the flexibility and specificity of viral and genetic targeting, and the development of novel probes offering non-overlapping spectral bandwidth and increasing temporal resolution (Emiliani et al., 2015; Gong et al., 2015).

Yet these techniques are inherently limited in all but the most superficial regions of the brain, given the light scattering and absorption of tissue. New developments are helping to extend such optical techniques to deeper brain regions, but necessitate tradeoffs in terms of either more constrained experimental paradigms or increased tissue damage. Three-photon microscopy at 1300 nm has enabled recording from intact brain tissue at depths exceeding 1 mm (Horton et al., 2013; Wang et al., 2017). And while three-photon microscopy is not yet amenable to recording in freely behaving animals, head-mounted two-photon microscopes show promise, but are limited to depths on the order of the mean free path of near infrared photons in the brain, just a few hundred microns (Zong et al., 2017). Greater penetration depths are now

being achieved with red-shifted fluorophores (Dana et al., 2016). At depths beyond the reach of three photon imaging, optically interfacing with deeper layers and non-cortical structures has relied on implanting miniature gradient index (GRIN) lenses or prisms (Jung et al., 2004; Barretto et al., 2009; Andermann et al., 2013; Cui et al., 2013), or removing overlying tissue (Dombeck et al., 2010). Such techniques provide optical access, but compromise or obliterate structures adjacent to the area being imaged.

Implants with a cross section greater than 50 μm cause neuronal damage or death over a zone up to 100 μm from the implant (Seymour and Kipke, 2007); the trauma of insertion and motion of the implant after insertion trigger a range of reactions including the immune foreign-body response to non-organic material, the disruption of oxygenation due to vessel damage, the breakdown in the blood-brain barrier, and excitotoxic cell death associated with accumulation of extracellular glutamate (Szarowski et al., 2003; Polikov et al., 2005; McConnell et al., 2009; Freire et al., 2011). Due to dense local connectivity, tissue damaged by the implant and foreign body response could impact network dynamics in the imaging plane (Hayn and Koch, 2015; Hayn et al., 2017; Goss-Varley et al., 2017). Yet implants with a cross section less than 10 μm have a substantially diminished tissue response (Seymour and Kipke, 2007; Seymour and Kipke, 2006; Kozai et al., 2012; Patel et al., 2015a).

We propose a new technique to optically address deep brain regions through sub-10 μm implants. The basic idea is to cut commercially available leached fiber bundles (Gerstner et al., 2004), revealing the dissociated fibers, which can then be implanted. In this process, hundreds or thousands of multimode optical microfibers each with a diameter as small as 6.8 μm are implanted into the brain while the back end of the device provides optical access to the fibers. During the implant process, each fiber travels independently and finds a path of least resistance causing the implanted bundle

to spread gradually. The small diameter of the fibers minimizes tissue displacement and decreases the likelihood both of evoking a tissue response and, as a result, of disrupting local network dynamics in the imaging plane.

In the approach described here, each fiber has a core and a cladding. The refractive index mismatch achieves near total internal reflection of light, enabling each fiber to interface with tissue near its aperture. Because of the splaying during insertion, the fibers will not maintain a strictly organized spatial mapping. Yet each fiber may provide a bidirectional interface with a small volume of tissue near the tip of the fiber, and potential correlations across fibers can enable reconstructing a relative spatial topography. Outside of the brain, the fibers converge to a polished imaging surface, where each fiber is arrayed in a tightly packed lattice that can interface with a traditional fluorescence microscope.

Based on histology and immunohistochemistry, we demonstrate that the bundles of optical microfibers splay during insertion into the brain, achieving a spatially distributed set of fibers throughout the target brain region. The small cross section of the individual fibers displaces less tissue than GRIN lenses (for example, a bundle of 2,000 fibers displaces half the volume of a 500 μm diameter lens), and hence may preserve more neurons and promote more natural network dynamics in the target region. Based on simulations of the optical profile of individual fibers, we assess the sensitivity of the fibers as a multi-channel, bidirectional optical interface. Finally, we show that fluorescence signals can be recorded from diffusing fluorescent beads through these small-diameter optical microfibers.

2.2 Methods

2.2.1 Fibers

The fibers we use are leached fiber bundles produced as flexible medical endoscopes. This work primarily relied on bundles of 4,500 fibers where each individual fiber has a diameter of 8 μm (Schott 1534180), although variations exist in the number of fibers (3,500–18,000) and the diameter (6.4–11.9 μm). The bundles are built for coherent imaging and constructed from three types of glass, a core (diameter: 5.1 μm , refractive index: 1.605), a cladding (thickness: 1 μm , refractive index: 1.56) and an acid soluble glass (thickness: 0.4 μm). The bundles are manufactured as traditional coherent fibers, and then the acid soluble glass is dissolved for bundle flexibility (Gerstner et al., 2004). The ends of the fibers come together in polished imaging surfaces held in ferrules. The dissociated fibers are covered in a flexible silicone sheathing.

We cut the bundles in half, using a scalpel or razor, sacrificing the spatial cohesion, but providing access to the individual, dissociated fibers. The silicone sheathing was cut back to expose the fibers, and we then cut a fraction of the exposed fibers to reduce the implant size to a target number of fibers (varied over implants to assess tissue impact). The remaining fibers were secured together by forming a bead of light-cured acrylic (Flow-It ALC, Pentron Clinical) around the fibers, leaving 4–5 mm of fibers exposed (Figure 2.1b). The exposed fibers could be further shaped using fine scissors, creating a bevel. Such pre-implant shaping increases the distribution of depths of the fiber tips. At this point, the dissociated fibers can be directly implanted into brain tissue; the other end of the fiber, containing the ferrule and polished surface with fibers aligned and arranged in a lattice, can be readily interfaced with a fluorescence microscope or other optical configuration (Figure 2.1).

Optical attenuation of the fibers was measured to be 3.38 ± 0.03 dB (std. dev.) for a 840 mm long bundle (4 dB/m). Attenuation was measured using collimated

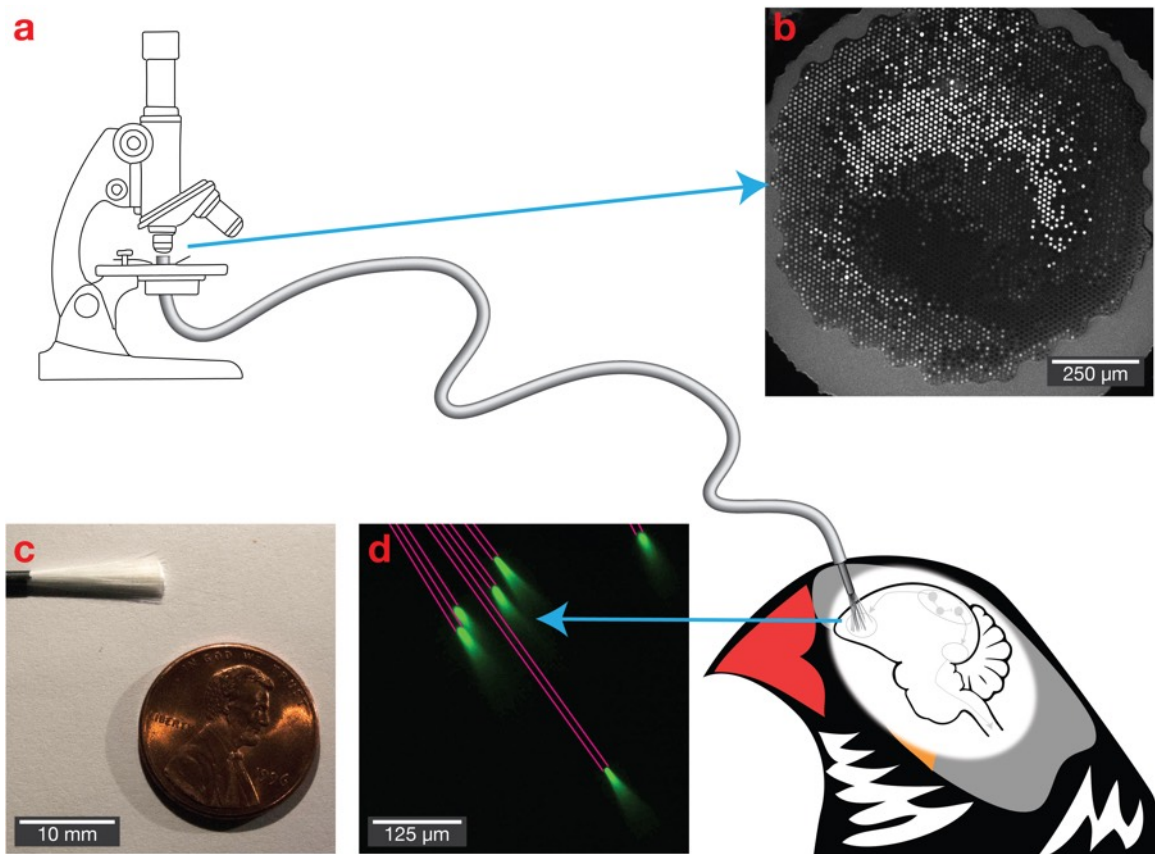


Figure 2-1: Bundles of microfibers as a potential deep brain optical interface. (a) The polished imaging surface is mounted in a traditional fluorescence microscope, while individual fibers with a diameter as small as $6.8\ \mu\text{m}$ are implanted into the brain. (b) The polished imaging surface that connects with the microscope. (c) A bundle of 18,000 fibers. (d) Light propagates with near total internal reflection, allowing it to deliver and collect light at the tips of the fibers. Six fibers are shown in a fluorescein solution, with pink lines added to emphasize fiber path.

light in the 446–486 nm range (relevant for exciting GFP-based indicators, such as GCaMP, or stimulating channelrhodopsin) focused on the polished imaging surface using a lens with numerical aperture matched to the fibers. In this measurement, we assumed that 19.4% of the incident light enters the cores based on the surface area of the fiber bundle, the fiber count, and the core diameter. After cutting the bundle, attenuation for the 420 mm bundle measured from the splaying fibers is 3.78 ± 0.02 dB (std. dev.), indicating that most of the light carried by the bundle is transmitted from the cut ends.

2.2.2 Histology

Animals. Animal care and experimental procedures were approved by the Institutional Animal Care and Use Committee (IACUC) of Boston University (protocols 14-028 and 14-029). Fibers were implanted in 27 adult zebra finches (> 120 days post hatch). Of the animals, eight were implanted with alternative fibers (different materials and different fiber diameters; results not shown). Of the remaining nineteen, fifteen were used for histology described in this chapter with four animals being excluded due to poor slicing (tearing of the tissue when slicing through the fibers) or poor staining (during immunohistochemistry).

Fiber implant. Anesthesia was induced with 4% isoflurane and maintained at 1–2% for the duration of the surgery. An analgesic (0.5 mg/kg meloxicam, Eloxiject) was injected intramuscularly into the breast at the start of the procedure. The animal was placed in a stereotaxic instrument and feathers were removed from the scalp. The scalp was cleaned with Betadine and ethanol. A local anesthetic (4 mg/kg bupivacaine) was injected subcutaneously into the scalp, and an incision was made along the anterior-posterior axis.

The skull over the implant point (area X) was localized based on head angle

(20°) and stereotactic coordinates (5.8 mm anterior, 1.5 mm lateral). In order to accommodate the bundle of fibers, a 0.5–1 mm diameter craniotomy was created, with the size matched to the bundle. The craniotomy was created by first using a dental drill to remove the outer layer of bone, then by using an ophthalmic scalpel to remove the inner layer of bone (Long et al., 2010). The dura within the craniotomy was removed using either a dura pick constructed from sharpened tungsten or an ophthalmic scalpel.

The fiber bundle was prepared by securing the fibers together in a bead of light-cured dental acrylic (Flow-It ALC, Pentron Clinical) and cut to 3–5 mm. Using a digital manipulator attached to the stereotaxic rig, the fiber bundle was positioned over the durotomy and slowly lowered into the tissue at a rate of approximately 500 μm per minute. The insertion rate varied based on the number of fibers and visual inspection of the tissue surrounding the implant. Larger implants (more than 250 fibers) could result in a noticeable depression or “dimpling” in the tissue before the bundle passed through the surface of the brain. Such dimpling was generally observed during the first 250–350 μm of insertion; beyond that depth, the size of the depression remained consistent as we continued to lower the implant. We found that the visible dimpling could be alleviated by lowering the implant an additional 50 μm past the desired depth, waiting for five minutes, then returning the implant to the desired depth. We did not observe bleeding associated with the implant or the dimpling. After the fibers were lowered to a depth of 2.7–2.9 mm (measured from the point when the fibers enter the tissue), additional light-cured dental acrylic was used to secure the fiber bundle to the skull surrounding the craniotomy.

Animals received nonsteroidal anti-inflammatories (0.5 mg/kg meloxicam) both before the surgery via injection (Eloxiject) and after the surgery in their food (Metacam), as well as topical antibiotics (Pfizer Terramycin) after the surgery.

Three days post implant, animals were returned to the aviary and housed socially. Animals used to image the distribution of fibers were perfused after 21 to 331 days (mean 88 days). Animals used for immunohistochemistry staining were perfused after 77 to 395 days (mean 176 days).

Animal perfusion and fixation. Animals were injected with 0.1 mL 10% sodium pentobarbital intramuscularly. Once anesthetized, the animals were perfused intracardially with phosphate-buffered saline (PBS) followed by 4% paraformaldehyde in 0.1 M PBS. The skull and brain were separated from the body. Leaving the skull in place (as the fibers are anchored to the skull), small cracks were made in the bone to ensure penetration of the fixative. The skull and brain was immersed in 4% paraformaldehyde in 0.1 M PBS overnight. Next, as cryoprotection, it was immersed in 15% sucrose in 0.1 M PBS overnight, followed by 30% sucrose in 0.1 M PBS for a second night. Placing the skull upside down such that the implant trajectory was roughly perpendicular to the mounting slide, the skull was frozen (-20°C) in embedding medium (Optimal Cutting Temperature Compound, Tissue-Tek) for 30 minutes and sectioned in a cryostat (Leica CM3050S, with Thermo Scientific MB22 microtome blades) in either 70 or 100 μm thick slices, cutting through the skull and perpendicular to the fiber bundle implant. Due to the thin, pneumatized bone of the songbird, cryosectioning through the skull was possible without any decalcifying process. For optimal cutting, blades were regularly shifted and replaced to ensure a fresh cutting surface was always in use; without such precautions, the worn blades were more likely to catch on fibers and tear surrounding tissue. Some sections were discarded because of tearing. Slices were either mounted on slides or were transferred to wells containing PBS and processed for immunohistochemical staining as described below.

Histology. To quantify the splay of fibers, brightfield microscopy images were collected of slices mounted on slides and secured with coverslips. Images were collected from slices at various depths.

Immunohistochemistry. In order to assess tissue health and imaging viability, a selection of slices taken at various depths were processed to label neurons via NeuN antibodies. Slices were washed in PBS, then in 0.3% Triton X-100 in PBS for 30 minutes and finally in a solution of 0.3% Triton X-100 and 5% normal donkey serum (NDS) for 45 minutes. The slices were then placed in a solution of the primary antibody (MAB377 Anti-NeuN, 1:500, EMD Millipore) made with 3% bovine serum albumin (BSA) and 0.3% Triton X-100 in PBS. The wells were placed on a rotator and allowed to incubate at 4°C overnight. Slices were washed in PBS ($\times 3$, 10 minutes each). Next, the slices were placed in a solution of the secondary antibody (715-025-150 Rhodamine [TRITC] AffiniPure Donkey Anti-Mouse IgG, 1:500, Jackson ImmunoResearch). The wells were again placed on a rotator and allowed to incubate at 4°C for one hour. Slices were washed in PBS ($\times 3$, 10 minutes each). Next, 1 mL of DAPI stain (4',6-Diamidino-2-Phenylindole, Dihydrochloride, 300 μ M solution, 1:1000, D1306, Thermo Fisher Scientific) was added to each well. After three minutes, the slices underwent a final wash ($\times 2$, 5 minutes), before being mounted on glass slides with an anti-fading mounting medium (Fluoro-Gel, EMS) and secured with a coverslip. Some immunohistochemistry samples were not usable, due to ineffective staining or fibers becoming dislodged during the washing process.

Microscopy. Slices were imaged using an upright fluorescence microscope (Nikon Eclipse NiE, with a DS-Qi1 Monochrome camera and controlled by NIS-Elements: Advanced Research), illuminated by an LED light source (SOLA Light Engine). To assess splay, we used either a 4 \times (Plan Fluor, NA 0.13) or a 10 \times (Plan Fluor, NA

0.3) objective. To image immunohistochemistry, we used a 20 \times objective (Plan Apo Lambda, NA 0.75).

Qualitative and quantitative analysis. To quantify fiber splay, brightfield images were collected from slices near the tip of the fiber. Fibers were manually annotated using a custom MATLAB program for organizing and analyzing histology. To calculate a measure indicative of the splay of the fibers, a bivariate normal distribution was fit to the position of the fibers in the slice and the area of the ellipse representing two standard deviations of the distribution (the 95% confidence interval) was calculated. The data presented are from 11 animals, reflecting the animals implanted with bundles consisting of 7–8 μm diameter fibers with at least a three week recovery period and where the tissue at the tip of the implant was cleanly sliced (see note above about sectioning).

To quantify the presence of neurons in proximity to fibers, two-channel fluorescence (with NeuN in red and DAPI in blue) and brightfield images were collected from the target implant region (area X). Control images were collected from the contralateral region (without an implant) to measure baseline neural distributions and densities. Neurons were manually annotated based on a consensus of the NeuN and DAPI signal, and fibers were manually annotated based on both the histology and brightfield images. For slices with fibers, the distance from each fiber to the nearest neuron was calculated (fibers where the edge of the image was closer than the nearest neuron were ignored), subtracting the radius of the fiber. As a control, random points were selected on the control slices without fibers, and the distance to the nearest neuron was calculated (points could be selected at or on neurons, resulting in a distance of zero).

In addition, NeuN-stained cell density was calculated for the 50 μm region surrounding each implant, normalized by densities calculated on the control slices. To

account for the close proximity of neighboring fibers, the cross sectional area of neighboring fibers was subtracted from the area of the 50 μm region when calculating density surrounding implants. The data presented are based on twelve annotated slices from five animals, reflecting all animals implanted with bundles of 7–8 μm diameter fibers with at least a ten week recovery period and successful immunohistochemical staining.

2.2.3 Modeling

Fiber profile. The optical profile for a single fiber was generated via a Monte Carlo simulation of 10,000,000 photon packets traveling through a 1 mm^3 volume (modeled as isotropic 5 μm voxels) (Boas et al., 2002). Photon packets enter the tissue at [500 μm , 500 μm , 200 μm] with a Gaussian distribution reflecting the NA of the fiber (0.377). Within each voxel, the photon packet can be scattered ($\mu_s = 10 \text{ mm}^{-1}$ with anisotropy $g = 0.9$ (Yi and Backman, 2012)) or fractionally absorbed ($\mu_a = 0.337 \text{ mm}^{-1}$ for 490 nm light, $\mu_a = 0.343 \text{ mm}^{-1}$ for 512 nm light based on 3% blood volume fraction [BVf] (Bouchet et al., 2010), 15 g/DL hemoglobin concentration (Raabe et al., 2011), an oxygenation fraction of 70% and extinction coefficients for hemoglobin (Kollias and Gratzner, 1999)). The 3D path of each photon packet is averaged together, normalized and visualized as a 2D slice through the volume. The fluorescence signals received by individual fibers, given the illumination profile from the superposition of the optical profiles emitted from all of the fibers, is calculated following the procedure described in (Hillman et al., 2004; Burgess et al., 2008).

Neural interface simulation. To simulate interfacing with a neural population, a 1.2 mm^3 volume of tissue was modeled. This volume is consistent with area X in the adult zebra finch (Bottjer et al., 1985) and is illustrative of a deep brain region. A target subpopulation of neurons of interest is modeled as uniformly distributed

through the volume with a density of 780,000 neurons per mm^3 , based on the density of medium spiny neurons in area X in male zebra finch that are one year old (Kosubek-Langer et al., 2017). All cells in the target subpopulation are assumed to express the relevant genetic probe.

Based on the histological data on splaying, the fiber bundle is assumed to have a bivariate normal distribution in xy space with standard deviation (σ) based on the number of fibers in the bundle. The fiber depth will vary based on preparation of the bundle (how the fibers are cut prior to implant) and the path of splay; this variability is modeled as a normal distribution of depths with standard deviation $\sigma = 30 \mu\text{m}$.

The strength of stimulation or excitation for individual neurons is calculated for each fiber by identifying the sensitivity of the voxel that corresponds with the position of the neuron relative to the tip of the fiber. The per fiber optical intensities are summed across all fibers in the bundle to calculate the total potential stimulation/excitation strength. These values are normalized as a percentage of maximum fluence in the tissue.

To evaluate the ability to uniquely address neurons through illuminating a subset of n fibers, a 20,000 iteration Monte Carlo simulation is used to select random permutations of n fibers. For each iteration, the number of neurons activated by the cumulative optical power of the selected fibers is compared with the number of neurons activated if each fiber was illuminated independently.

The round-trip fluorescence yield for pairs of fibers and neurons, a measure of expected fluorescent emission collected by the fiber from the neuron, is calculated by multiplying the total excitation strength for the neuron (as described above) by the sensitivity of the voxel that corresponds with the position of the neuron relative to the tip of the fiber (representing the time reversal of emission from the neuron reaching the fiber tip) (Hillman et al., 2004; Burgess et al., 2008). This round trip

fluorescent yield is normalized based on the maximum possible yield.

2.2.4 Fluorescent beads

To validate the recording capability of the fiber bundles, the tips of loose fibers were immersed in a solution of water and fluorescent beads (Bangs Laboratories FSDG007, 7.32 μm diameter, 480 nm excitation, 520 nm emission). The ferrule and polished imaging surface were held below a traditional fluorescent microscope (Olympus, 20 \times objective) with a broadband white LED (Thorlabs SOLIS-3C) set at 60% brightness and a GFP filter cube (Semrock BrightLine GFP-4050B, 466/40 excitation, 525/50 emission, 495 dichroic). Excitation power from the objective was measured at 6.27 mW. As beads diffused in the water, changes in fluorescence were recorded by a sCMOS camera (Hamamatsu ORCA-Flash4.0 v2) with a resolution of 2048 \times 2048 16 bit pixels and an exposure of 50 ms per frame. Saved CXD files were processed in MATLAB using a custom pipeline. Frames were motion corrected using the Scale-Invariant Feature Transform (SIFT) algorithm (Vedaldi and Fulkerson, 2008; Lowe, 1999; Lowe, 2004). A standard deviation image created by calculating the standard deviation of pixels across frames was used to identify those fibers that were in the solution and where bead diffusion resulted in variability in the fluorescence. For the identified fibers, traces were generated by extracting and averaging all pixels that corresponded with the fiber. Traces were converted to $\Delta F/F_0$, where F_0 corresponds with the 5th percentile intensity (i.e., background intensity when there is minimal fluorescence from nearby beads).

To calculate the contrast-to-noise ratio (CNR) for the bead recording, we performed a second recording to measure noise. The fibers were placed in a solution of fluorescein and water, such that the fiber brightness matched the peak brightness observed during the fluorescent bead recording. The signal was recorded, and again, traces were generated by extracting and averaging all pixels that correspond with each

fiber. For the CNR, we calculate the contrast from the fluorescent bead recording by subtracting the 5th percentile from the 95th percentile intensity and averaging across fibers; we calculate the noise as the standard deviation for traces from the fluorescein recording.

2.3 Results

2.3.1 Histology

Bundles of between 50 and 5,000 microfibers were implanted into zebra finch basal ganglia (area X) at a depth of 2.9 mm. To understand the impact of the bundles, histologic samples were collected to measure the distribution of fibers in tissue and to evaluate the distance between fiber tips and the nearest NeuN-stained neurons.

With the fibers anchored to the intact skull, the tissue was fixed and cryosectioned perpendicularly to the implant penetration angle. Sections were imaged and annotated to record the spatial distribution of microfibers at different depths. During insertion, each fiber follows a path of least resistance, splaying through the brain tissue. In these perpendicular sliced sections, the distribution of fibers resembles a bivariate normal distribution throughout the target region. In Figure 2-2, 530 fibers can be seen distributed spanning over 1 mm of tissue, while only displacing a cross sectional area of $26,640 \mu\text{m}^2$; a 1 mm diameter GRIN lens to access the same region would have a cross sectional area of $785,398 \mu\text{m}^2$.

Implant conditions account for much of the variability in the spread of the fibers. Based on anecdotal observations, the configuration of the fibers prior to implant—specifically, the spatial arrangement of fibers in the acrylic anchor point (used both to hold the fibers during the implant and the to anchor the fibers to the skull), and the spread of the fibers below this acrylic anchor point—appears to affect the final distribution of the fibers. For example, if the fibers spread in the air before coming

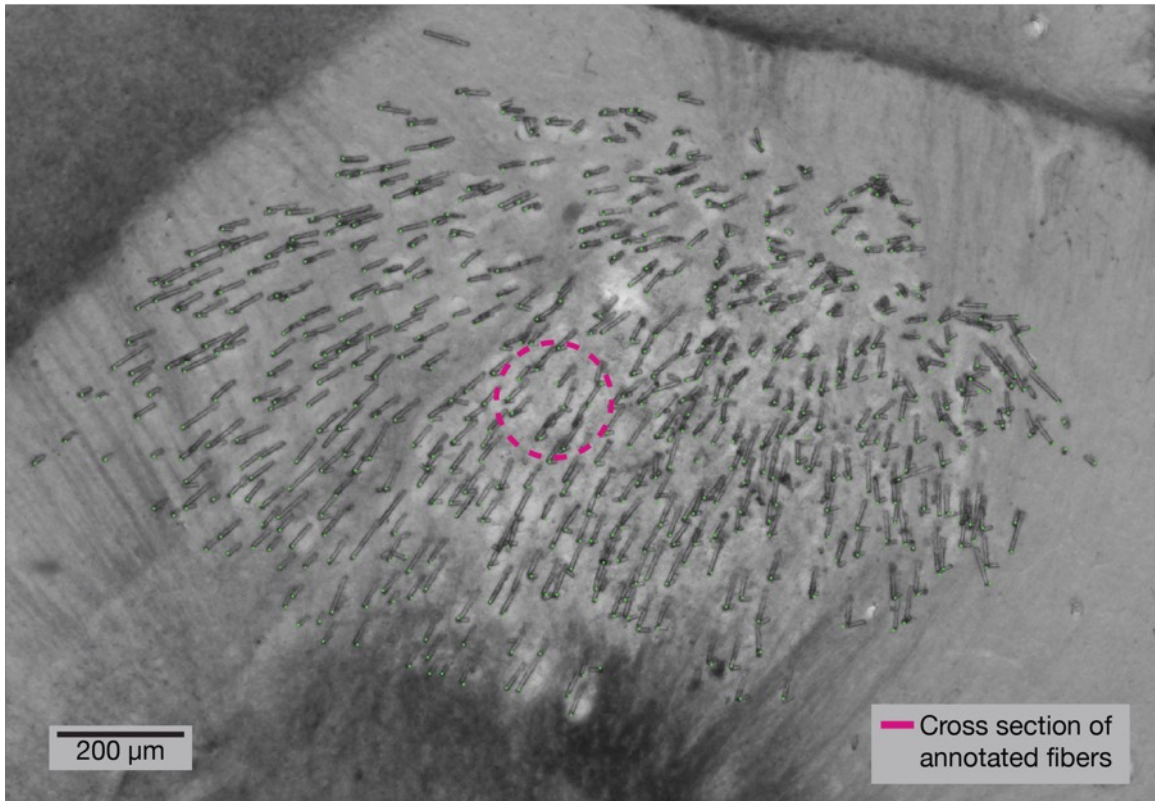


Figure 2:2: Histology at tip of implant shows microfibers splayed throughout the target region. A 100 μm thick brain section showing the tips of a bundle of 530 optical microfibers implanted at a depth of 2.95 mm. Before insertion, the bundle had a diameter of 570 μm. This section was collected four months after implant, and the brain sectioned perpendicularly to the insertion angle. The cross sectional area of tissue displaced by the microfibers (annotated in green) is 26,640 μm² (pink circle).

into contact with the tissue, we tended to observe greater spread after insertion into the tissue. The configuration of the fibers in the acrylic anchor point is difficult to control, as we sought to avoid directly squeezing or stressing the fibers. But we found that we could influence the amount of spread below the anchor point by keeping the fibers dry; if the fibers get wet, there is greater adhesion during insertion and, as a result, a more narrow distribution in the tissue. As a result, we avoided wetting the fibers and minimized moisture on the surface of the tissue prior to implant (as that would get wicked into the fiber bundle and increase adhesion).

In Figure 2-4, the distribution of the microfibers in the tissue can be seen to increase over the four slices from different depths in the same animal; the splay area is calculated by drawing a bounding ellipse containing 95% of the fibers. For each 1 mm of implant depth, the diameter of the splay area increases by $229.1 \pm 51.1 \mu\text{m}$ (std. dev., based on 9 pairs of slices from 5 animals); see Figure 2-3.

Tissue sections from animals with chronic implants (10+ weeks post implant) underwent NeuN staining to label neurons and DAPI staining to label nuclei. Since the red blood cells of birds contain DNA, DAPI labelled cells that are not NeuN stained include populations of glia, astrocytes, red blood cells, and any other non-NeuN stained cell nuclei. The slices show NeuN-stained neurons in close proximity to the fibers (see Figure 2-5). In instances where two or more fibers remain close during insertion, the proximity of the fibers may adversely affect the immediate tissue, as suggested by an increased presence of non-neural cells (DAPI stained but not NeuN stained) around such “clumps” of fibers.

By annotating both the fibers and the neurons, the presence of NeuN-stained neurons near the fibers can be compared to control slices (same region, no implant) to evaluate tissue impact. Figure 2-6 compares the distance from fibers to neurons in implant slices to the distance between randomly selected points and neurons in control

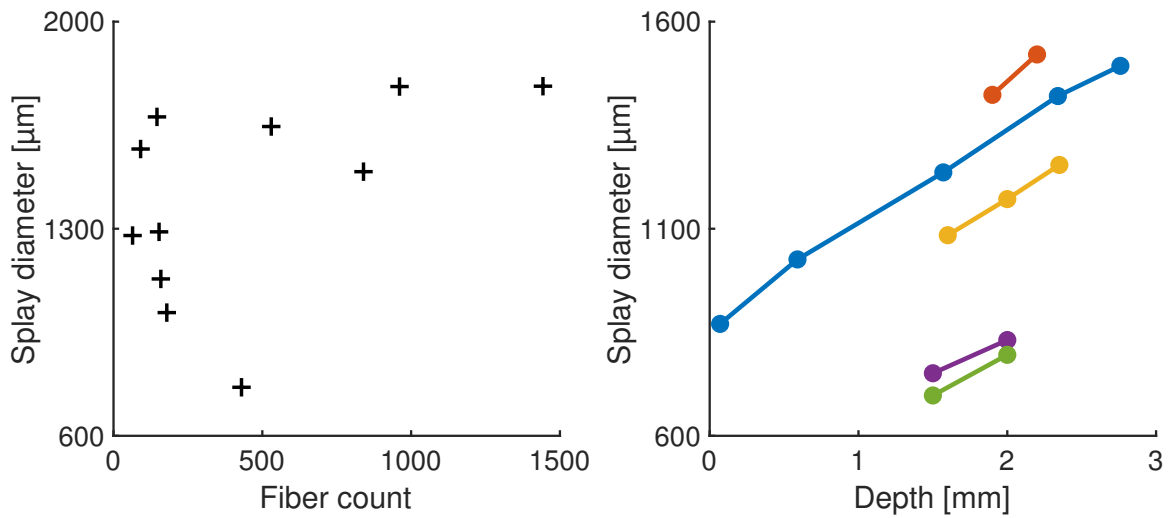


Figure 2-3: Diameter of splaying increases linearly with depth.

Left: Splay of fibers at a depth of 2.9 mm, in the target region of songbird basal ganglia from 11 animals. The plot shows the diameter of the ellipse describing the splay of the fibers for various implant sizes. As the number of fibers increases, the area accessed by the fibers increases. Right: For five animals, slices were collected at multiple depths to estimate splay diameter as a function of depth. For each 1 mm of implant depth, the diameter of the splay increases by $229.1 \pm 51.1 \mu\text{m}$ (std. dev.).

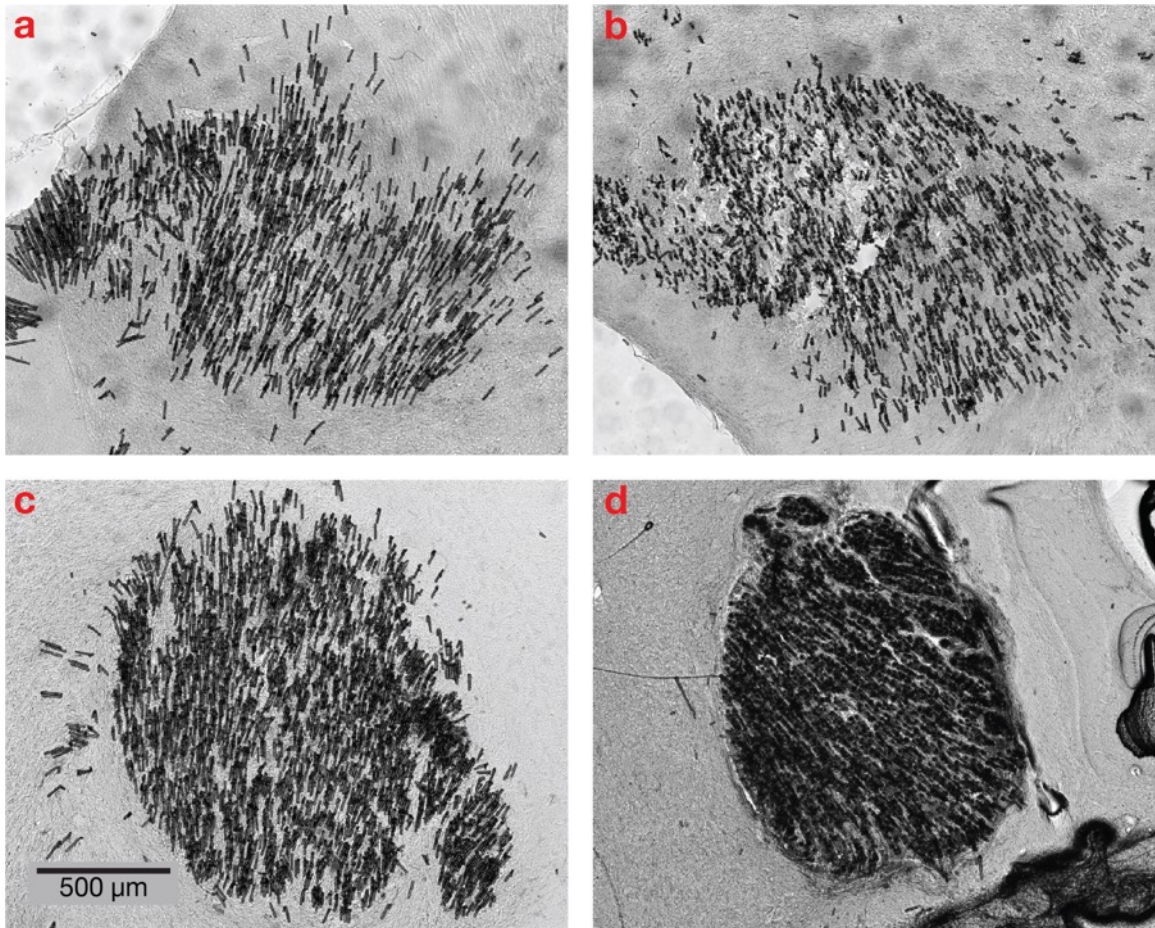


Figure 2-4: Histology at different depths as the fibers splay during insertion. A bundle of approximately 1,125 optical microfibers implanted at a depth of 2.95 mm. Eight weeks after the implant, the animal was perfused and the brain sectioned perpendicularly to the insertion angle. At the surface, the bundle diameter was 1.03 mm. These 70 μm thick slices from depths (a) 2.76 mm, (b) 2.34 mm, (c) 1.57 mm and (d) 0.59 mm reveal a gradual spreading of the optical fibers during insertion as each fiber follows a path of least resistance.

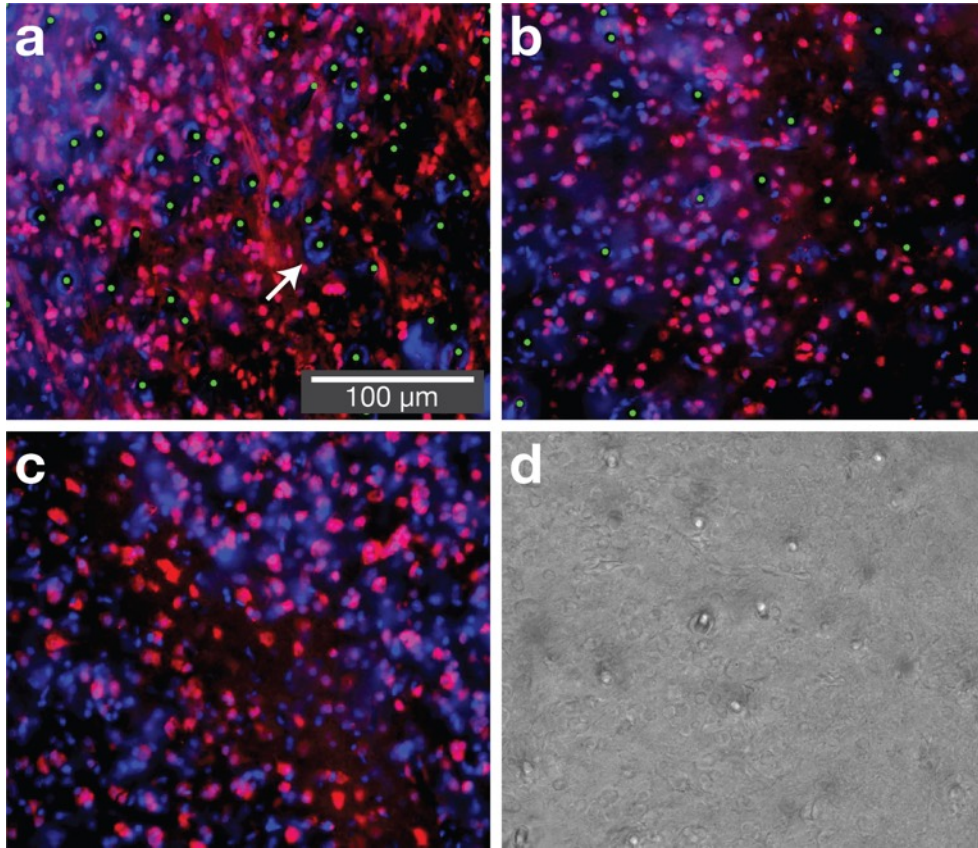


Figure 2-5: At chronic time points neurons are found in close proximity to fibers. Three sections from zebra finches implanted with optical microfibers, collected at least ten weeks post-implant. Sections are near the tip of the implant, within the basal ganglia (area X, depth 2.9 mm). (a) and (b) show implants in the basal ganglia (bundle sizes of 4,500 and 1,125 fibers respectively), (c) shows unimplanted basal ganglia, and (d) shows a corresponding brightfield image used to confirm fiber locations. Red is NeuN (neurons), blue is DAPI (nuclei) and green dots are manual annotations that reveal fiber locations. The immunohistochemistry shows NeuN-stained cells in close proximity to fibers. In some cases, we observe a dense circle of DAPI stained cells in close proximity to the fibers (arrow), suggesting either bleeding (in birds, red blood cells have DNA) or a reactive tissue response (such as glia or astrocytes). This most frequently occurs at locations where multiple fibers are in close proximity (this can occur with bundles of over 4,000 fibers or when fibers are wet prior to insertion). The length scale of reactive tissue response is approximately an order of magnitude smaller than for silicon electrode shanks with a 50 μm profile (Szarowski et al., 2003).

slices. The control measurement provides a lower bound for distance to the nearest neuron, if the implant had no impact on the tissue. For the implanted slices, the distance from a fiber to the nearest NeuN-stained neuron is on average $12.81 \pm 9.22 \mu\text{m}$ (std. dev.), while on the control slice, the distance from a randomly selected point to the nearest neuron is on average $8.32 \pm 4.72 \mu\text{m}$ (std. dev.).

We also can compare the NeuN-stained cell density surrounding each fiber relative to the cell density seen in the control slices. In the $50 \mu\text{m}$ region surrounding each fiber, we observe a NeuN density of $69.8\% \pm 17.9$ (std. dev.) the density seen in control slices (same region, no implant). Because the $50 \mu\text{m}$ surround typically includes other fibers, we subtract the cross sectional area of such neighboring fibers from the $50 \mu\text{m}$ area when calculating the density.

NeuN staining alone does not provide a comprehensive evaluation of tissue or neural health; variability in staining does not consistently indicate differences in neural populations and does not capture non-neuronal changes in tissue health (Ünal-Çevik et al., 2004; Collombet et al., 2006; Duan et al., 2015). Despite having a narrow immunohistochemical tool to evaluate tissue health, our histology data are consistent with the possibility that circuits remain healthy in the vicinity of the fiber tips.

2.3.2 Modeling

To quantify the potential neural population accessible via the optical microfibers, we modeled the optical profile of a single fiber and a bundle of fibers throughout a volume of tissue (see section 3.2) (Boas et al., 2002).

Figure 3.2 shows the normalized optical profile for a single fiber in tissue with spatially uniform anisotropy, scattering and absorption coefficients based on brain tissue measurements. At a distance of $40 \mu\text{m}$ from the tip of the fiber, the number of photon packets passing through an arbitrary point in the tissue drops below 10%. Although the fiber can weakly interface with a larger volume of tissue due to the

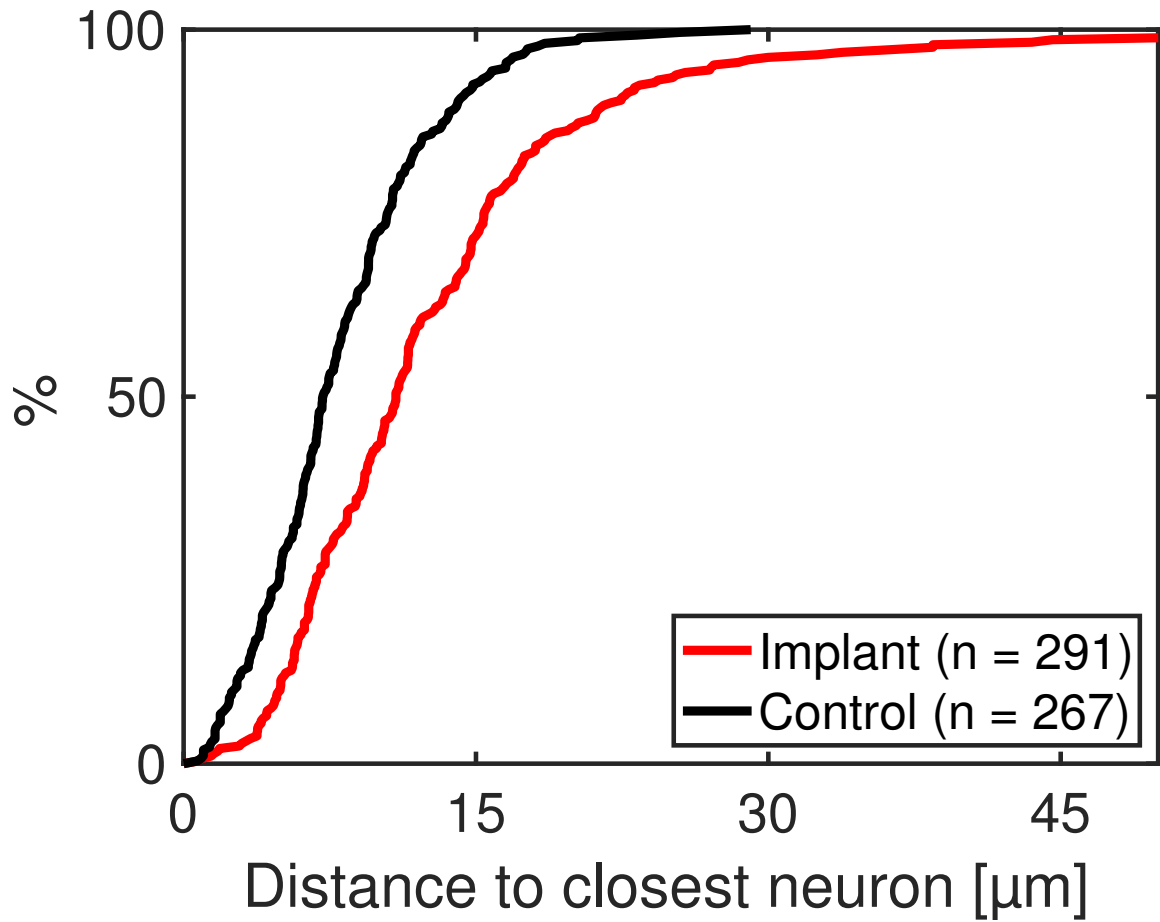


Figure 2-6: Histology reveals minimal tissue damage. The distribution of distances to the nearest NeuN-stained cell for implants (measuring from the edge of each fiber) and unimplanted controls (measuring from randomly selected points). The NeuN and DAPI staining shows that there are intact neurons in close proximity to the fibers; 85% of the fibers have a neuron within 20 μm .

scattering of light in the brain, individual fiber fluorescence will be dominated by neurons within 40 μm of the tip of the fiber. The viability of recording fluorescent signals depends on a number of additional properties that will vary based on the animal model and target region, including the indicator brightness, specificity of expression, density of the neural signal, and tissue autofluorescence.

Similarly, stimulation through the fiber will most strongly modulate neural activity within the region immediately surrounding the tip of the fibers. Based on the coupling 2.5 μW of 470 nm light into each fiber, and accounting for attenuation measurements of the optical path and fibers, and the simulated optical profile, one fiber will provide sufficient optical power to activate channelrhodopsins in a 18,000 μm^3 region surrounding the tip of the fiber given a 5 mW/mm^2 activation threshold (Yizhar et al., 2011). For the modeled neural subpopulation (medium spiny neurons in the zebra finch basal ganglia, with a density of 780,000 neurons per mm^3 (Kosubek-Langer et al., 2017)), this stimulation region equates to activating approximately 14 neurons. For comparison, this stimulation region equates to activating approximately 5 neurons in mouse hippocampus CA1, based on a density of 275,000 neurons per mm^3 (Ayberk Kurt et al., 2004; Richards et al., 2013).

Based on the histology of splaying fibers described above, it is possible to overlay profiles for hundreds or thousands of fibers throughout a brain region to quantify the properties of the bundle as an interface.

Figure 2.8 shows a distribution of normalized excitation/stimulation power reaching neurons for a simulated bundle of 500 fibers. Although the neurons receiving the most optical power are within the first 100 μm below the mean implant depth, the scattering properties of the tissue and the overlap in the excitation profile of fibers means that the excitation light will affect many more cells 400–600 μm below the implant depth.

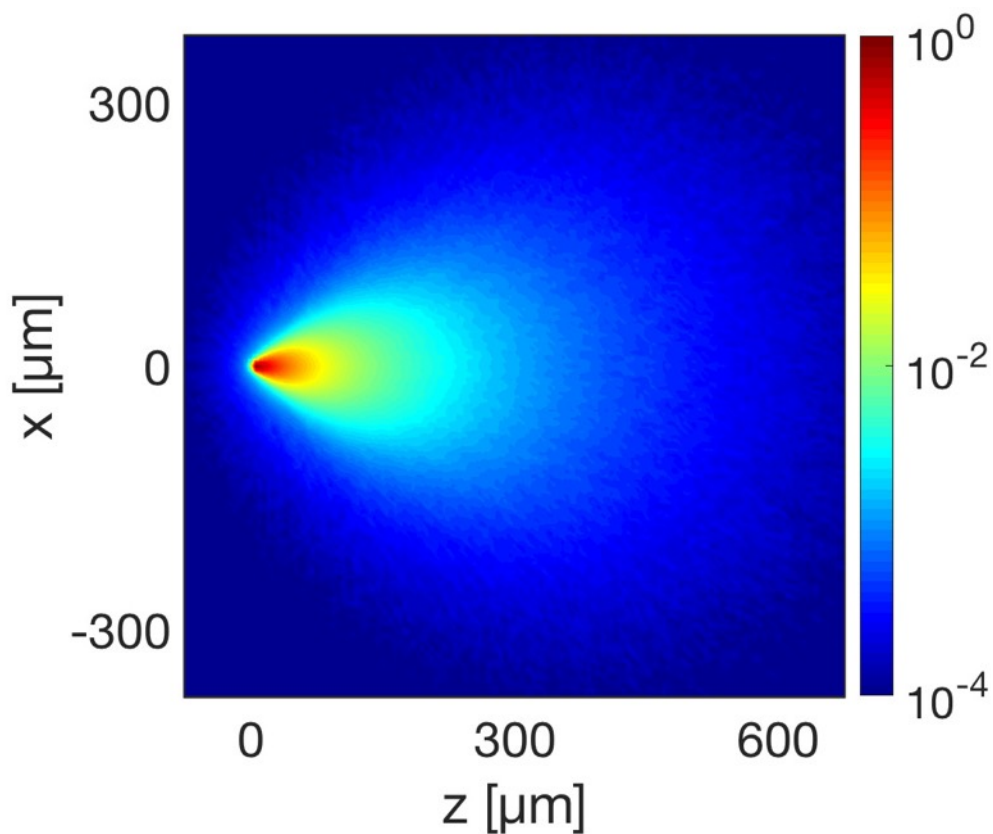


Figure 2-7: A single fiber would primarily interface with neurons in close proximity to the tip, based on the tissue scattering and absorption. The normalized log intensity emission profile of an optical microfiber with tip positioned at $[0, 0]$. The profile is a Monte Carlo simulation of photon packets propagating through brain tissue, with scattering and absorption properties estimated for 490 nm light. The simulated profile shows a strong interaction with tissue immediately below the tip of the fiber, enabling localized photometry or stimulation; the weak interactions with a larger volume of tissue will contribute background in recordings, or delocalized optogenetic excitation.

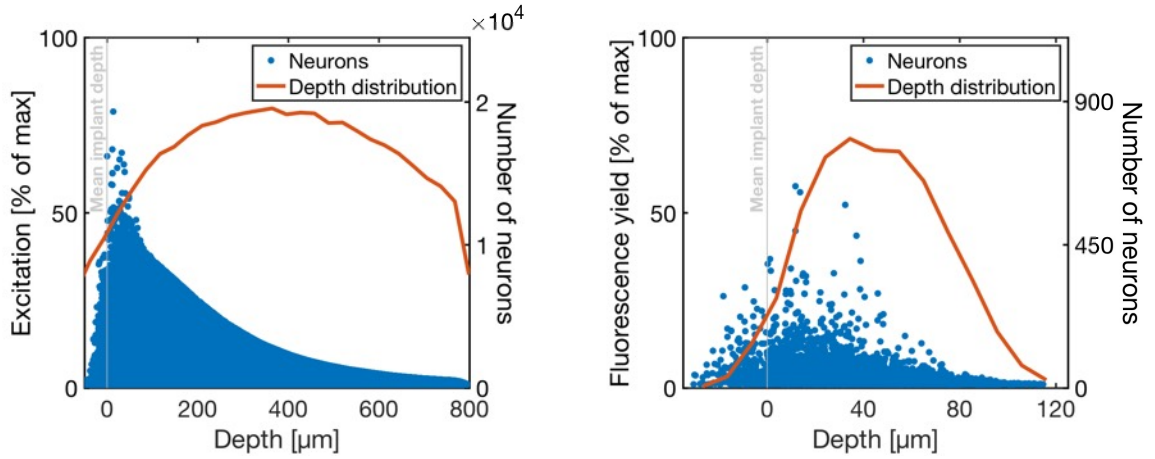


Figure 2-8: A computational model indicates that optical microfibers would record or stimulate neurons immediately below the fiber tips. Left: Distribution of light intensities reaching all modeled neurons, for uniform illumination of all fibers in the fiber bundle. These values are normalized by the maximum possible optical power (i.e., the power at the point in the tissue with the highest intensity). Blue dots are individual neurons, and the red line is a depth distribution of neurons that receive $>1\%$ of max excitation, indicating that for full bundle illumination, optical stimulation would activate cells far away from the fiber tips. Right: The round-trip fluorescence yield is calculated by first taking the total excitation power reaching the neuron (left) and scaling that by the strongest overlapping fiber profile (representing the collected fluorescence emission). These values are normalized by the maximum possible round-trip fluorescence yield (the maximum achievable given the excitation profile). Blue dots are individual neurons, and the red line is a depth distribution of neurons with $>1\%$ of max excitation.

In stimulation experiments, rather than illuminating all fibers, a subset of the fibers can be illuminated to produce more precisely targeted cellular modulation. Given the splay of the fibers, the vast majority of fibers can address a unique set of cells closest to the tip; yet the scattering properties of the tissue and the overlaps in the profiles mean that delivering stimulation through multiple fibers will increase activation in deeper regions and at the overlap between fiber profiles. For example, our model suggests that activating each fiber independently at non-overlapping times in a bundle of 500 fibers would serially stimulate approximately 4,600 cells; if all fibers were active simultaneously, there would be sufficient optical power to stimulate approximately 93,000 cells in the modeled neural population.

By activating small subsets of fibers, it is possible to avoid broad activation, while still exploring stimulation patterns with many degrees of freedom. By simulating overlaps in the optical profile for random sets of 10 fibers in a bundle, light delivered through the ten fibers will only activate an average of 11 more neurons (9.3%) than if the fibers were activated individually. Increasing the number of simultaneously active fibers will increase the crosstalk between the stimulation profiles. For example, sets of 50 fibers will activate an average of 506.4 more neurons (87.3%) than if the fibers were activated individually.

To evaluate the bundle as a potential recording interface, we calculate the round-trip fluorescence yield, indicative of how much fluorescent activity is collected by each fiber. Consistent with the profile for a single fiber, neurons within 40 μm of the mean implant depth have the highest fluorescence yield for recording purposes; cells up to 120 μm away will contribute to the signal, yet low fluorescence yield will likely relegate this contribution to indistinguishable background.

2.3.3 Fluorescent beads

As a preliminary test of the fluorescence recording capability, we immersed dissociated fibers in a suspension of fluorescent beads in water and recorded fluorescence traces as the beads diffused through the sensitivity profile of the individual fibers. Taking a standard deviation of pixel intensities over the recording, we generated a standard deviation image of the polished imaging surface, which revealed those fibers with large fluctuations in measured fluorescence resulting from the diffusing beads (Figure 2-9). Extracted traces (average intensity for pixels corresponding with the fiber), shown in Figure 2-9, reveal minimal crosstalk between neighboring fibers and a high signal-to-noise ratio. With excitation power of 6.27 mW measured at the imaging surface of the fiber bundle, we observed fluctuations in fluorescence intensity up to $23.7\times$ the F_0 intensity.

We calculate a CNR (contrast-to-noise ratio) with contrast $25.88\times$ the standard deviation of the noise observed during a similar recording with the fibers immersed in a uniform fluorescein solution (with fluorescent brightness matched to the peak signal in the bead recordings).

2.4 Discussion

Our histological results demonstrate that bundles of optical microfibers may provide an alternative to GRIN lenses to optically address 3D volumes in deep brain areas. The fibers self-splay during the implant process, achieving a distribution that resembles a bivariate normal distribution, with the diameter frequently exceeding 1 mm at an implant depth of 2.9 mm. There appears to be a relationship between the number of fibers and the diameter of the splay, but the trend does not achieve significance in the data set ($r^2 = 0.5$, $p = 0.11$). Small bundles show increased variability in splay that requires further exploration. We believe that implant conditions, such as

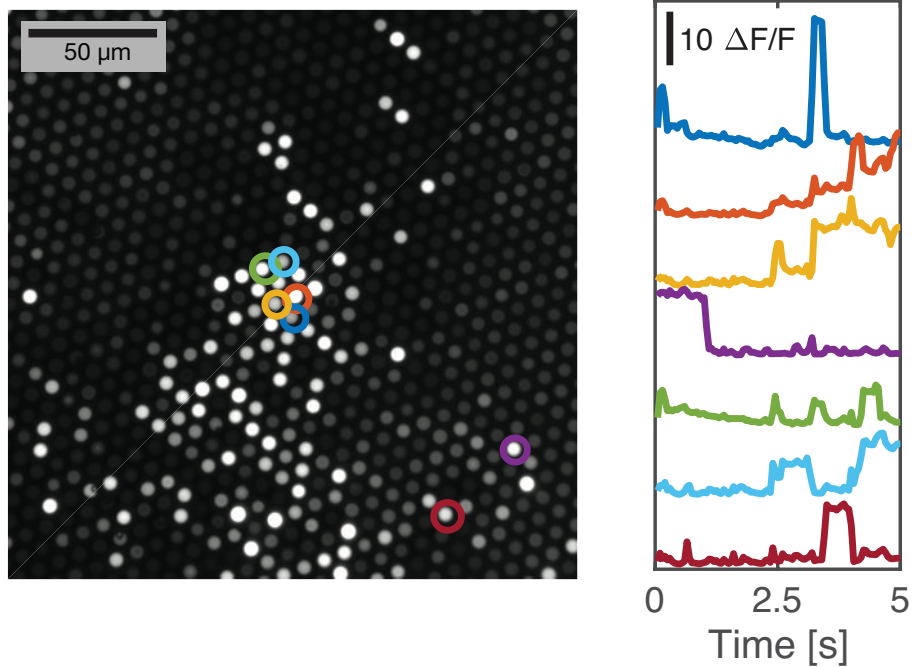


Figure 2-9: Recording of diffusing fluorescent beads reveals minimal cross-talk between neighboring fibers. The dissociated end of a bundle of fibers was immersed in a suspension of fluorescent beads in water, while the imaging surface was recorded via a traditional fluorescence microscope. The image on the left is a standard deviation image corresponding with a 1024×1024 portion of the full sCMOS sensor, where pixel brightness corresponds with variability over the 5 second recording. It accentuates those fibers immersed in water and with diffusing beads in close proximity to the fiber tips. Traces from a selection of fibers (circled) were extracted to show intensity over the recording. Fiber intensity varies as beads diffuse around the tips of the fibers, showing a high signal-to-noise ratio and minimal crosstalk between neighboring fibers.

the distribution of the fibers before entering the tissue, may account for much of this variability. In addition, as visible in Figure 2-4, the final distribution is not always symmetric, which could reflect tissue heterogeneity, non-perpendicular implant angles or non-perpendicular sectioning of the tissue.

At the fiber tips, we find NeuN-stained cell bodies in close proximity to the fiber, suggesting the small diameter, flexible microfibers may evoke a smaller foreign body response than that seen with larger glass or electrode implants (McConnell et al., 2009; Lee et al., 2016), but more extensive histological analysis is needed in a range of species. Because our current histology is unable to identify neurons in front of (below) the fiber apertures, we instead rely on the perpendicular sections to identify stained neurons adjacent to the fibers in the section closest to the tip of the implant, providing an estimate of the presence of neural signals within range of the fiber sensitivity profile. Future experiments may be able to reconstruct the full 3D path of the fibers through the tissue, and as a result, the presence of neurons within the fiber sensitivity profile.

We are limited in our ability to compare our data on NeuN-stained cells surrounding the implant with prior literature, due to the high number and distribution of the splaying microfibers. NeuN staining is often evaluated around a single implant point, and by measuring the labeled cell density in a 50 μm region surrounding the implant; in a bundle of our splaying optical fibers, that region often contains additional optical fibers. Even with this limitation, we observe NeuN-stained cell densities in the surrounding region that exceed those described for a range of larger, less flexible probes and implants (Biran et al., 2005; Winslow and Tresco, 2010; Welkenhuysen et al., 2011; Harris et al., 2011). These findings suggest the splaying microfibers may provide a less invasive option for interfacing with deep brain regions.

Our modeling results define the sensitivity profile of the fibers, indicating that

fibers optically interface with a small volume of tissue near the tip of the fiber. By superimposing the per fiber sensitivity profile in a geometry consistent with our histology, our model allows evaluating the fiber bundle in terms of light delivery (relevant for stimulation) and round-trip fluorescence (relevant to recording). Although in vivo experimental performance will vary due to tissue autofluorescence, and due to indicator brightness and density, our model provides intuition for the likely interface properties. When used for stimulation, our Monte Carlo simulation suggests that patterned illumination of a handful of fibers should precisely activate distinct subsets of the neural population in the target brain region with minimal crosstalk. When used for recording, the round-trip fluorescence will be dominated by neurons in the 40 μm region surrounding the fiber aperture; collectively, a bundle should act as a high channel count fluorescence photometry interface capable of sampling fluorescent indicator activity from hundreds or thousands of points throughout the target deep brain region.

This potential for recording via the fiber bundle is prototyped by the measurements of fluorescent microbeads diffusing in solution, suggesting that it is possible to excite and measure fluorescence through the 5 μm cores. The traces from neighboring fibers show uncorrelated activity, consistent with the splaying of the fibers and minimal crosstalk between fibers. Further work is needed to demonstrate the in vivo utility of the optical microfibers for optogenetic stimulation and fluorescence imaging.

Collectively, these findings indicate that bundles of splaying optical microfibers may provide an alternative to GRIN lenses for bidirectionally interfacing with deep brain regions. Specifically, this technique may achieve a unique compromise in the set of tradeoffs associated with extending optical techniques to less superficial brain regions. The method provides a high channel count interface distributed throughout a non-superficial 3D volume with potentially reduced tissue damage relative to GRIN

lenses. Additional histology in a wider range of species will be needed to compare tissue response between implanted fiber bundles and GRIN lenses.

For both recording and stimulating, the self-splaying property means that the fiber distribution will be incoherent—the position of the fibers is unknown once implanted. Because of this, the fibers are not able to elucidate absolute spatial patterns in neural activity. Despite not being able to identify the absolute position of the fibers in the tissue during usage, selectively illuminating individual fibers (e.g., by scanning a laser across the imaging surface with a galvanometer) and detecting the amount of light collected by all other fibers might serve as a proxy for measuring relative distances between fibers in the tissue (Heshmat et al., 2016).

When recording via the bundle, it is only possible to measure a single optical intensity value for each fiber, and each fiber will act as the optical equivalent of a local field potential. Yet, by examining correlations across fibers resulting from overlapping light fields, the recorded signals may be amenable to known source separation techniques such as independent component analysis (Hyvärinen and Oja, 2000) or bayesian source separation (Knuth, 2002), achieving an optical form of “spike sorting.”

For stimulation, a digital micromirror device (DMD) can be used to project patterned light onto the polished imaging surface at the end of the fiber bundle. Given attenuation measurements and sensitivity profile modeling, 2.5 μW optical power could be coupled into a fiber to stimulate neurons localized near the fiber aperture.

The simulations presented here are limited to normalized, noise-free measurements of the optical profile for individual fibers and assume uniform and consistent optical probe expression within a target neural population modeled as point sources. Such simulations enable estimating the the region with which the fibers interface, and the relative intensity of excitation/stimulation light delivery and the relative round-trip

fluorescence yield. By incorporating the expression and efficiency of the relevant fluorescent probe, the model is capable of calculating absolute power measurements and evaluating signal to noise performance.

The histology presented here suggests a new class of brain implants based on self-splaying microfibers, similar to previous work with nickel chromium aluminum microelectrode brushes used for chronic electrophysiology in primates (Krüger, 2010), but using 10–100 times more fibers per bundle, where each fiber is approximately 6 times less stiff (based on the area moment of inertia). A large number of ultrasmall fibers can be implanted in the brain while minimizing damage near the active end of the implant. This principle can apply to optical fibers as illustrated here, or to new electrode arrays, such as the carbon fiber ultramicroelectrode array (Guitchounts et al., 2013), or silicon carbide ultramicroelectrodes (Deku et al., 2017; Pancrazio et al., 2017). As high density interconnect solutions are developed for ultramicroelectrode arrays, we anticipate seeing the principle of self-splaying microfiber interfaces extended to the electrical domain (Wray, 2017).

Self-splaying optical microfibers compliment a number of new techniques aiming to achieve high channel count optical interfaces, such as multi-site fiber photometry (Guo et al., 2015) and optoelectronic probes with embedded waveguides or with on-device, implantable light sources and detectors (Warden et al., 2014; Wu et al., 2015; Segev et al., 2017). Technique development relevant to each of these methods will have broader repercussions, such as on-device μ LED illumination and CMOS sensors to achieve fully head-mounted and wireless optical interfaces; silicon waveguides and switches for lithographic manufacture of optical implants; and optical gratings to better localize and multiplex signals (Segev et al., 2015). The self-splaying form factor described here will benefit from these developments, with future iterations potentially moving illumination and sensing optics to a wireless, head-mounted device.

Chapter 3

Extracting individual neural activity recorded through splayed optical microfibers

3.1 Introduction

Rapid advances in genetic probes (Emiliani et al., 2015) and optical techniques for recording and manipulating neural activity (Deisseroth et al., 2006) are central to breakthroughs in systems neuroscience, providing tools for interrogation of precisely targeted population and circuit dynamics. Yet such techniques are inherently limited by the light scattering of tissue. To gain access to more deep brain regions, researchers remove superficial tissue (Dombeck et al., 2010) or employ implantable optics, such as GRIN lenses and prisms (Jung et al., 2004; Barretto et al., 2009; Andermann et al., 2013). Such implants can damage or obliterate more superficial tissue, and given dense local connectivity, may jeopardize local network dynamics in the tissue surrounding the implant (Hayn and Koch, 2015; Hayn et al., 2017; Goss-Varley et al., 2017).

A similar method, fiber photometry, permits access to deep brain regions for recording bulk fluorescence via an implanted fiber optic probe (Adelsberger et al., 2005; Cui et al., 2013; Adelsberger et al., 2014; Gunaydin et al., 2014). The technique enables high sensitivity recording of calcium or other fluorescent indicators expressed either in a target population or in long range axonal projections, but is often limited

to a single channel and requires an implant on a scale of hundreds of microns, similar to a GRIN lens. Subsequent variations have expanded the technique to record simultaneously from up to a dozen probes and/or from multiple regions (Guo et al., 2015). We are working to further extend the capabilities of fiber photometry, substantially increasing the number of simultaneous recording channels while decreasing the core diameter, and hence the cross section, of each fiber. By implanting bundles of hundreds or thousands of small diameter ($<8 \mu\text{m}$) optical microfibers, each fiber collects bulk fluorescence from a small region of tissue surrounding the aperture of the fiber, while displacing substantially less tissue (see chapter 2). During insertion, each fiber follows a path of least resistance, splaying through the target brain region. These bundles provide a minimally invasive way to sample fluorescence activity throughout a target, non-superficial region of the brain.

With the capacity to record many more channels and to record more precisely localized fluorescence, we move from a paradigm of interrogating bulk activity towards one of measuring circuit-level neural encoding. Like single photon imaging or multi-unit electrophysiological recordings, it is not possible to distinguish or limit recordings to a single neuron. But much as spike sorting enables separating individual neural activity, it is possible to incorporate knowledge of the target neural population and the sensitivity profile of the fibers to gain a more comprehensive understanding of the individual neural dynamics contributing to the recorded fluorescence signal.

When using a low density of fibers to interface with a low density cell population (a small number of neurons expressing the fluorescent indicator), the sensitivity profile of each fiber will be dominated by one or two neurons. Limited overlap between the sensitivity profiles of neighboring fibers will preclude source separation, as there will not be sufficient correlations between the fluorescence signals. Alternatively, when using a higher density of fibers, the sensitivity profiles will have greater overlap,

creating the opportunity to reverse the linear mixing of nearby neuronal signals. Under such conditions, the recorded signal is amenable to source separation techniques to extract individual neural traces.

In this chapter, we model bundles of hundreds or thousands of optical microfibers distributed throughout a target brain region as an optical interface for collecting fluorescence activity. Our model allows us to evaluate the interface properties of the bundle, and how variables like the distribution of fibers and neurons effects the interface performance. Our model results suggest that with a low density of fibers, each fiber will collect the optical equivalent of a local field potential, measuring bulk fluorescence from a small number of neurons in close proximity to the fiber tip; as the density of the fibers increases, overlaps between the fiber sensitivity profiles will enable collecting sufficient information to separate individual neural activity.

3.2 Methods

Interface simulation. We calculate the fluorescence sensitivity profile for a single fiber inserted into the tissue using Monte Carlo simulations of 10,000,000 photon packets launched from the fiber as described in (Boas et al., 2002). The tissue is modeled as a 1 mm^3 volume broken into isotropic $5 \text{ }\mu\text{m}$ voxels, with the tip of the fiber positioned in the center of the volume. Photon packets are emitted from the fiber with an angle determined by a Gaussian distribution reflecting the numerical aperture of the fiber (0.377). The packet is modeled moving through voxels and at each step can be either scattered or fractionally absorbed. Absorption is dominated by hemoglobin in the blood, and as a result we calculate the absorption coefficient based on a 3% blood volume fraction (BVF) (Bouchet et al., 2010) with a 15 g/DL hemoglobin concentration (Raabe et al., 2011) and a 70% oxygenation fraction. Given the extinction coefficient of hemoglobin (Kollias and Gratzer, 1999), our absorption

coefficients are $\mu_a = 0.337 \text{ mm}^{-1}$ for 490 nm light, $\mu_a = 0.343 \text{ mm}^{-1}$ for 512 nm light. Scattering is described well in the literature, and we use a scattering coefficient of $\mu_s = 20 \text{ mm}^{-1}$ with anisotropy $g = 0.9$ (Al-Juboori et al., 2013; Yi and Backman, 2012). By averaging the paths of all photon packets, we construct a three dimensional photon distribution throughout the tissue.

The sensitivity profile for a bundle of fibers is obtained by taking the linear superposition of the profile for a single fiber. Based on our prior histology documenting the distribution of bundles of hundreds to thousands fibers (section 2.3.1), we estimate the distribution of fibers in the tissue as a bivariate normal distribution in xy space. To explore the interface properties under various conditions, we vary the fiber density by changing the number of fibers for a fixed standard deviation of the spatial distribution of the fibers. The fiber depth distribution will vary based on how the fibers are cut prior to insertion; for our simulations, we model this variability as a normal distribution of depths with a standard deviation of $\sigma = 15 \text{ }\mu\text{m}$. The angle of each fiber is assumed to be uniform and parallel to the z-axis.

By superimposing the sensitivity profile on the tip of each fiber in the bundle based on the splay distribution (Hillman et al., 2004; Burgess et al., 2008), we can evaluate the interface properties of the full bundle. The bundle’s ability to deliver excitation light to a given neuron is equal to the sum of all superimposed sensitivity profiles; while the bundle’s ability to collect fluorescent emissions from a given neuron is measured in terms of the few fibers that receive the majority of the emitted light from that neuron. The combination of the excitation and emission forms a mixing matrix:

$$M_{i,j} = h_{i,j} \sum_{k=1}^n g_{j,k} \quad (3.1)$$

Where $h_{i,j}$ is the emission from neuron j collected by fiber i and $g_{j,k}$ is the excitation from fiber k that reaches neuron j . For the analysis presented here, we assume that excitation is static—that $g_{j,k}$ does not change over time.

Neural population simulation. Equipped with this model of the optical interface properties for a bundle of microfibers, we can now evaluate the ability to measure signals from a simulated neural population. We simulate a volume of tissue, of sufficient size to ensure that it includes all regions of non-negligible fluorescence sensitivity (usually around 1.2 mm^3), with a uniform distribution of neurons. We vary the density of neurons to understand the impact of signal density, but use densities that are consistent with relevant subpopulations of interest (Walton et al., 2012; Kosubek-Langer et al., 2017). Unless explicitly stated, simulations use a density of 250,000 neurons per mm^3 . We assume all neurons express the relevant genetic probe.

Neural activity is simulated as independent spike events (Bernoulli processes) (Kass et al., 2014). The spike probability at each time step is calculated based on the spiking frequency, which unless otherwise stated is 0.4 Hz. Spikes are then convolved with a GCaMP6 waveform; unless otherwise stated, simulations use the GCaMP6f waveform with a rise time ($t_{peak} = 0.14 \text{ s}$) and an exponential decay ($t_{\frac{1}{2}} = 0.32 \text{ s}$) (Chen et al., 2013). Fluorescence was modeled at 100 timesteps per second, and then downsampled based on the simulated frame rate for the recording setup.

The fluorescence traces for each neuron are then combined via the mixing matrix described in the previous section to produce fluorescence traces for each fiber. The fluorescence collected by a fiber can be written:

$$y_i = \sum_{j=1}^n M_{i,j} x_j \quad (3.2)$$

Where x_j is the fluorescence for neuron j and y_i is the fluorescence signal collected by fiber i .

Source separation. Given the linear mixing process inherent in the fluorescence signal collected by each fiber, the data are well suited to blind source separation techniques to estimate the underlying neural fluorescence signals. To improve the performance of the source separation, we developed an approach that incorporates our knowledge of the mixing process and associated fluorescent indicator dynamics. Similar to existing techniques that use deconvolution to estimate precise spike timing (Pnevmatikakis et al., 2016), we initially inverse filter the recorded signal to remove the fluorescent indicator dynamics. This step requires an estimate of the exponential decay associated with the calcium response and indicator time constant, and can be omitted for indicators where these dynamics are not known or are not stereotyped.

$$Y = MX \text{ where } \vec{x}_i = \vec{w} * \vec{s}_i \quad (3.3)$$

$$Z = MS \text{ where } \vec{z}_i = \vec{w}^{-1} * \vec{y}_i \quad (3.4)$$

Where Y is the recorded fiber output, M is the mixing matrix, and X is the fluorescence signal produced by convolving the underlying signal \vec{s}_i of neuron i with the indicator waveform \vec{w} . By applying an inverse filter (\vec{w}^{-1}), we produce matrix Z that is equal to applying the mixing directly to the underlying signals.

Next, we apply the nonnegative independent component analysis algorithm (Plumbley, 2003) to perform blind source separation under the constraints of nonnegativity.¹ The algorithm first whitens the data, and then applies a series of orthonormal rotations to reduce the error between Z and the reconstruction of Z from the rectified

¹The software is open source and accessible at <https://github.com/nathanntg/fiber-source-separation> (DOI: 10.5281/zenodo.1314756)

(nonnegative) components of S .

Having separated the independent signals, we can then apply the waveform filter (\vec{w}) to produce fluorescence traces that correspond with the identified independent components.

As there are many more neurons than fibers, separating all neural activity is an underdetermined problem. This technique is limited to extracting as many neural traces as there are fibers.

Evaluating source separation. The evaluation of the source separation must consider both that the output of the source separation is a small subset of the underlying neural signals, and the underdetermined nature of the blind source separation. To this end, we calculate the correlation coefficients of each separated signal (\hat{x}_i) with each true, simulated fluorescence trace (\vec{x}_i). The quality of the separation is then evaluated based on how many of the separated signals have a sufficiently high correlation with a true trace. In the results section, we evaluate threshold choices and how they impact the number of extracted “true” signals.

To understand the source separation in the context of an experimental question, we further evaluate the separated signals on a spike detection task. Using the approach of detecting threshold crossings as a proxy for neural spikes, we can compare threshold crossing events in the separated signal with those in the matched underlying neural trace. This forms a binary classification task that can be measured in terms of a receiver operating characteristic plot and the accompanying area under the curve (Han,). The area under the curve (AUC) represents how well threshold crossings on the separated signal can be used to approximate threshold crossings on the true neural fluorescence; an area under the curve of 0.5 indicates poor performance (unable to separate), while a value of 1 indicates perfect performance.

As a control, we compare correlations between the separated signals with a novel

set of randomly generated traces.

3.3 Results

Relevant experimental technique. The relevant experimental technique being modeled, including the optical interface, implant methods and motivating histology, is fully described in section 2.2. In brief, we use commercially available flexible endoscopes (Schott 1534180), which are manufactured by dissolving an acid soluble glass between the individual fibers in coherent imaging bundles. This produces an endoscope with thousands of dissociated fibers that come together in polished imaging surfaces at both ends (figure 3·1b); each fiber has a core (diameter: 5.1 μm), a cladding (thickness: 1 μm) and the remnants of the acid soluble glass (thickness: 0.4 μm). By cutting the bundle in half, the dissociated fibers are exposed (figure 3·1c).

After cutting away a fraction of the fibers in the bundle (based on the desired implant size), the remaining fibers are anchored together 4–5 mm from the tip using a bead of light-cured acrylic (Flow-It ALC, Pentron Clinical). The bead is secured to a digital manipulator in a stereotaxic rig. An anesthetized animal is mounted in the rig, and a craniotomy and durotomy are opened above the target brain region. The fibers can then be slowly lowered into the tissue; the fibers have enough rigidity to enter the tissue without bending. Histology from implants shows that each fiber follows a path of least resistance, spreading through the target brain region (figure 3·1d).

The other end of the fiber (a ferrule and polished imaging surface) can be mounted below an objective in either a traditional fluorescence microscope or a purpose built optical configuration to provide excitation light and collect emission light via a CMOS sensor (figure 3·1a).

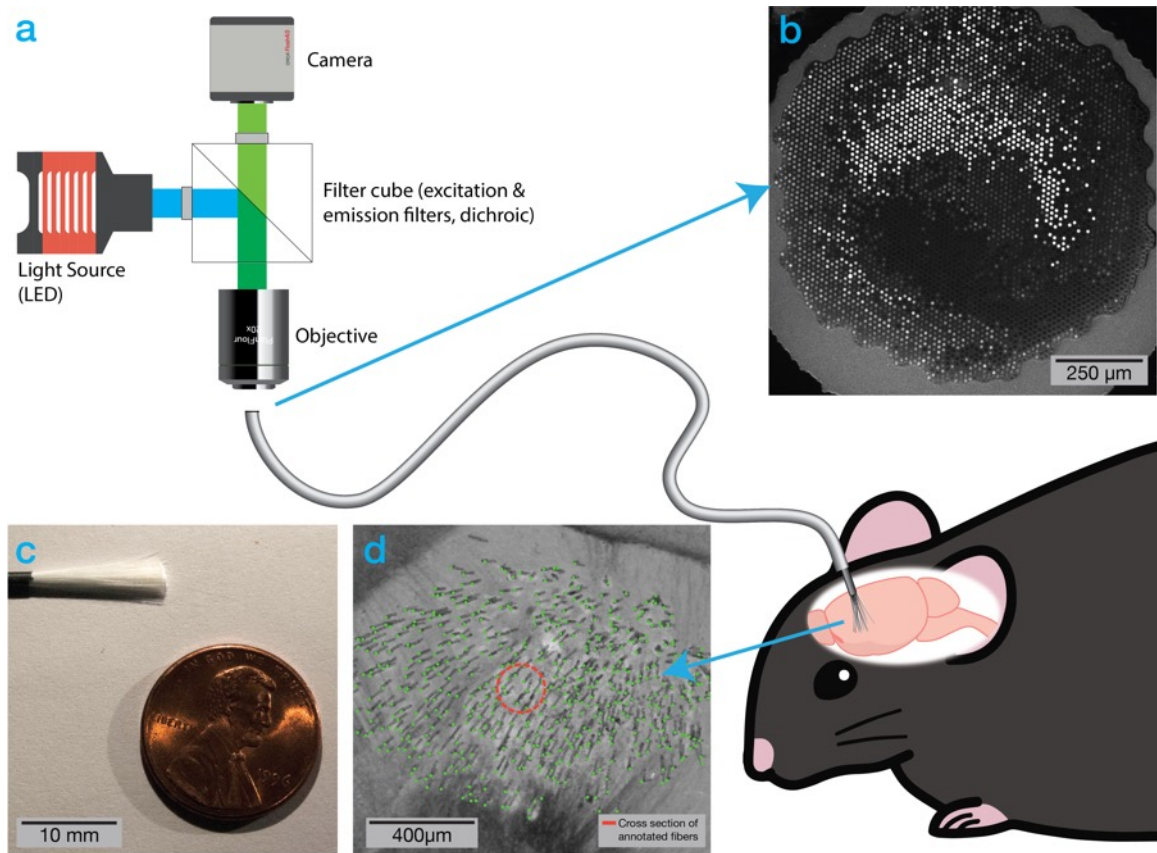


Figure 3-1: Illustration of the described method, using a bundle of optical microfibers as a multichannel, deep brain recording interface. (a) A standard fluorescent imaging configuration is used to interface with the fiber bundle. The polished imaging surface is mounted below an objective. Excitation light from an LED or other light source passes through a filter cube and is coupled into the fiber bundle; fluorescent emissions return through the objective, pass through the emission arm of the filter cube and are recorded by a camera. The fiber bundle consists of dissociated fibers, each with a diameter of $8\ \mu\text{m}$. The individual fibers are implanted into the target brain region and secured to the skull. (b) The polished imaging surface as seen by the camera. (c) A bundle of 18,000 fibers prior to implant with gray silicone sheathing cut away. (d) Histology at the tip of a bundle implanted to 2.95 mm in a zebra finch, showing 530 optical microfibers (annotated in green). The fibers displace substantially less tissue (orange circle is cross section of displaced tissue) than existing optical techniques for recording from such a large volume of tissue.

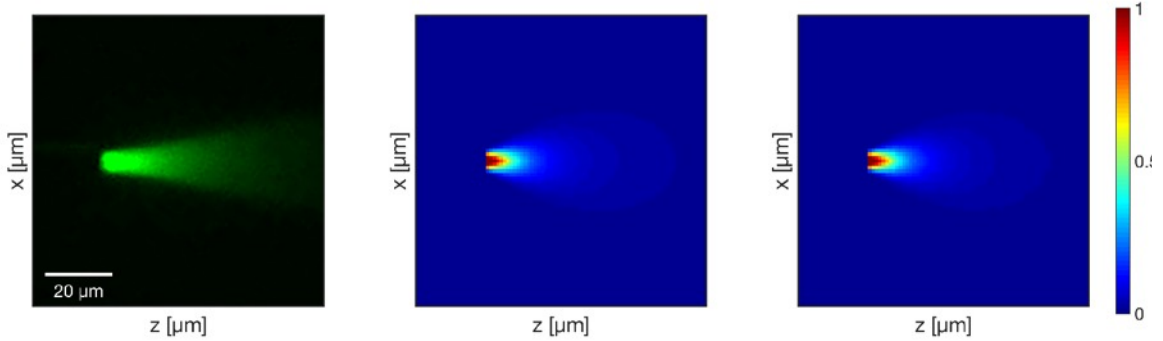


Figure 3·2: **Left:** A single fiber tip shown in a fluorescein solution with blue light (a 446–486 nm) emitted from the fiber. Due to the near total internal reflection, the light exits the tip of the fiber. The image, captured by a fluorescence microscope with a GFP filter, reveals the fluence excitation profile for the cut fiber. **Center:** The linear fluence excitation profile of a single fiber, calculated via a Monte Carlo simulation of photon packets propagating through water. **Right:** The linear fluence excitation profile from a single fiber, calculated via a Monte Carlo simulation of photon packets propagating through the tissue. At each step, a photon packet may scatter or be absorbed based on tissue properties estimated for 490 nm light. Note that incorporating tissue scattering properties does not dramatically alter the profile, as the scale is below the mean free path of light in the brain.

Fiber profile model. In figure 3·2, we show a 2D slice of this 3D photon distribution and compare it with a similarly generated profile of fluence in water (i.e., with negligible absorption and scattering (D&A Instrument Company (text), Linda Worlton (layout), 2008)). The profile in water and tissue are similar, reflecting the fact that the relevant length scales are below the mean free path of light in brain tissue. In addition, we compare the two computationally generated profiles with an image of a single fiber in a fluorescein solution. Blue light is shone through the fiber, and the illuminated fluorescein is imaged through a 500-550 nm emission filter, revealing a distribution consistent with the model.

Interface model. Calculating the fluorescence sensitivity profiles for various distributions of optical microfibers, consistent with prior histology, we are able to model

and evaluate the number and relative brightness of neurons contributing to the detected fluorescence signal. Figure 3-3 shows the modeled distribution of fibers and the relative brightness of individual neurons under different sets of conditions: two fiber densities (varying the number of fibers with the same standard deviation of splay) and two neural densities (reflecting different potential subpopulations). As the neural population is assumed to be uniformly distributed, increasing the density of neurons results in an increase in the number of neural traces being collected by the implant. Increasing the number of fibers has a more pronounced effect, as it increases the magnitude and uniformity of the excitation power delivered to the region and achieves a more dense sampling of fluorescence from the target neural population.

This relationship between the number of fibers and the number of neurons contributing fluorescence is explored further in figure 3-4, with each point based on the average of five randomly generated distributions of fibers. As the number of fibers increases, we initially observe a rapid increase in the number of neurons whose fluorescence contribution to a given fiber is above illustrative thresholds, due both to the increased sampling and to the increased excitation power. These effects eventually saturate as the distribution of fibers is kept fixed and all neurons within the field of view of the fixed distribution of fibers are contributing fluorescence signals.

These results demonstrate that the number of neurons contributing to the fluorescence signal increases more rapidly than the number of fibers. Under low densities of fibers, each fiber collects from a distinct set of neurons and the low excitation power means that the signal will be limited to the 2–3 neurons closest to the fiber aperture. But as the fiber density increases, the paradigm shifts to one where many neurons are contributing fluorescence to multiple nearby fibers (figure 3-4; right). As multiple neural traces are present in the signal from a single fiber, it becomes beneficial to be able to apply source separation techniques.

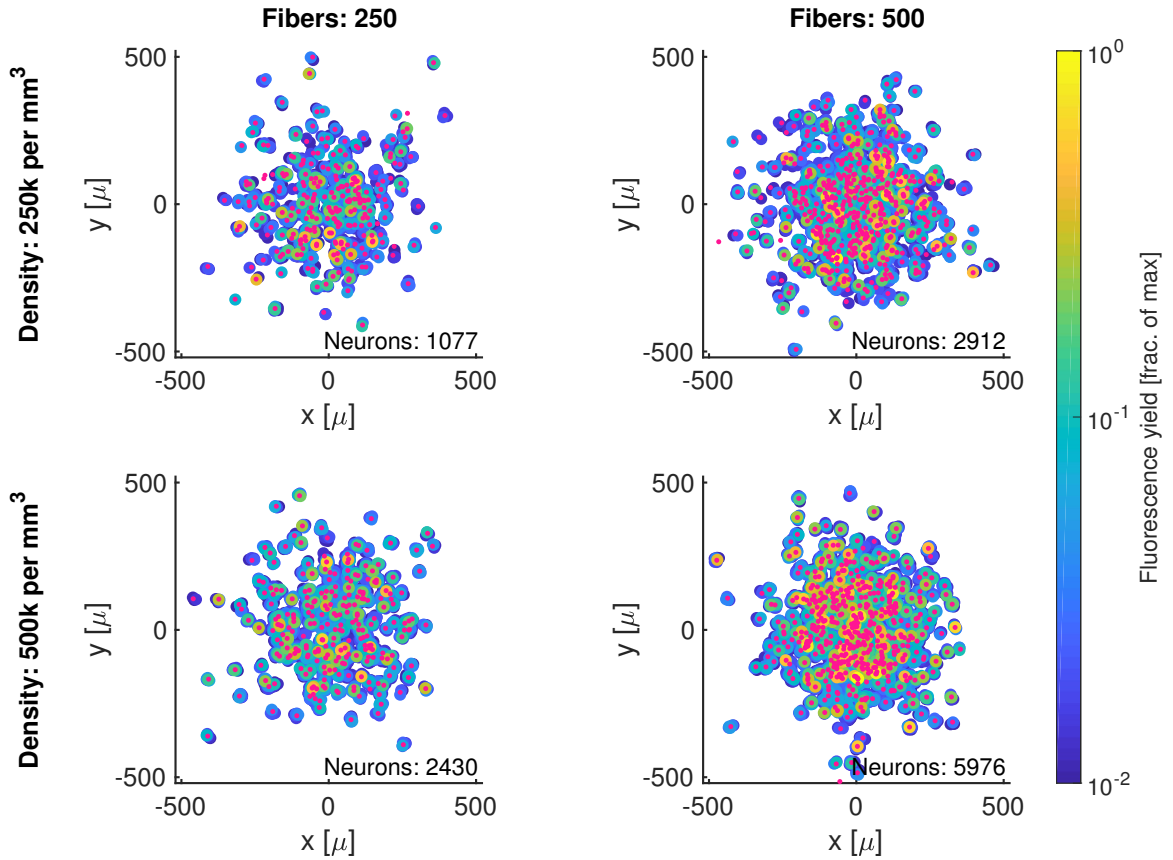


Figure 3.3: The neural population we expect to interface with through a bundle of splayed optical microfibers. The spatial distribution of fibers (small pink dots) is based on the bivariate normal distribution seen in histology slices (section 2.3.1), and is shown in relation to the neurons (large circles) that are contributing fluorescence to the collected signal above a 1% threshold. Neurons are colored based on their fluorescence signal contribution to the fiber normalized by the maximum fluorescence signal that would be recorded when a cell is immediately under a fiber. Columns show two distinct fiber counts (with same splay parameter, $\sigma = 150 \mu\text{m}$); rows show two distinct cell densities.

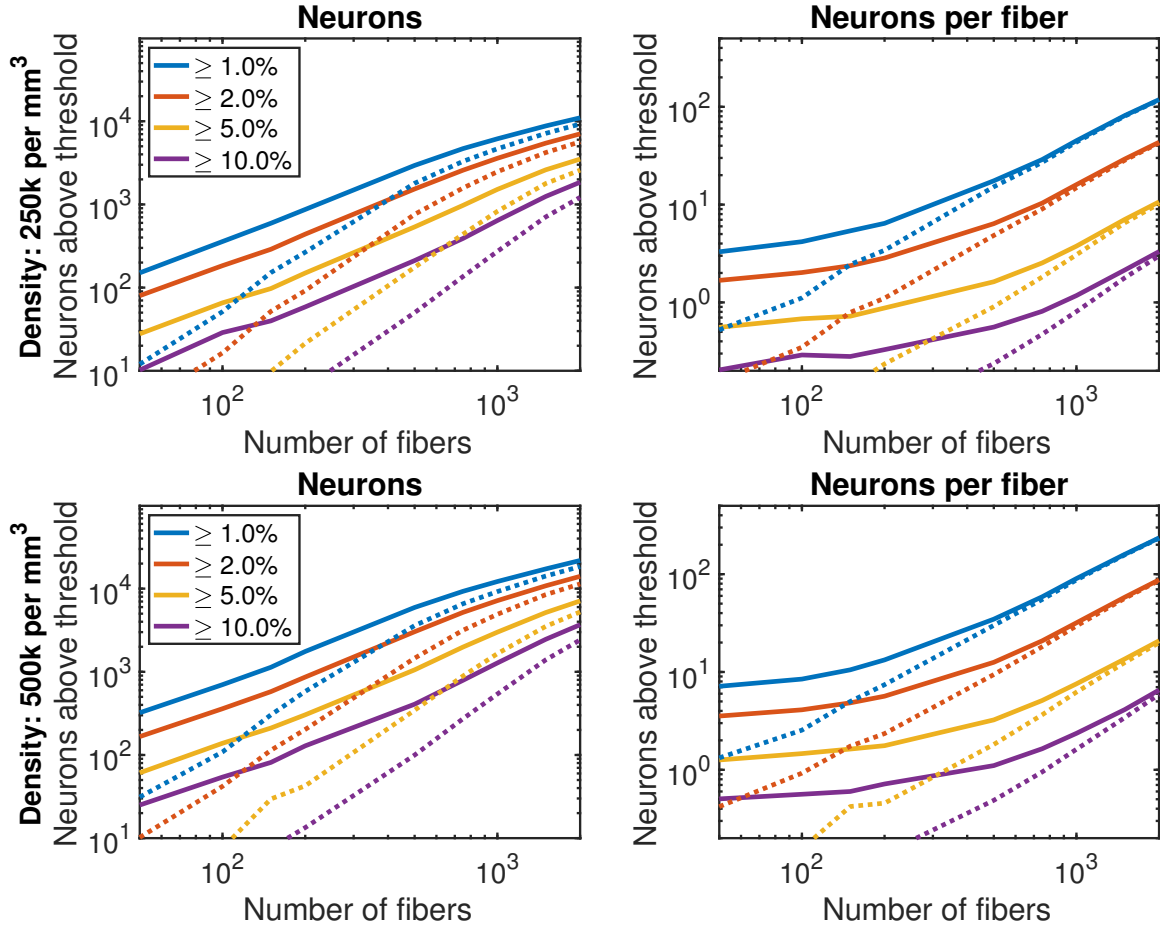


Figure 3-4: By increasing the number of fibers, while holding the splay diameter constant ($\sigma = 150 \mu\text{m}$), the bundle can interface with more neurons. The visibility of a neuron is calculated based on their fluorescent contribution to a fiber normalized by the maximum fluorescence signal that would be recorded when a cell is immediately under a fiber. Each point is the average of five randomly generated fiber implant distributions. **Left:** The solid lines plot how many neurons are clearly visible (given different thresholds, represented as different color lines) to at least one fiber in the bundle. The dotted lines plot how many neurons are clearly visible to two or more fibers. **Right:** How many neurons are visible to a single fiber in the bundle. As the number of fibers increases, the excitation power increases and more neurons become visible.

For source separation to be effective, there needs to be overlap in the sensitivity profiles of fibers and, as a result, neurons contributing fluorescence to multiple fibers. The dashed lines in figure 3-4 show how many neurons contribute fluorescence to two or more fibers. As the number of fibers increases, this value also increases, suggesting that source separation becomes more feasible.

The breakdown of the fluorescence signals recording by an average fiber is shown in figure 3-5, depicting the relative contribution of the neurons that most strongly interface with the fiber. Each fiber collects the fluorescence from many neurons. Figure 3-5 shows that the brightest cell is on average 50–100% brighter than the next brightest cell contributing fluorescence to a given fiber. As the density of fibers increases (and, as a result, increases the uniformity of the excitation power), the drop off in brightness from subsequent neurons in the sorted list of neurons becomes less pronounced. We can look at this same breakdown from the other perspective: how many fibers capture the fluorescence from one neuron, as shown in figure 3-6. With a low number of fibers, the overwhelming majority of fluorescence from a neuron reaches a single fiber. As the density of fibers increases though, this shifts such that multiple fibers capture the fluorescence from a single neuron, permitting the application of source separation approaches.

Source separation. Given a higher density of fibers, we can apply the blind source separation technique described in the methods section (section 3.2) to approximate individual neural components that may be contributing to the recorded fluorescence. Figure 3-7 shows a simplified model of the linear mixing of hypothetical neural traces (based on a Bernoulli spiking process convolved with the GCaMP6f waveform), and the subsequent results of the the source separation technique.

In order to assess the performance of the source separation, the separated signals must be compared to all underlying neural activity signals to see if the extracted sig-

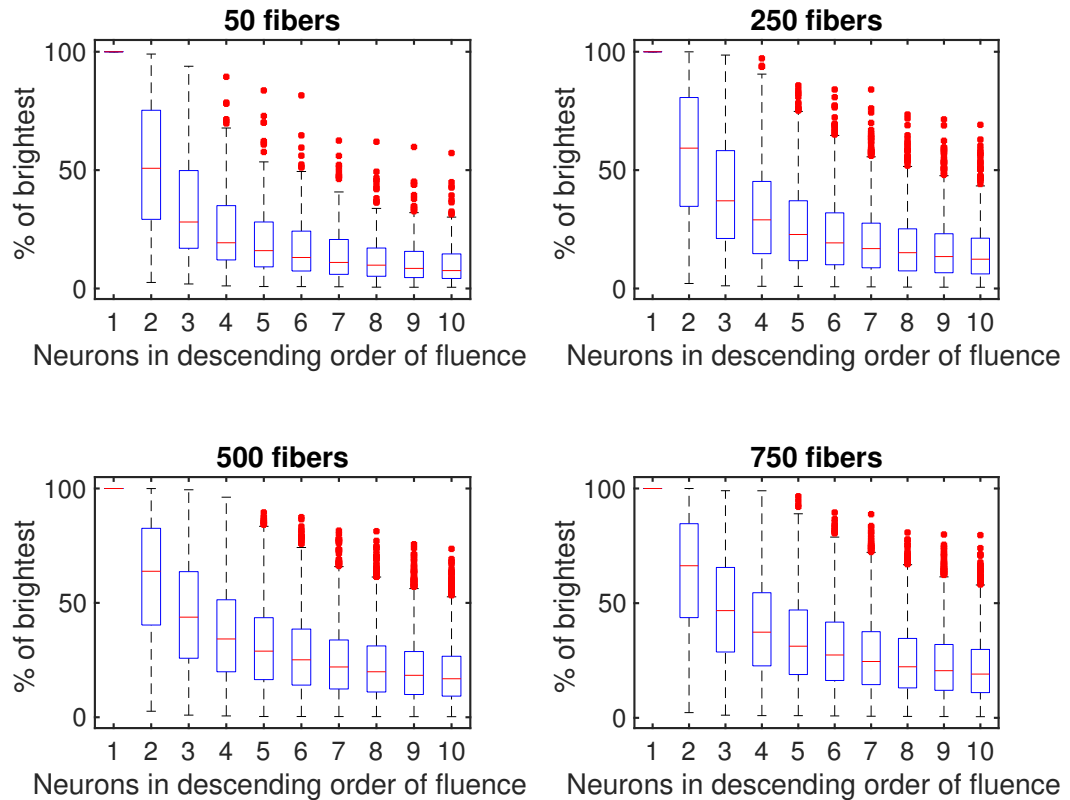


Figure 3.5: The contribution of individual neurons to the signal recorded through a single fiber. Values are normalized to the first (brightest) neuron visible to the fiber. Increasing the number of fibers does not substantially change the distribution, but delivers more light which increases the brightness of the neurons further from the tip of the fiber. Each fiber captures fluorescence from a number neurons, with an exponential drop off in the relative contribution of neurons. Each plot represents the average distribution of neural contributions for each fiber, averaged across fibers and across five randomly sampled distributions of fibers. The four subfigures show increasing numbers of fibers, with a constant amount of splay ($\sigma = 150 \mu\text{m}$).

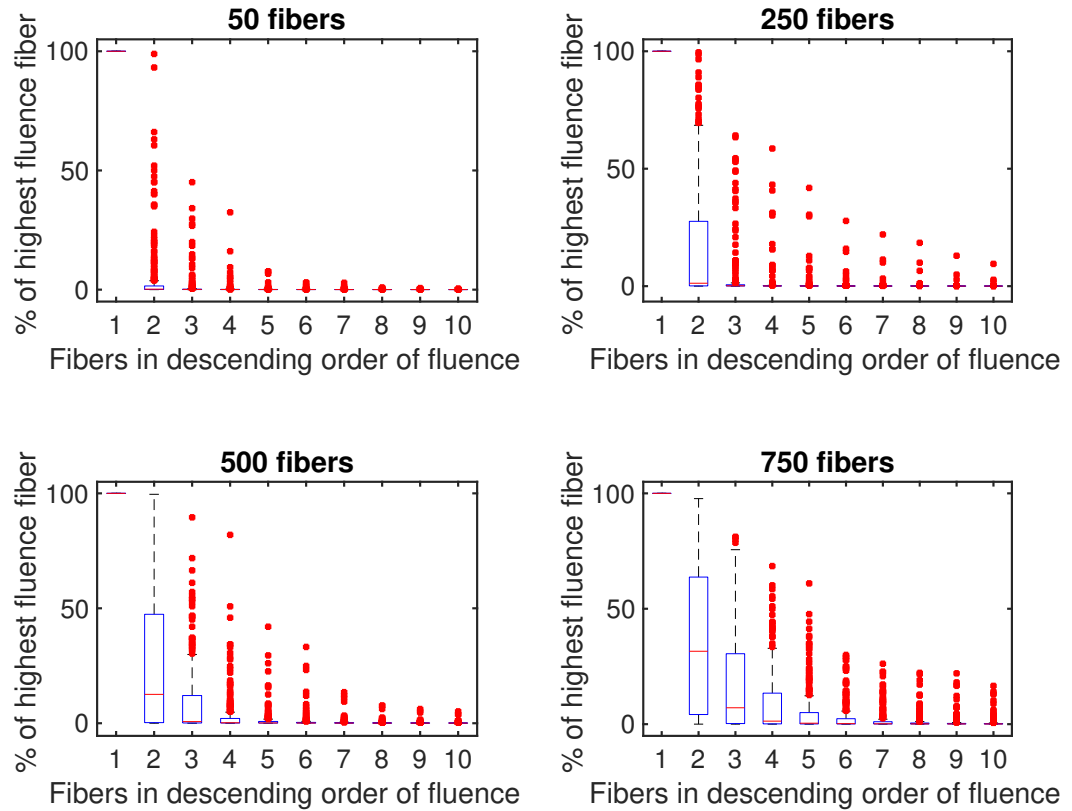


Figure 3-6: Each neuron primarily contributes fluorescence to a single fiber. Each box represents the strength of the interface between a given neuron and a fiber (round trip fluorescence), sorted in descending order of signal contributed to each fiber and normalized so that the strongest interface (the first fiber) is 100%. Plots are based on five sampled distributions of fibers, evaluating the 50 brightest neurons (most visible to a single fiber, in terms of round trip fluence). The four subfigures show increasing number of fibers in a bundle, with a constant amount of splay ($\sigma = 150 \mu\text{m}$).

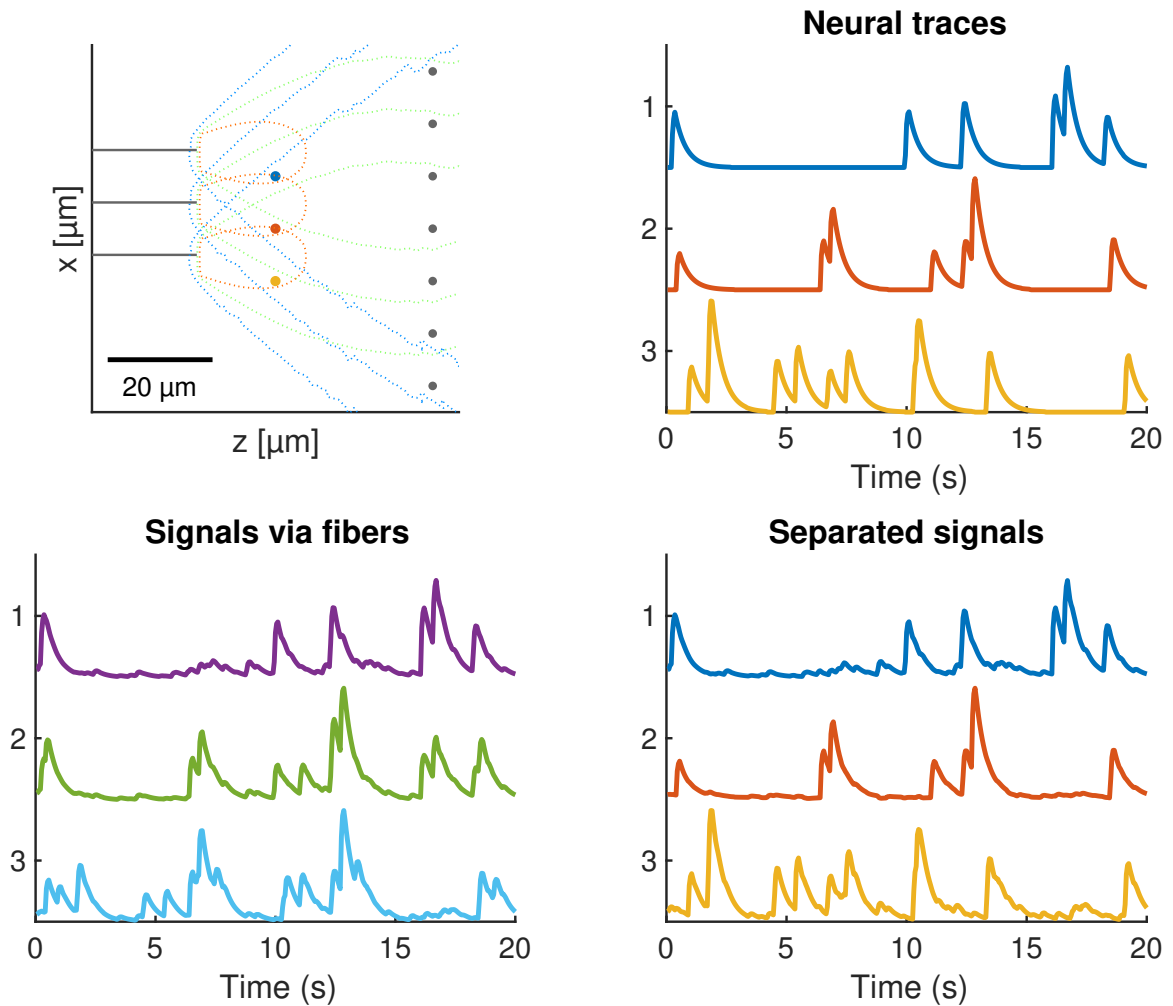


Figure 3-7: Simplified model used to exemplify the source separation process. **Top left:** A simple 2D configuration of fibers and neurons to demonstrate the source separation technique. Three fibers are shown in gray, each with contours representing their sensitivity profile. Three neurons (blue, red, yellow) are positioned near the fibers, while many neurons are distributed further from the fibers (creating background fluorescence). **Top right:** Traces for the three neurons of interest generated as a random Bernoulli process convolved with a GCaMP6f waveform. **Bottom left:** The signals recorded from the three fibers, representing a linear mixing of all the neurons based on the relative sensitivity. **Bottom right:** The three outputs of the source separation process, sorted to most closely match the original neural traces.

nals correspond with the activity of specific neurons. We match extracted signals with underlying neural traces based on correlations; extracted signals having a sufficiently high correlation ($r^2 \geq 0.6$) are considered an accurate match. Figure 3-8 compares the percentage of extracted traces that are accurate matches for three scenarios, under a number of different model parameters (fiber counts and neural firing rate). First, we show a control comparing with novel neural traces, confirming that identified accurate matches are not simply a probabilistic result of the large neural population being modeled; with novel data, none of the traces accurately match, indicating that matches are not false positives. Next, we assess accurate matches between the signals recorded via the fibers (without any source separation) and the underlying neural traces; as suggested by the earlier modeling, some fibers are dominated by 1 or 2 neurons, and produce accurate matches without additional processing. Finally, applying the nonnegative independent component analysis produces the highest percentage of accurate matches across parameters.

Because this sort of evaluation may be sensitive to the r^2 threshold, we also evaluated the utility of the matched traces for different thresholds. A receiver operating characteristic curve (figure 3-9) evaluates the performance of using accurately matched, separated signals to detect action potentials (via threshold crossing) for a range of r^2 thresholds. As the r^2 accuracy threshold increases, the matched separated signals provide a more useful input for threshold detection, at the expense of reducing the number of separated signals. These results motivated the selected threshold of 0.6. As a control, the same threshold crossing detection was repeated comparing the separated signals to unrelated, novel random traces. The area under the curve (AUC) was between 0.5–0.51 for all r^2 thresholds (not pictured), consistent with the lack of a relationship between the ground truth and separated signals.

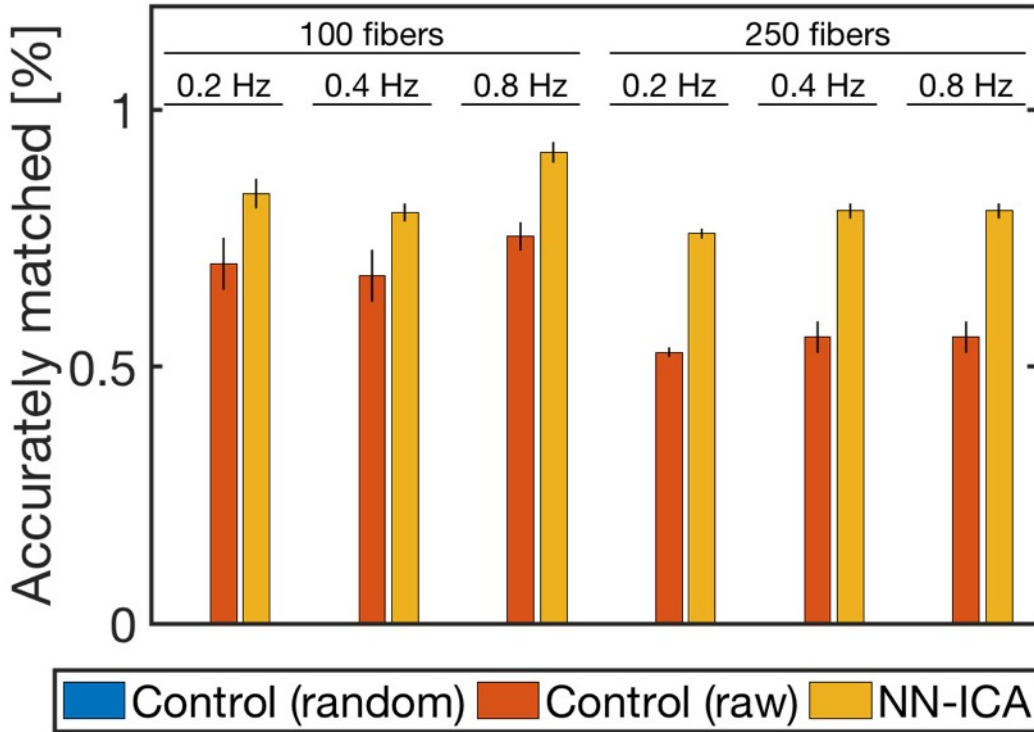


Figure 3-8: Percentage of extracted signals that accurately match an underlying neuron, based on a correlation of $r^2 \geq 0.6$. The first column (blue) is a control, showing no accurate matches when comparing fiber intensity with unrelated neural activity. The second column (red) shows the accuracy of the raw fiber intensity values; as some fibers are dominated by 1–2 neurons, there is a high percentage of traces that closely match underlying neurons. The third column (yellow) demonstrates the benefit of blind source separation, increase the number of accurately extract signals. These results are consistent and robust across various model parameters, including number of fibers and neural firing rates. Error bar shows std. dev. over 3 iterations.

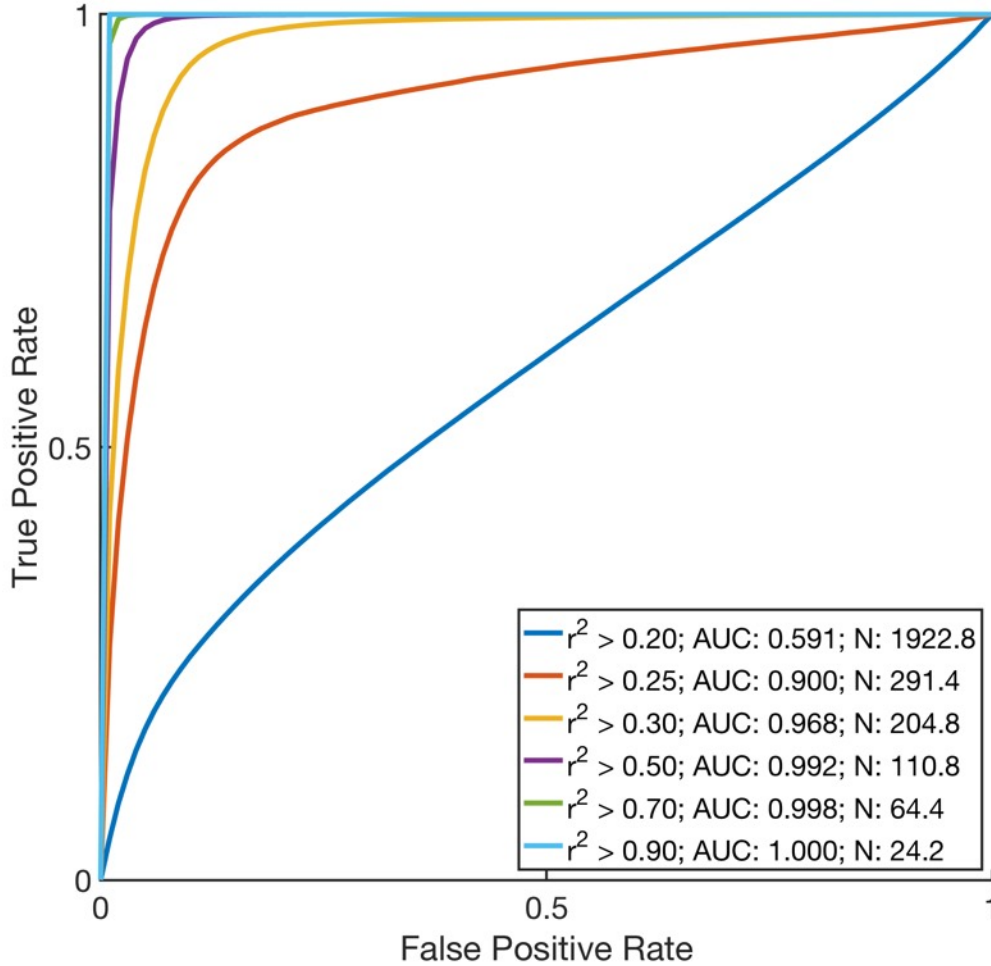


Figure 3-9: By increasing the r^2 threshold used to match separated signals with underlying neural activity, we observe an increase in accuracy in spike detection based on threshold crossing for spike detection, but a decrease in the number of matched neuronal signals. By altering the spike detection threshold, we can generate a receiver operating characteristic curve measuring the accuracy of the spike detection algorithm. Using different r^2 thresholds to match separated signals with the simulated neural fluorescence traces, we can generate different ROC curves. By lowering the r^2 threshold, we match more traces (N), but sacrifice accuracy (measured as area under the curve, or AUC). Average of five simulation based on 100 fibers with a splay of $\sigma = 125 \mu\text{m}$ in a region with a cell density of 250,000 neurons per mm^3 .

3.4 Discussion

Bundles of splaying optical microfibers present a versatile extension to existing fiber photometry methods, enabling the sampling of fluorescence from hundreds or thousands of points throughout a target brain region, while displacing less tissue than traditional, large diameter photometry ferrules or GRIN lenses.

When using a small number of fibers, the method achieves a high channel count variation of fiber photometry (Guo et al., 2015), collecting fluorescence activity from a small region of tissue at the tip of each fiber. As shown in figure 3-4, with a sparse target population or with sparse expression of the fluorescent indicator, this signal may correspond with just one or two cells.

As the number of implanted fibers increases, or as the density of the implanted fibers increases, the recording paradigm shifts. More fibers results in greater excitation power distributed over a larger volume of tissue (and, as a result, more fluorescent signal from more neurons), and higher fiber density results in increased overlap between the sensitivity profiles of neighboring fibers. With this shift, the fluorescent signal from a single cell is more likely to contribute to multiple fibers (figure 3-5). These correlations enable application of source separation techniques to estimate individual neural activity.

Blind source separation techniques are widely used in neuroscience for decoding of neural signals (Makeig et al., 1999), for identification of functional and anatomical connectivity (Randlett et al., 2015), and for analyzing electroencephalography (EEG) signals (Makeig et al., 1999), as well as for applications more akin to the one described here. Source separation—specifically, independent component analysis (ICA) (Hyvärinen and Oja, 2000)—has been applied in processing single- and multiphoton microscopy to identify and extract individual cellular contributions akin to spike sorting in electrophysiology (Mukamel et al., 2009; Xu et al., 2012; Patel et al.,

2015b).

These existing blind source separation techniques can be applied directly, as the overlapping sensitivity profiles associated with each fiber act as a linear mixing of fluorescence activity from the surrounding tissue. Yet the physical distribution of the splayed optical microfibers and the mechanics of the fluorescent indicator provide useful constraints that can further inform the source separation process. Specifically, we adopt an approach that incorporates the dynamics of the fluorescent indicators and the nonnegativity of the mixing process. First, we use an inverse filter to remove the fluorescence waveform. Our approach assumes consistent and known waveform dynamics, which enables the inverse filtering; should this assumption not apply, source separation techniques designed for convolutive mixtures become relevant and enable estimating both the mixing and convolution steps (Mitianoudis and Davies, 2003; Ozerov and Fevotte, 2010). We then use a nonnegative independent component analysis algorithm to estimate an unmixing matrix to separate the recorded signals into independent components. This achieves a linear unmixing that is consistent with the constraints of the recording mechanism, where the individual neural sources additively contribute to the recorded signals.

Similar techniques and model constraints are frequently used in traditional calcium imaging, using non-negative matrix factorization and deconvolution to extract neural activity and estimate underlying spiking (Pnevmatikakis et al., 2016). Another approach that may be applicable is Bayesian source separation, which seeks to estimate the mixing matrix and source signals by maximizing the probability of both the underlying source signals, and the resulting mixing of these source signals (Knuth, 2002). Our observations about the sparseness of the mixing process, as well as any existing knowledge regarding the target population activity, can be incorporated into the prior.

In exploring source separation techniques, we also looked at what factors impact the source separation performance. Unsurprisingly, increased recording duration improves the performance. More relevantly though, source separation performance is best with sparse signals (low spiking frequency and fast time course fluorescent indicators, such as GCaMP6f). Such sparse signals provide discrete, differentiable events that are conducive to estimating the underlying mixing process.

To evaluate the performance of the source separation for a realistic analysis task, we compared spike detection analysis on the separated signals and on the true, underlying neural traces. Separated signals are first matched with the underlying neural traces based on correlations; the majority of the separated signals have a strong correlation ($r^2 > 0.6$) with one of the true neural traces, and as a result, achieves a high level of accuracy in the threshold crossing task. Of course, analysis of real world data would not have the benefit of being able to identify the extracted signals that match the underlying neural activity, but these results suggest that the hundreds or thousands of channels of data collected through the fiber bundle have the potential to reveal neuron-level dynamics of interest.

Further work can look at incorporating additional information into the source separation process. For example, it may be possible to estimate the initial mixing matrix through empirical measurement of correlations between fibers. Specifically, by shining light down a single fiber and looking at light collected by the other fibers, it may be possible to estimate the relative spatial configuration of the fibers and, as a result, the correlations that we would expect in the linear mixing process.

More broadly, our work here has laid a modeling framework for evaluating high channel count fiber photometry as a means of interfacing with deep brain regions. By estimating the overlap of neighboring sensitivity profiles and hypothetical neural population dynamics, we can describe both the likely composition of the signals collected

by individual fibers and the larger mixing process that occurs. One limitation of our study, although likely minor, is that we simulated neural signals as arising from point sources. Further work is needed to explore the full impact of the fluorescent signals arising from large and complex neurons that may alter both the mixing process and the feasibility of source separation.

Chapter 4

In vivo recordings show calcium dynamics recorded via splaying optical microfibers

4.1 Introduction

Optical techniques for recording fluorescent probes are a cornerstone of rapidly advancing systems neuroscience. With an expanding suite of genetically encoded probes and techniques for targeting expression, it is possible to optically record calcium, voltage and neurotransmitter dynamics in a precisely selected neuronal subpopulation (Emiliani et al., 2015; Gong et al., 2015). Yet these techniques are inherently constrained by the scattering and absorption properties of tissue, constraining optical techniques to more superficial brain regions.

Three-photon imaging, which is at the cutting edge of optical techniques, can record from intact brain tissue at depths exceeding 1 mm (Horton et al., 2013; Wang et al., 2017). But to reach regions beyond this depth, current research relies on either removing superficial tissue (Dombeck et al., 2010) or implanting prisms or lenses (Jung et al., 2004; Barretto et al., 2009; Andermann et al., 2013; Cui et al., 2013). Such invasive implants can compromise or obliterate adjacent regions and potentially jeopardize local connectivity relevant to the neural population being investigated.

In an effort to extend optical techniques to deep brain regions that both preserves the ability to interface with hundreds of neurons—and, as a result, differentiate neural coding throughout the region—and that lessens the impact on local network dynamics

and neighboring brain regions, we proposed a new optical interface in section 2.2.1. Specifically, we constructed implants from bundles of hundreds or thousands of small diameter optical microfibers (as small as $6.8\mu\text{m}$). When implanted, each fiber moves independently and follows a path of least resistance, causing the fibers to splay as they are inserted. At a depth of 2.9 mm, a bundle of 1,000 fibers can spread over 1 mm in diameter. Because of the small diameter and flexible fibers, the fibers displace less tissue and elicit less tissue response, while still enabling interfacing with a large 3D volume of tissue.

Each fiber has a core and a cladding, achieving near total internal reflection, allowing the fiber to interface with a small region of tissue below the fiber aperture. Outside of the brain, the fibers come together in a polished imaging surface held in a metal ferrule, which can be fixed below the objective of a traditional fluorescent microscope.

In chapter 2, we have described histology evaluating the splay of the fiber bundles and the presence of NeuN-stained cells in close proximity to the fiber tips; in chapter 3, we have modeled the interface capabilities and properties of the bundles. In this chapter, we share initial in vivo recordings of fluorescence, including intravenous fluorescent agents, calcium-linked fluorescence during cortical spreading depolarization (CSD) and sensory evoked fluorescence resulting from forepaw stimulation. The intravenous fluorescent agent and CSD elicit bright, discernible increases in fluorescence. We find weak, but significant fluorescent activity associated with forepaw stimulation when using larger diameter fibers, and identify potential approaches to translate these successes to the small diameter fibers.

4.2 Methods

4.2.1 Fibers

The fiber implants are constructed from two commercially available sources, resulting in two variations with distinct fiber diameters. Bundles of 8 μm fibers are made from flexible medical endoscopes with 4,500 individual fibers each (Schott 1534180). The bundles are made as a coherent imaging bundle with an acid soluble glass between the individual fibers, in addition to the standard core and cladding; during manufacturing, the acid soluble glass is dissolved leaving the dissociated fibers, which increases bundle flexibility (Gerstner et al., 2004). Each fiber has a core diameter of 5.1 μm , and a numerical aperture of 0.377. The second variation, bundles of 37 μm fibers, are made as incoherent bundles with approximately 350 fibers individual fibers (Fiberoptics Technology Incorporated FTIIG24471). Each fiber has a core diameter of 34 μm and a numerical aperture of 0.6. In both cases, the ends of the fibers come together in polished imaging surfaces held in ferrules, and the dissociated fibers are covered in a flexible silicone or plastic sheathing for protection.

We cut the bundles in half with a razor, allowing access to the individual fibers. The protective sheathing is cut back, exposing a sufficient length of fibers for the implant. Depending on the desired implant size, a fraction of the bundle of fibers is cut away, again using a razor. The remaining fibers are secured in a cohesive bundle by placing a bead of light-cured acrylic (Flow-It ALC, Pentron Clinical) around the individual fibers, approximately 1.5 mm from the tips of the fibers. Once secured, the fibers can be further shaped to influence the final tissue geometry; we frequently cut fibers with a slight bevel (100 μm difference in length) to ensure that fibers sample fluorescence from a range of depths in the target region.

4.2.2 Surgery

Animal care and experimental procedures were reviewed and approved by the Institutional Animal Care and Use Committee (IACUC) of Boston University (protocols 17-017 and 17-026). Recordings were made in seven adult mice, including 1 wild type, 3 Thy1-GCaMP3 (Jackson stock 029860), 2 Thy1-GCaMP6f (Jackson stock 024339) and 1 Thy1-GCaMP6s (Jackson stock 024275). Mice were anesthetized with isoflurane during surgical procedures (3% induction, 1-1.5% maintenance). During surgery, the body temperature was monitored via a rectal probe and maintained at 37°C by a homeothermic blanket. The animal was placed in a stereotaxic frame for the surgery and implant procedure. A metal head post was secured to the temporal bone for immobilizing the head during recording. Contralateral to the head post, a craniotomy was created at either the barrel cortex or the forepaw region of the primary somatosensory cortex, sized to match the fiber bundle implant (1-1.5 mm). The dura within the craniotomy was removed.

The fiber bundle was held in a manipulator attached to the stereotaxic rig, with the fiber bundle positioned over the durotomy and the fibers orthogonal to the surface of the brain. The fibers were slowly lowered into the tissue at a rate of approximately 500 μm per minute. After the fibers were lowered to a depth corresponding with cortical layer V (500-600 μm), the bundle was secured to the skull surrounding the craniotomy with acrylic.

In three animals, the occipital bone was thinned, contralateral to the headpost and ipsilateral to the fibers, for laser speckle imaging.

In five animals, a frontal craniotomy was made, contralateral to the head post, to allow application of KCl in order to induce a cortical spreading depolarization (CSD). Until the CSD induction, the opening was covered with gel-foam soaked with artificial cerebrospinal fluid (ACSF).

4.2.3 Recording

During recording, mice were anesthetized with either isoflurane (1%) or α -chloralose (0.5-1%, IV, 0.1 mL per 30 min, Sigma-Aldrich C0128). During imaging, the body temperature was monitored via a rectal probe and maintained at 37°C by a homeothermic blanket.

Fiber recording. The ferrule and polished imaging surface were mounted below a traditional fluorescence microscope (Olympus) with either a 10 \times (PL L, 0.25 NA) or a 20 \times (Plan, 0.4 NA) objective, depending on the imaging surface size. The fibers were illuminated by a broadband white LED (Thorlabs SOLIS-3C) at 100% brightness, with a GFP filter cube in the imaging path (Semrock BrightLine GFP-4050B, 466/40 excitation, 525/50 emission, 495 dichroic). Excitation power at the objective was 9 mW. Emissions were recorded by a sCMOS camera (Hamamatsu ORCA-Flash4.0 v2) with 2 \times 2 binning, resulting in a final frame of 1024 \times 1024 16 bit pixels. Exposure varied across experiments, but was between 50–100 ms per frame. Frames were acquired using HCImage (Hamamatsu) and saved as CXD files.

Intravenous fluorescein isothiocyanate (FITC). To assess fiber sensitivity to fluorescent agents in the vasculature, the fibers were implanted in the mice (N = 2) and recorded while injecting fluorescein isothiocyanate (FITC)-labeled dextran (molecular weight 10 kDa or 2 MDa, Sigma-Aldrich FD10S and FD2000S) intravenously (50–100 μ L of 5% wt/vol in phosphate-buffered saline), either via the tail or retro-orbitally (Yardeni et al., 2011).

Inducing cortical spreading depolarization (CSD). To measure calcium fluorescence during a cortical spreading depolarization, a pellet of KCl was placed on the surface of the brain of the GCaMP transgenic mice (N = 5) at the frontal cran-

iotomy. A drop of ACSF was placed on the pellet to dissolve the pellet. This approach is known to produce repeated CSDs in anesthetized mice (Karatas et al., 2013). The pellet was prepared as described in (Karatas et al., 2013), by placing 30 mg of KCl in an Eppendorf, adding 10 μ L of distilled water and allowing the water to evaporate.

Laser speckle imaging. In order to verify the cortical spreading depolarization, blood flow was monitored via laser speckle flowmetry. The technique is performed as described in (Dunn et al., 2001; Karatas et al., 2013). A 785 nm laser diode (Thorlabs L785-P090 controlled by Thorlabs LDC210C) was used to illuminate the skull in a diffuse manner. The region was imaged via a 10 \times objective (M Plan Apo, 0.28 NA) and recorded using a CMOS camera (Basler acA2040-90umNIR). A set of 15 raw speckle images was acquired at a rate of 90 Hz, with 5 ms exposure time and averaged for further processing. New sets were acquired at 1-second intervals, and were converted to spatial speckle contrast (K) using a sliding grid of 7 \times 7 pixels (Tom et al., 2008). Speckle contrast images were converted to correlation time values (using the formula $1/K^2$), which are inversely and linearly proportional to mean blood velocity. Relative blood flow changes in an ROI ($\sim 0.2 \times 0.2$ mm) were calculated by dividing correlation time values at each time point by the baseline value (calculated by averaging 60 images acquired over 1 min before initiation of CSD).

Laser speckle frame acquisition was synchronized with the fiber recording by acquiring frame synchronization pulses from both cameras over the duration of the recording.

Evoking sensory activity. To measure calcium fluorescence evoked by sensory activity, two wire electrodes were inserted into the forepaw contralateral to the fiber implant in the transgenic mice ($N = 1$). The electrodes were connected to a stimulator (Grass Astro-Med S48) via a constant current isolation unit (Grass Astro-Med

PSIU6), configured to output 20 ms, 0.6–1.2 mA square pulses every 2 seconds. The stimulation was visually confirmed through observing associated muscle contractions.

Stimulation pulses were synchronized with the fiber recording by acquiring two signals channels, one corresponding with the fiber CMOS frame acquisition and one corresponding with the stimulation pulses, over the duration of the recording.

4.2.4 Analysis

Fiber recordings were converted from CXD files to raw binary image sequences using a custom Python script. Frames were then processed via a custom pipeline implemented in MATLAB (Mathworks). During the first pass, frames were motion corrected using an implementation of the Scale-Invariant Feature Transform (SIFT) algorithm (Vedaldi and Fulkerson, 2008; Lowe, 1999; Lowe, 2004) and then calculating the 1st and 99th percentile pixel intensities across all video frames. By calculating a pixel range image (by subtracting the 1st percentile intensity from the 99th percentile intensity for each pixel), fibers with dynamic fluorescent activity are clearly visible. MATLAB’s circle finding algorithm (Atherton and Kerbyson, 1999) is used to automatically draw regions of interest (ROIs) around fibers with high variability. To minimize artifacts from motion correction, ROIs are shrunk to 75% of their original size. The analysis pipeline then makes a second pass through the video, applying the same motion correction transform and averaging the pixel intensity for all pixels in each fiber region of interest. The end result is an intensity time course for each fiber of interest. Traces are converted to $\Delta F/F_0$, where F_0 corresponds with the median intensity in the period prior to the fluorescence onset.

To test the statistical significance of the sensory evoked behavior, a Student’s t-test was performed comparing the background subtracted fluorescence in the 100 ms after the stimulation to the background subtracted fluorescence in the 100 ms before the stimulation for those fibers where visual inspection identified a potential time

locked change in fluorescence ($N = 2$).

4.3 Results

In order to demonstrate and evaluate the recording capability of the bundles of optical microfibers, we performed a series of recordings across a range of externally evoked fluorescent events.

Intravenous fluorescein (FITC). Sensitivity to fluorescent agents in the vasculature was measured by injecting high molecular weight fluorescein conjugated dextran, while recording fluorescence via the implanted fibers. Figure 4.1 shows fluorescent traces for a retro-orbital injection of 2 MDa FITC. The fluorescent bolus is visible 1–2 seconds after injection, and has more sustained fluorescence than the higher molecular weight FITC (not shown). The fluorescent bolus corresponded with an average increase in fluorescent intensity of $0.22\times$ the F_0 intensity (std. dev. 0.011) in the 25 brightest fibers.

Induced cortical spreading depolarization (CSD). In transgenic animals expressing a calcium sensitive fluorescent probe, the ability to record calcium fluorescence was measured during a cortical spreading depolarization by dissolving a pellet of KCl on the surface of the brain, which is known to evoke multiple CSDs in anesthetized mice (Karatas et al., 2013). We recorded for 20 minutes, beginning at the time of application of the KCl. In four of the five animals, we observed one or more fluorescent events that corresponded with a CSD. Fluorescence, shown in figure 4.2, increased over $24.1\text{ s} \pm 16.8$ (std. dev), and recovered more slowly, over $87.7\text{ s} \pm 17.0$ (std. dev). This timing is consistent with previous measures of intracellular calcium in layer V cells during CSD (Gniel and Martin, 2010), but with a slower rise time consistent with the fact that a fiber will collect fluorescence from multiple neurons in

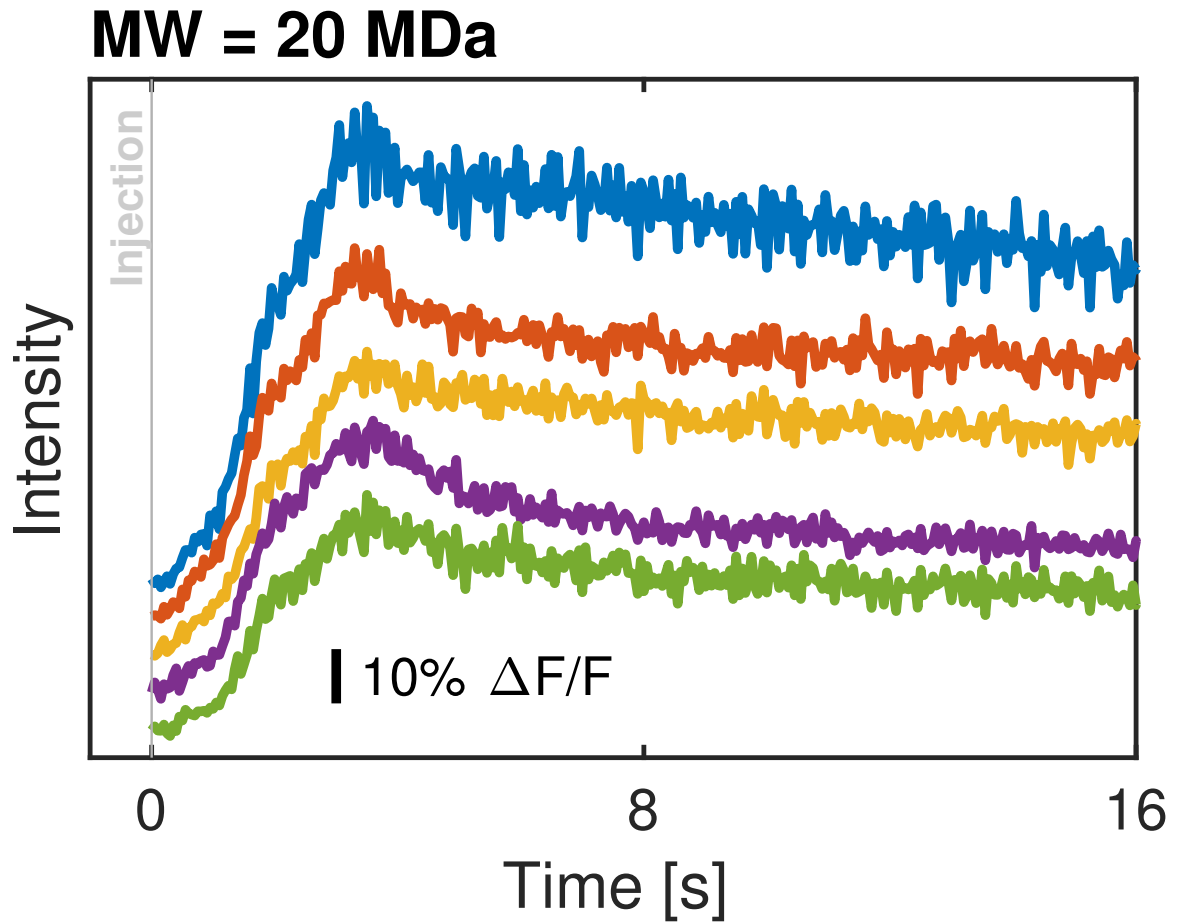


Figure 4-1: Detection of fluorescent agent in vasculature via implanted fibers. At time 0, the mouse received an IV injection of high molecular weight FITC retro-orbitally. Recordings via 8 μm fibers show an immediate and sustained increase in fluorescence. Each line is the $\Delta F/F_0$ intensity for a single fiber from the recording.

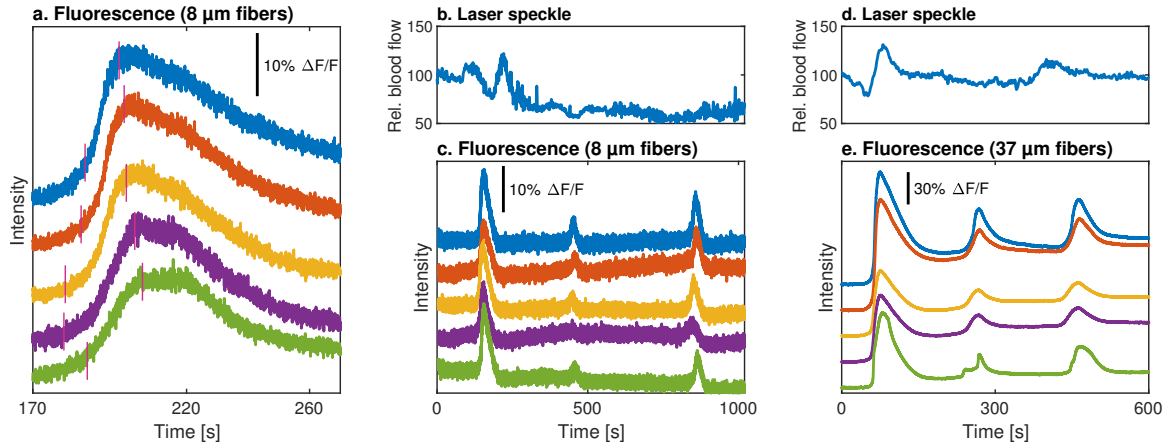


Figure 4-2: Cortical spreading depolarization (CSD) evokes a fluorescence increase. Three recordings from Thy1-GCaMP6f mice implanted with fibers after dissolving a pellet of KCl on the surface of the brain. Each line is the $\Delta F/F$ intensity for a single fiber from the recording. Within three minutes of application, a distinct fluorescence increase is visible. By recording relative blood flow via laser speckle, it is possible to confirm the presence of a CSD. (a) Fluorescence associated with a single CSD, recorded via 8 μm fibers. (b) and (c) Synchronized recording of laser speckle and fiber fluorescence via 8 μm fibers, showing a CSD and two subsequent fluorescent events. (d) and (e) Synchronized recording of laser speckle and fiber fluorescence via 37 μm fibers, showing two CSDs and an additional fluorescent event in between.

its sensitivity profile.

As a CSD propagates across the cortex at approximately 2 mm per minute (Ochs and Hunt, 1960; Pietrobon and Moskowitz, 2014), we can look at the acquired images of the fiber bundle for timing differences in fiber fluorescence that corresponds with this propagation. Figure 4-3 shows frames from the acquired video, illustrating the propagation of the CSD.

Relative blood flow measured via laser speckle near the fiber implant site provided confirmation of the CSD. Because the laser speckle was recorded at a second location, there is a time offset associated with the CSD propagation. The CSDs identified via blood flow correspond closely with recorded fluorescence increases, but we also observe

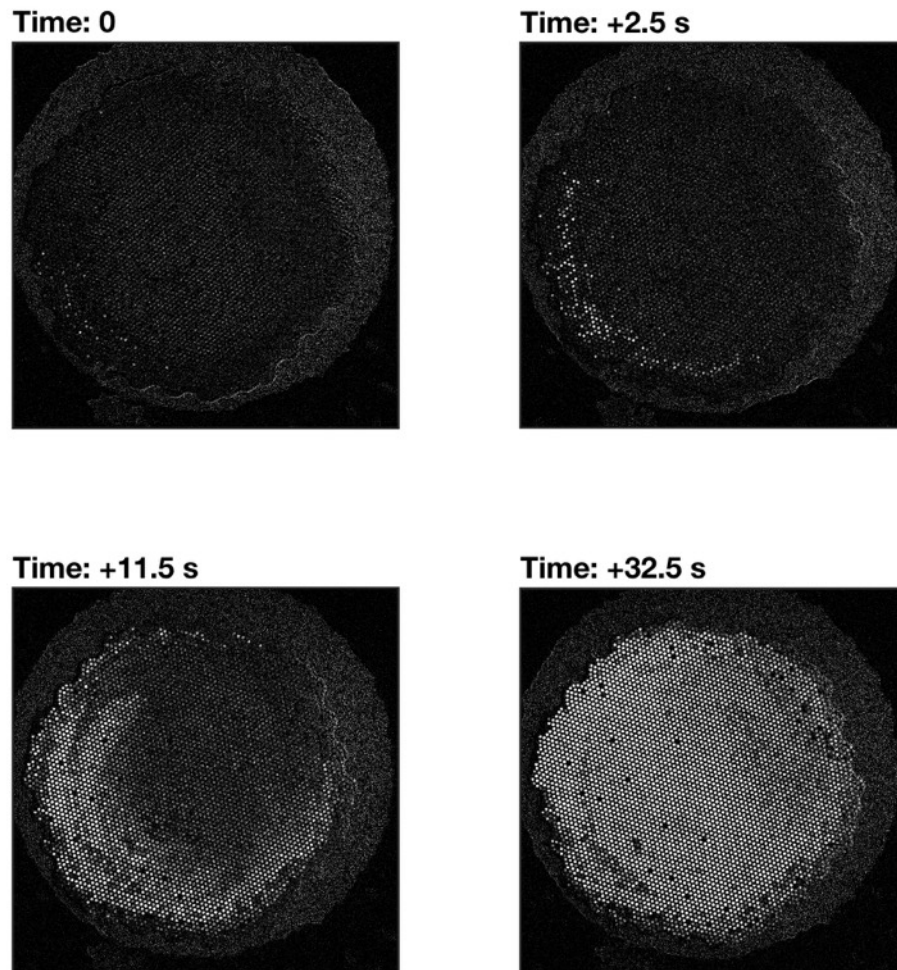


Figure 4.3: Frames of polished imaging surface show progression of cortical spreading depolarization (CSD). Three minutes after dissolving a KCl pellet on the brain of a Thy1-GCaMP6f mouse, the fluorescence associated with a CSD was visible via the implanted 8 μm fibers. Four background subtracted frames selected from the first 33 seconds of the CSD show the spatial propagation of the depolarization.

additional subsequent fluorescent events that do not have the corresponding change in relative blood flow.

For the 8 μm fibers, the observed fluorescence increase is $0.154\times$ the F_0 intensity (std. dev. 0.03) in the 25 brightest fibers. For the 37 μm fibers, the increase is $0.577\times$ the F_0 intensity (std. dev. 0.19).

Sensory evoked activity. To record fluorescence evoked by sensory stimulation, we recorded from the primary somatosensory region of cortex of a transgenic mouse expressing a calcium sensitive fluorescent probe while electrically stimulating the contralateral forepaw. We align and average fluorescence from 0.4 s before until 1.6 s after the stimulation pulse. When recording from the 8 μm fibers, we did not observe fluorescent activity corresponding with the stimulation pulses. When recording from the 37 μm fibers, we see a small, but significant increase in fluorescence over baseline for two fibers (figure 4.4). The increase in fluorescence averages $0.001\times$ the F_0 intensity ($p \leq 0.005$), based on 100 aligned stimulation pulses.

4.4 Discussion

These initial recordings demonstrate the potential utility of bundles of optical microfibers as a method for recording fluorescence activity; each fiber delivers excitation light and samples fluorescence from a small region of tissue at the fiber aperture.

First, we demonstrate the ability to sense a fluorescent agent in the vasculature by intravenously injecting high molecular weight FITC. This initial proof of concept shows the fibers are functional and sensitive to a high fluorescence event, and may have promise for recording dynamics associated with the vasculature.

Next, we turn our attention to sensing genetically-expressed fluorescent probes (in this case, GCaMP6). In these experiments, we explore the most intriguing aspect of the splaying optical fiber bundles, where the fibers can sample neural activity

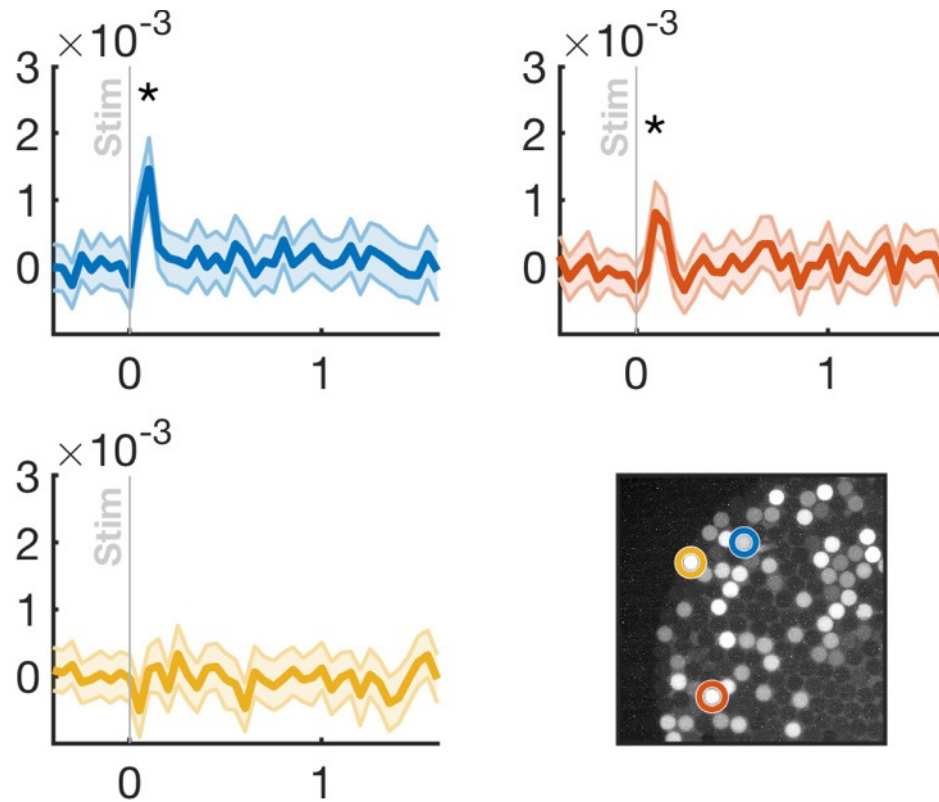


Figure 4-4: During forepaw stimulation, two 37 μm fibers show time locked fluorescent activity. The three traces show stimulation-aligned average fluorescent intensity of distinct fibers after background subtraction over 100 trials. The fibers are implanted in primary somatosensory region of a Thy1-GCaMP6s mouse, and the contralateral forepaw receives a 20 ms, 1.2 mA pulse at time 0. The shaded region representing the 95% confidence interval by bootstrapping trials. The top two traces have a significant increase in fluorescence over pre-trial frames (t-test, $p \leq 0.005$). Bottom, right: image of the polished imaging surface with the three corresponding fibers highlighted.

throughout a 3D volume of tissue while retaining intact neurons in close proximity to the fibers and, as a result, decreasing the likelihood of a large tissue response that may interfere with local connectivity and network dynamics (see section 2.3.1).

During a bright and distributed event such as a CSD, we see a distinct increase in fluorescence that is consistent with previously described calcium dynamics during CSD (Gniel and Martin, 2010). The change in fluorescence was bright—clearly visible while recording, before application of any preprocessing steps such as background subtraction. In addition to seeing the fluorescence corresponding with CSDs identified via the laser speckle recording, we see additional, subsequent increases in calcium fluorescence that do not have an accompanying change in blood flow. This potentially suggests repeated influxes of calcium and/or depolarization that may warrant additional investigation.

The CSD recordings also allow a comparison across the two types of fibers. When using the larger diameter fibers (37 μm), the change in fluorescence is almost four times greater than when using the smaller diameter fibers (8 μm). This is consistent with the wider aperture enabling greater light acceptance. From the greater sensitivity of the large fibers, we can observe additional dynamics in the fluorescence; specifically, after the first CSD-evoked fluorescence increase, the fluorescence does not fully return to baseline. This may reflect the fact that intracellular calcium levels drop quickly after the CSD, but full restoration of pre-CSD concentrations takes more than 5 minutes, or may reflect variability in the response to the CSD across cortical layers (Gniel and Martin, 2010).

We observed CSDs in four of the five animals following application of the KCl. Two of the five animals expressed GCaMP3 (as opposed to GCaMP6f) and were excluded from the quantification of brightness given the different properties of the fluorescent probe. In one of these GCaMP3 mice, we did not observe an increase in fluorescence

following application of the KCl pellet. We believe that if a CSD occurred, it was after our 20 minute recording session. Following the recording session, we discovered that the homeothermic blanket malfunctioned and the mouse's body temperature dropped by 2°C, which may account for the lack of CSD.

Finally, the results recording sensory evoked fluorescent activity are more mixed, in part a result of the small sample size (one animal, with two recording sessions, one in each hemisphere). With the larger diameter fibers (37 μm), we did observe statistically significant stimulation-locked fluorescence, but the $\Delta F/F$ change was orders of magnitude smaller than the CSD recording through the same fibers. For the smaller diameter fibers (8 μm), no identifiable stimulation-locked fluorescence was observed.

A number of factors likely contribute to the limited or absent fluorescent signal, and future work can improve the signal. All recordings were taken under isoflurane anesthesia, which suppresses sensory evoked cortical activity (Sitdikova et al., 2013). During the recordings, we attempted to transition to α -chloralose, but were unable to sustain the animal's anesthetized state; as a result, we continued light isoflurane, potentially interfering with the cortical response to the forepaw stimulation. During a subsequent round of recording via the larger diameter fibers, we found no stimulation-locked fluorescence, consistent with an observed deepening in the animal's anesthesia and corroborating the potential role of anesthesia in suppressing sensory evoked signals.

A second challenge is that all recordings reported here are acute. Acute recordings may be detrimentally impacted by bleeding, swelling or other acute reactions to the implant that have not yet been evaluated. Consistent with previously reported histology (section 2.3.1), we believe that the strength of the optical microfibers as an interface comes from their chronic stability. Future work will focus on building

stable chronic implants for mice to enable recording from awake, behaving animals, eliminating the effects of anesthesia and allowing the surrounding tissue to stabilize after the implant process.

Third, the fiber implant process is currently guided solely on coordinates. Given the dimpling that can occur during implant (section 2.2), the implant depth would benefit from closed loop feedback. By monitoring fluorescence while lowering the fiber bundle into the tissue, it may be possible to more precisely target a specific cortical layer.

In addition, excitation power recorded through the larger fibers may have been adversely affected by a mismatch between the objective NA (0.25) and the fiber NA (0.6), resulting in lost excitation signal. Correcting this mismatch may increase the coupling of light from the fiber into the objective, and hence may improve the recorded signal.

These initial recordings demonstrate the feasibility of bundles of hundreds or thousands of microfibers as an interface to optically access 3D volumes of tissue. Incorporating the insights from these initial recording attempts will enable improving surgical protocols and moving towards an awake, behaving paradigm. With these iterations, we hope to improve sensitivity to sensory-evoked fluorescence activity, such that it can be recorded through both the small and large diameter fibers.

Chapter 5

Interface and software for near-real-time processing and feedback

5.1 Introduction

Acute recordings from bundles of optical microfibers (chapter 4) show the potential of the interface to extend optical access to deep brain regions. The splaying fibers deliver excitation light, and collect fluorescent emissions during a cortical spreading depolarization, enabling visualizing the associated calcium dynamics and propagation of the depolarization. Yet a large part of the value proposition of the interface is the potential to record fluorescence in awake, behaving animals.

In order to achieve such recordings, a new optical configuration is required that will allow recording animals during a complex behavioral task. This necessitates a way to physically manage the fibers such that the bundle is protected from physical damage, while maintaining optical access to the individual fibers and allowing the animal to freely move within their enclosure.

Specifically, we intend to use the fibers to record fluorescence activity in singing zebra finches. Their ability to freely move about their enclosure is crucial; when constrained, the animals will rarely sing. To this end, we have designed a recording interface that holds a reinforced fiber bundle in a passive commutator above the bird's enclosure. As the bird moves around its cage, the fiber can rotate below the objective of a traditional fluorescence microscope.

Custom acquisition software controls synchronized acquisition of video and analog data; in the case of the zebra finches, we use the analog data channels to record audio, which is both used for triggering acquisition and for subsequent analysis—specifically, to align calcium fluorescence across song renditions. The software is also capable of near-real-time analysis of acquired video frames, extracting fiber intensity values, which can be used to trigger behavioral feedback or create a basic brain machine interface.

Based on the design configuration used to record from seven zebra finches, each for a minimum of a week, we describe a hardware and software configuration that enables longitudinally recording fluorescence from an awake behaving animal.

5.2 Methods

Animal care and experimental procedures were approved by the Institutional Animal Care and Use Committee (IACUC) of Boston University (protocols 14-028 and 14-029). Fibers were implanted in nine zebra finches. Of those, we chronically recorded from seven birds via the fiber interface described in the next section; two were excluded due to issues with early design iterations, where the birds risked getting tangled in the fiber bundle and hence were not connected to the microscope.

5.2.1 Chronic fiber interface

To use the bundles of optical microfibers to interface with awake behaving animals, we have built and piloted a configuration where the animal is housed in an enclosure below a traditional fluorescence microscope with the ensheathed bundle running from the microscope to the animal (figure 2.1). The bundle is secured to the animal using anchor points around the craniotomy. To avoid physical stress on the optical fibers, the bundle is reinforced with a strip of polyimide (DuPont Kapton, 0.005" thick),



Figure 5-1: A diagram of a prepared polyimide strip to reinforce a chronic fiber bundle implant. A strip of polyimide is used to absorb physical stresses, protecting the bundle of fibers. The fiber bundle is threaded through the small holes and the bottom hole (right) is used to anchor the polyimide strip to the skull.

prepared as shown in figure 5-1. The strip similarly runs from the skull implant points to the fluorescence microscope above the enclosure.

The polyimide strip is cut slightly shorter than the fiber bundle, so that when the animal moves or twist, the force will be primarily exerted on the strip rather than the bundle. To secure the fiber bundle to the polyimide strip, we punched 1.5 mm holes in the strip, and thread the fiber bundle through the holes. This ensures that the slack in the fiber bundle does not dangle in a way that might interfere with the animal’s behavior.

Depending on the duration of the recording session, the fiber can either be fixed below the fluorescence microscope or can be mounted in a low-friction passive commutator, constructed from precision ball bearings (figure 5-2), that allows the fiber bundle to rotate as the animal moves. Given the flexibility of the fibers, the polyimide reinforcement strip is beneficial here to translate the rotational torque up to the commutator.

To correct for the rotation of the fiber, rotational motion correction is applied to the recorded video (described in section 5.2.4).

In situations requiring longer exposure times, the rotation of the fiber may be problematic. We tested a further variation that used a servo to apply a rubber “brake” pad to the passive commutator during recording, temporarily preventing rotation.



Figure 5-2: Commutator built with low-friction, precision ball bearings allows fiber to rotate. A passive commutator constructed with precision ball bearings holds the ferrule and polished imaging surface below a microscope objective. As the animal moves about the enclosure, the fiber can freely rotate, while remaining level in the focal plane of the microscope.

5.2.2 Acquisition hardware

The ferrule and polished imaging surface were held using a passive commutator (figure 5.2) below a traditional fluorescent microscope (Olympus, 20 \times objective) with a broadband white LED (Thorlabs SOLIS-3C) set at 100% brightness and a GFP filter cube (Semrock BrightLine GFP-4050B, 466/40 excitation, 525/50 emission, 495 dichroic). Excitation power from the objective was measured at 9.16 mW; given the core size and count, this corresponds with coupling approximately 0.3 μ W into each fiber. Fluorescence activity was recorded either with a USB compatible CMOS camera (3rd eye electronics, MC900 paired with DM420 frame capture device) configured for an exposure of 33 ms resulting in a 30 frames per second recording of 640 \times 480 8 bit pixels or with an sCMOS camera (Hamamatsu ORCA-Flash4.0 v2) configured for 2 \times 2 binning and an exposure of 50 ms, resulting in a 20 frames per second recording of 1024 \times 1024 16 bit pixels.

When recording via a standard USB CMOS, the custom acquisition software described in the next section was used to control the camera and acquire video. When using the ORCA-Flash sCMOS, the custom acquisition software triggered acquisition and recorded frame synchronization information, while the raw video stream was acquired and written to disk by HCImage (Hamamatsu) on a separate computer. This allowed isolating the data-intensive (40 megabytes per second) video acquisition from the analog signal acquisition and analysis.

5.2.3 Near-real-time software

To manage and trigger acquisition, and to do near-real-time signal processing, we created custom image acquisition software that runs on the macOS operating system (figure 5.3).¹ Leveraging the native AVFoundation framework, the software is capable

¹The software is open source and accessible at <https://github.com/gardner-lab/video-capture>

of communicating with a wide range of USB video acquisition hardware, including both analog-to-digital frame grabbers and cameras. The software can capture video or video synchronized with multi-channel analog data (including either audio or other analog data). Video and analog data are written to disk in MPEG-4 container files with video encoded at full resolution either uncompressed, or using the H.264 or lossless MJPEG Open DML codecs, and audio encoded using either the AAC codec or the Apple Lossless format with a sampling rate of up to 96 kHz. Simultaneously, the software writes metadata including frame timing, region of interest intensity and analysis parameters to a text file (CSV format).

The software also communicates with a microcontroller (Arduino Uno Rev3 or 2560 Mega) via a USB-to-serial connection. The microcontroller allows the software to control additional peripherals, including light source brightness, camera parameters (such as exposure) and the commutator.

The software is able to perform near real-time analysis on both the video frames and the analog input channels—these channels enable low-latency, video-aligned acquisition of audio, external TTL pulses, electrophysiology or behavioral data. For example, in experiments where we record fluorescence in songbirds, we use the analog channels to acquire audio and trigger acquisition based off song detection (by processing audio through a short-time Fourier transform to calculate the ratio of power in frequency bins associated with song [1–10 kHz] to the power of frequency bins outside the song range). The microcontroller is used to activate the excitation light source, restricting illumination to periods of singing and, as a result, minimizing photobleaching.

During monitoring and acquisition, the software can perform low-latency computational analysis of both the video frames and analog input. In the case of the video, the user interface provides the ability to draw regions of interest (ROIs) onto

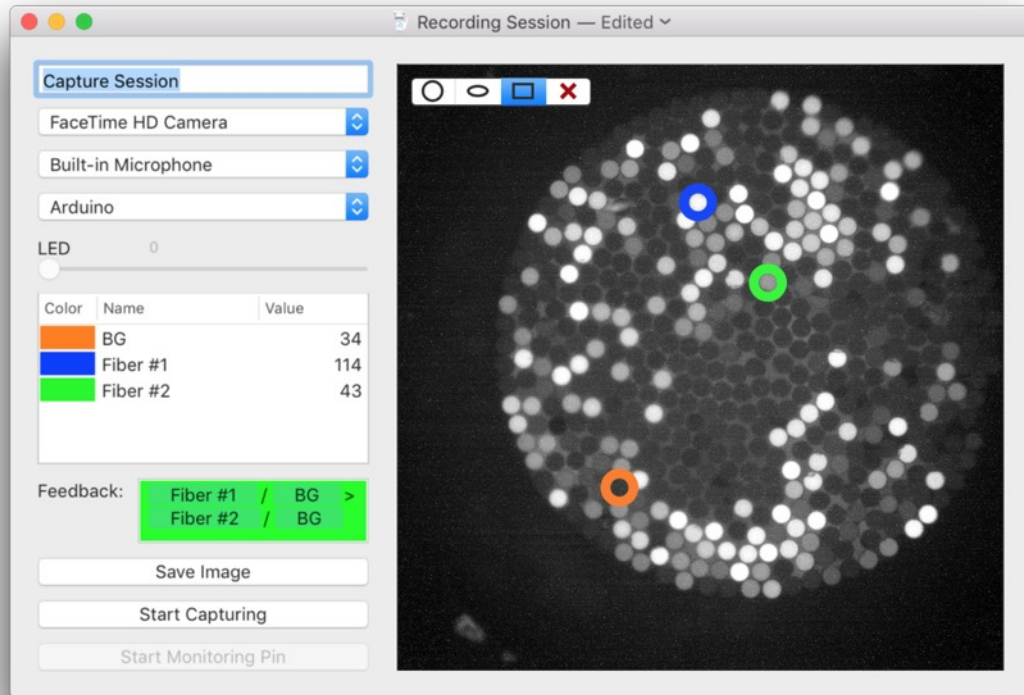


Figure 5.3: User interface of acquisition control software capable of near-real-time analysis. The software controls acquisition-related peripherals, including USB camera sensors, light sources and microcontroller breakout boxes, and manages synchronized acquisition of video and analog signals. During recording, the software can process video frames, extracting multiple annotated regions of interest, and can process analog signals, such as performing audio template matching. Analysis is used to trigger acquisition or external feedback, acting as a basic brain machine interface.

the field of view and processing rules in the form of symbolic equations that can be used to trigger external feedback (e.g., sound or reward). At the start of acquisition, the software converts the regions of interest into indices corresponding with the ROI masks and parses the symbolic equations into an abstract syntax tree (AST) for optimization and evaluation. Each frame is read in YCbCr color space, providing direct access to the luma component (Y). Using vector optimized instructions when available, the software accumulates average pixel intensity for each region of interest and then evaluates the syntax tree and outputs the appropriate feedback value. Figure 5-3 shows the software configured to compare ΔF values for two regions of interest corresponding with two fibers.

Given the broader range of analog analysis and applications, the software does not have a graphical user interface for defining analog signal analysis, but the code provides clear extension points. We have extended and open sourced versions of the software that use the analog signals to acquire and process audio. Acquired audio is converted to a spectral representation through a two-taper short-time Fourier transform (STFT). These analysis steps leverage the vDSP Accelerate framework, which utilizes vectorized instructions whenever possible to achieve low latency processing. We use the spectral representation to trigger acquisition (during singing) and to provide behavioral feedback. The spectral representation can serve as an input to a neural network trained to precisely identify salient audio (i.e., a syllable or other vocalization) (Pearre et al., 2017); upon detection, the software can provide aversive feedback (such as burst of white noise) to perturb behavior.

To evaluate the software latency, we flash an LED in the field of view of the camera, while recording the output trigger controlled by the software to measure when the LED intensity is detectable. The pulse driving the LED also triggers acquisition on an oscilloscope (Tektronix TBS 1022), which is set to averaging mode (128-trigger

average) in order to collect latency data. In addition, external logging in the software is used to evaluate processing time for specific steps in the analysis pipeline (such as ROI extraction). Audio processing is evaluated as described in (Pearre et al., 2017), using recordings of songs with a ground truth annotations on the second channel. The ground truth signal triggers oscilloscope acquisition, again averaging over 128 trials to build a distribution of timing performance.

5.2.4 Analysis pipeline

Given the large file size in chronic recordings (200 GB), we designed a custom set of tools to aid in file processing and analysis.² We created a Python script to convert the Hamamatsu CXD file format to raw binary files, allowing direct frame indexing. Next, a set of custom MATLAB classes allows composing a node based processing graph, which allows each frame to be processed in isolation, minimizing the amount of memory needed to work with the videos.

Our standard pipeline involves iterating over video frames twice. During the first pass, raw video frames are passed into a Scale-Invariant Feature Transform (SIFT) (Vedaldi and Fulkerson, 2008; Lowe, 1999; Lowe, 2004) motion correction algorithm, capable of correcting the rotation of the fiber bundle associated with the passive commutator. The transformation matrices associated with the motion correction is cached for the second pass. The motion corrected frames are passed to statistical analysis nodes. The analysis nodes accumulate statistics on each pixel, including range, mean and percentile intensities. These statistics enable identifying high variability pixels (corresponding with fibers collecting fluorescence), which can then be used to define regions of interest for subsequent analysis.

During the second pass, the algorithm again applies the motion correction trans-

²The software is open source and accessible at <https://github.com/nathanntg/fiber-pipeline> (DOI: 10.5281/zenodo.1314759)

form to each frame, and extracts the mean pixel intensity associated with each region of interest. Additional nodes in the software pipeline allow optionally applying smoothing, downsampling or background subtraction, depending on the desired output.

5.3 Results

The chronic fiber interface configuration and associated video acquisition and analysis software were used to record from seven zebra finches for 7–23 days each (mean: 17 days). The recording results are not presented here, but the sessions provided an opportunity to evaluate and revise the fiber interface for longitudinal awake behaving recordings.

5.3.1 Chronic fiber interface

The implanted fibers remained well secured over the course of the recording, and the setup provided the necessary freedom of motion to allow the birds to sing. For all seven animals, we recorded fluorescence via the fibers and synchronized audio. Acquisition was automatically triggered by singing, and the animals performed hundreds of song renditions per day.

After 23 days implanted in an awake behaving animal, we remeasured the optical attenuation. The optical attenuation of the used fibers was measured to be 6.54 dB (compared with 3.78 dB pre-recording, as measured in section 2.2.1).

5.3.2 Analysis performance

To evaluate the near-real-time analysis and feedback, we recorded signals that include a ground truth reference signal, enabling evaluation of accuracy and performance.

Region of interest (ROI) video analysis was evaluated by measuring the time from LED onset to software feedback. The average time to trigger a feedback stimulus is

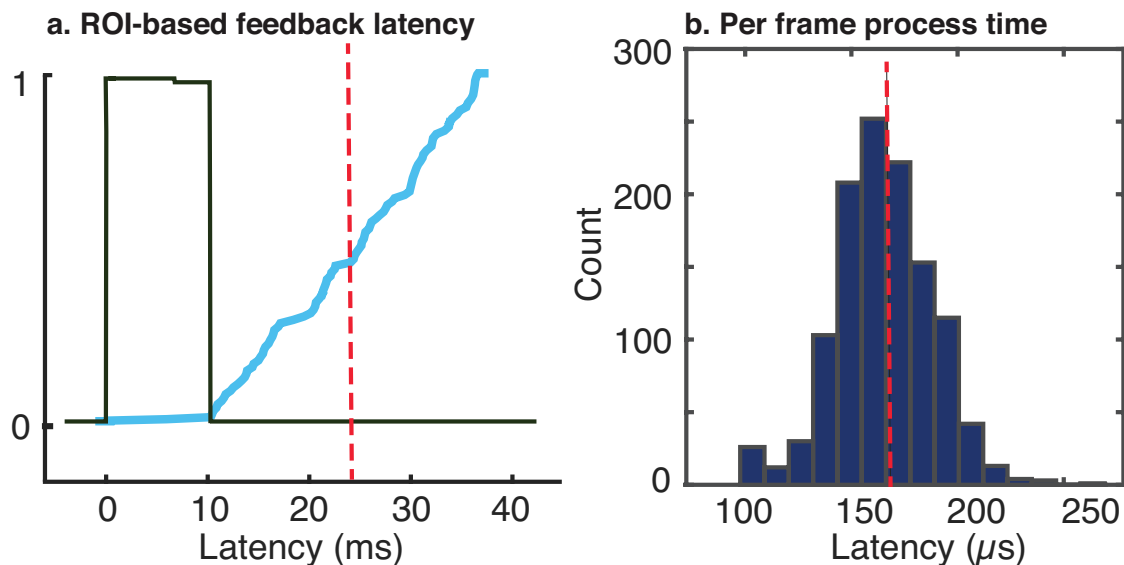


Figure 5-4: Video analysis produces feedback in 24 ms, including exposure time. To measure the latency of the video analysis functionality in the acquisition software, an LED was flashed in the field of view, while timing the delay until detection of the output TTL indicating detection. (a) Black: voltage driving LED light flash; blue: cumulative density function (CDF) of TTL output. The latency from LED activation to output TTL is 23.9 ± 3.9 ms (std. dev). This is consistent with the 33 ms exposure time. (b) Of the total latency, the image processing to extract mean intensity from ten cell-sized regions of interest contributes an average of only 0.17 ms; much of the ROI feedback latency is a reflection of the frame rate and acquisition time.

23.9 ± 3.9 ms (std. dev.), including frame exposure, digitization, transmission, data acquisition and software processing. This latency reflects the intrinsic limitations of a 33 ms exposure time (which accounts for 16.5 ms of the delay) as well as the time spent capturing and decoding the video, and communicating an output TTL via the microcontroller. Figure 5-4 depicts video analysis latency.

Of the total ROI latency, we can break this down in terms of specific steps in the analysis pipeline. Data acquisition, region of interest processing, and feedback triggering all occur within an average of 1.7 ms after frame capture (95% confidence: <11 ms). This variability stems primarily from video encoding and storage, where

the codec and write buffering necessitate increased processing time for a subset of frames. An additional source of variability is processing time, which has a smaller impact and is shown in figure 5.4b, relates to the number and complexity of the defined regions of interest. As the number and size of the regions of interest increases, the processing time increases. In tests involving ten cell-sized regions of interest, the average processing time was 0.17 ± 0.03 ms (std. dev.).

For audio processing, a similar evaluation can be performed to measure average latency for a detection task. Specifically, we used a version of the acquisition software extended with a trained neural network to identify birdsong syllables (Pearre et al., 2017). The detection software was configured to process 1.5 ms chunks of audio, sending a rolling window of spectral features through the neural network to detect the target syllable. Using a recording that includes ground truth data, the latency of detection events could be compared with actual syllable presentation. Figure 5.5 shows the latency for two different TTL output modalities: upon detection, the acquisition software could either generate a TTL pulse via the connected microcontroller or generate a signal on the audio line out (useful for playing aversive white noise feedback). Via the audio line out, the average latency is 4.2 ± 2.1 ms. Via the microcontroller, the average latency is 0.0 ± 1.8 ms.

5.4 Discussion

Given the challenges of connectorizing or aligning fiber bundle ferrules, each with a lattice of thousands of individual fibers, we have developed and described an approach to perform chronic recordings in awake behaving animals by placing the enclosure below a fluorescence microscope. Custom software is then used to either manually or automatically trigger acquisition during a behavioral paradigm, recording video of fluorescence activity and, when applicable, synchronized analog data (such as audio).

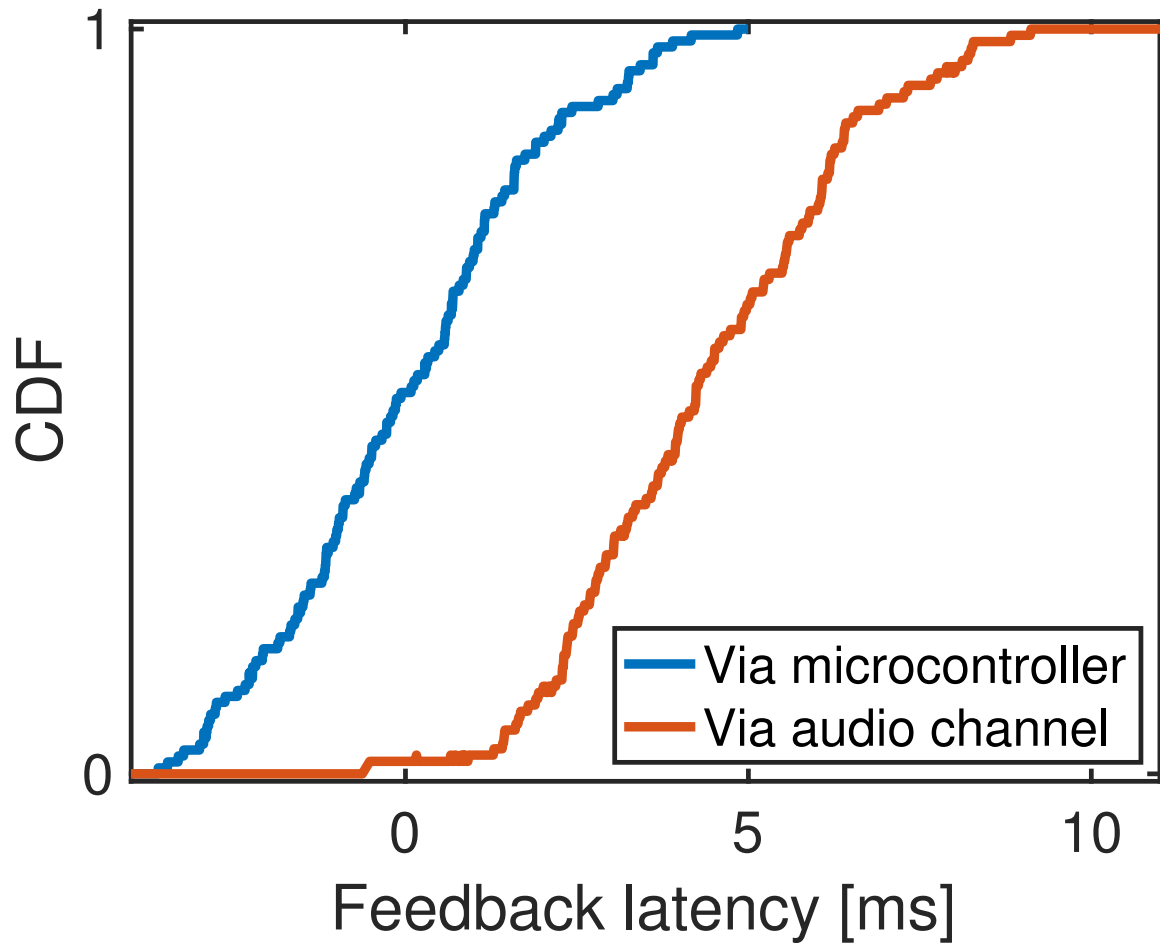


Figure 5-5: Audio analysis produces feedback in under 5 ms. The acquisition software extended with a neural network based syllable detection tool, was evaluated on annotated data, allowing measurement of the latency between actual syllable presentation and the detection TTL pulse. If the TTL pulse was delivered via the attached microcontroller, average latency was 0.0 ± 1.8 ms; if delivered via the audio line out, the latency increased to 4.2 ± 2.1 ms.

The software has the ability to do low latency processing of both video and analog signals, which can be used to control acquisition or provide feedback to the animal.

Using this setup, we were able to chronically monitor seven birds and trigger acquisition based off singing. Assessment of the fibers after three weeks of acquisition show an increase in attenuation, suggesting that even with the polyimide reinforcement strip, either the implant or recording process results in wear and tear on the bundles of optical microfibers, increasing attenuation. It may be valuable to collect more measurements to track the decline in attenuation, and potentially improve the chronic interface configuration to better protect the fibers.

With software capable of near-real-time analysis of fluorescence activity, the fibers can be used as a brain machine interface (BMI) in which an animal controls an external device through the calcium fluorescence measured via the implanted fibers; for example, this could be used to allow songbirds direct control over sound generation (Clancy et al., 2014). Other applications of the software could include closed-loop stimulation experiments that seek to optically disrupt specific patterns of activity when detected.

In our tests, the latency of triggering off fluorescence activity was limited by the sensor of the camera, about 23.9 ± 3.9 ms (figure 5.4). For many experiments, this response latency is acceptable. In the songbird, for example, the sensory-motor latency from pre-motor neural activity in HVC to sensory evaluation of the auditory signal processed in the basal ganglia is a minimum of 32–50 ms (Andalman and Fee, 2009). Based on these estimates and published accounts of conditional feedback experiments in songbirds, the time-delay should provide a learnable brain machine interface (Ölveczky et al., 2005; Tumer and Brainard, 2007; Sakata and Brainard, 2008; Sober and Brainard, 2009). However it remains to be seen whether the timing jitter in the current configuration is acceptable for brain machine interface experiments in a

system as precise as the songbird. For the zebra finch, relative jitter between premotor commands and auditory feedback is just a few milliseconds. For some experiments, lower latency and lower variability may be desirable, which can be achieved through a shorter exposure (higher frame rate). To further decrease jitter, the acquisition process can potentially be moved to a deterministic real-time operating system.

Chapter 6

Conclusions

6.1 Splaying optical microfibers as an interface

In this thesis, we have introduced a novel deep brain optical interface. Rather than using a single monolithic implant, the presented bundles of optical microfibers have a smaller cross section and greater flexibility. During insertion, each fiber moves independently, splaying throughout the tissue. The other end of the fibers are arrayed in a regular lattice on a polished imaging surface that can be readily mounted under a traditional fluorescence microscope. As each fiber has a core and cladding, achieving near total internal reflection, the fiber carries light to the aperture, where it can optically interface with a small region of tissue.

In chapter 2, we reviewed the fiber configuration, surgery and histology. Results from implanted zebra finches showed that at a depth of around 3 mm, a bundle of a hundreds or thousands of fibers spreads over 1 mm in diameter with each fiber sampling fluorescent activity from small regions of tissue distributed across a larger 3D volume. The immunohistochemistry finds neurons in close proximity to the fiber tips in animals chronically implanted, showing less tissue impact than comparable results from larger diameter, rigid electrode implants. These results are a promising indication of the preservation of local connectivity and network dynamics.

Based on the distribution of fibers seen in the histology, we modeled the interface properties in chapter 3. As the number of fibers increases and, hence, the density of fibers, a bundle will deliver more uniform excitation power to the tissue and neigh-

boring fibers will have greater overlap in the collected signals. Under such conditions, it becomes possible to apply blind source separation techniques to extract individual neural contributions. By combining knowledge of the underlying fluorescent indicator waveform and mixing process, we use a form of non-negative independent component analysis to unmix simulated neural activity.

In chapter 4, we presented initial *in vivo* recording data from mice, including fluorescence collected due to both intravenously injected agents and induced cortical spreading depolarizations. In addition, we showed fluorescent activity time locked to sensory stimulus when using larger diameter fibers. These signals demonstrate potential for the fiber bundles as a recording interface, but also highlight additional areas for improvement (such as refining the optics to achieve a higher contrast to background ratio) and reproducing the same success using smaller diameter fibers.

Finally, in chapter 5, we presented a recording configuration developed to chronically interface with animals via the bundles of optical microfibers, including a commutator and acquisition platform capable of synchronized video and analog data capture. Near-real-time analysis software allows processing acquired signal, and can be used to present feedback or run brain machine interface experiments.

Overall, we believe that the bundles of optical microfibers achieves a unique set of tradeoffs for optically interfacing with deep brain regions. Small, flexible optical microfibers preserve more of the connectivity and dynamics in adjacent brain regions, while extending optical access in a way that enables freely behaving experimental paradigms. For our work in zebra finches, this allows recording from birds without constraining them in a way that discourages or prevents singing; yet we anticipate that these same benefits will translate to additional species and systems neuroscience inquiries.

6.2 Future work

This work has presented a new implant and technique for deep brain imaging, along with a basic survey of relevant histology, modeling and initial recordings. But these are early steps, and future work will continue to adapt this technique to new use cases and greater potential.

6.2.1 Additional in vivo recordings

In chapter 4, we presented initial in vivo recordings showing fluorescence activity from intravenously injected fluorescent agents and from genetically encoded calcium indicators during both a cortical spreading depolarization and a forepaw stimulation experiment. The forepaw results are promising, but also highlight challenges in terms of contrast-to-noise and the need to move to chronic implants with awake behaving mice.

More work is needed to adapt the chronic recording interface described in chapter 5 to new animal models, including mice. The dexterity of mice and their tendency to chew on objects necessitates more active protection of the fiber implant.

Such an interface will allow collecting additional sensory-evoked fluorescence activity, without the potential confounds of anesthesia. Being able to repeat recordings in chronically implanted animals will allow the brain to recover post-implant and will provide an opportunity for testing design iterations to understand how they impact signal quality.

With further refinement, the technique can eventually be applied to fundamental systems neuroscience questions in deep brain regions.

6.2.2 Controlling implant and splay

The splaying properties of the fibers have been evaluated with a specific deep brain region in mind—the basal ganglia of the zebra finch. But from the histology, we observe variability in the distribution of the fibers at a depth of 3 mm. Further analysis and technique development may provide greater control over the splay, potentially reducing variability and improving the compatibility of the optical microfibers with shallower or deeper implants. Specifically, it may be beneficial to construct a mesh or perforated structure that can be mounted on the surface of the brain, which will serve to both pre-splay and reinforce the fibers prior to their entering the tissue. Such a structure may enable more reproducible splaying patterns.

In addition, such a structure may benefit implants at different depths. Currently, much of the fiber distribution comes from the slow spreading process as the fibers are lowered through the tissue. For shallower implants, pre-splaying the fibers will ensure a wide distribution without requiring the depth to achieve the fiber distribution. For deeper implants, fibers longer than 5 mm are more likely to buckle. By having a structure around the fibers before they come into contact with the tissue, it may reinforce the fibers and reduce the chance of buckling when accessing regions at a depth greater than 5 mm.

6.2.3 Stimulation and structured illumination

The splaying optical microfibers have the ability to both deliver excitation light to the tissue, and to collect fluorescent emissions from neurons surrounding the fiber aperture. In concert, this enables fluorescent recording, which has been the primary focus of this effort. But given that the fibers can deliver excitation light, they also provide a compelling interface for manipulating neural activity using opsins or other light-gated ion channels.

Collectively, illumination of the full bundle can modulate neural activity across a large region. But the real potential of the bundles as a stimulation interface comes from selectively illuminating a subset of the fibers, enabling precise activation or silencing of a small number of neurons (see the modeling in section 2.3.2). Specifically, coupling 2.5 μW of 470 nm light into a fiber should provide sufficient optical power to activate channelrhodopsin over a 18,000 μm^3 region surrounding the tip of the fiber.

This becomes especially powerful when combined with fluorescent imaging, using a fluorescent indicator with orthogonal wavelengths. Imaging during a behavior enables identifying those fibers which pick up motor or sensory locked activity; then selective silencing of those neurons via stimulation can help disambiguate their contribution to the behavior. The multimode fibers enable a bidirectional interface, allowing simultaneous fluorescence imaging and stimulation.

For stimulation, a similar configuration can be used to the chronic recording interface described in chapter 5. But rather than focusing excitation light across the full fiber bundle, a digital micromirror device (DMD) can be used to project patterned light onto the polished imaging surface at the end of the fiber bundle. If mounted on a commutator, real time registration or a rotation encoder can enable adapting the stimulation pattern to the rotational position of the fiber.

6.2.4 Multiplexing

In addition to enabling patterned stimulation, structured illumination may have the potential to enable better source separability during recording by iterating through illumination patterns. Inspired by the increased resolution achievable using structured illumination microscopy (Gustafsson, 2000; Gustafsson, 2005; Saxena et al., 2015), we believe that there may be potential to “multiplex” activity by rotating through different patterns that illuminate distinct permutations of the fiber bundle.

Each illumination pattern will correspond with a distinct mixing matrix, based on

the differences in excitation power. Applying the same source separation techniques described in chapter 3, it should be possible to estimate each of the mixing matrices and, as a result, separate out more of the underlying neurons contributing to the fluorescence.

Under such a multiplexed recording paradigm, there will be a tradeoff between decreased overall excitation (due to illuminating only a subset of the fibers) and less temporal resolution (as some neural activity may be lost in the time before returning to a specific illumination pattern). As a result, such recording may benefit from using modeling to identify an optimal tradeoff between number of illumination patterns and excitation power, and from using a slower time course fluorescent indicator (e.g., GCaMP6s).

6.2.5 Head mounted optics

As with the move toward head-mounted miniature microscopes to record fluorescent activity (Ghosh et al., 2011; Cai et al., 2016; Liberti III et al., 2017), the bundles of splaying optical microfibers may be most useful once the recording infrastructure is sufficiently adapted to a head-mounted recording configuration. At least initially, this would most likely apply to recording or bulk stimulation, which have similar requirements to existing miniature microscopes.

The design of a miniature fluorescence microscope closely mirrors the larger fluorescence microscopes we use to image through the fiber bundles (figure 6.1). An LED light source provides excitation light through an excitation filter and dichroic, while fluorescent emissions return, passing through the dichroic and an emission filter to a CMOS. Existing miniature microscopes benefit from open and adaptable designs (Cai et al., 2016; Liberti III et al., 2017), and with potential modifications to the optical path to couple light into the fiber bundle, may provide a small, low cost option for chronically imaging fluorescent activity in awake behaving animals.

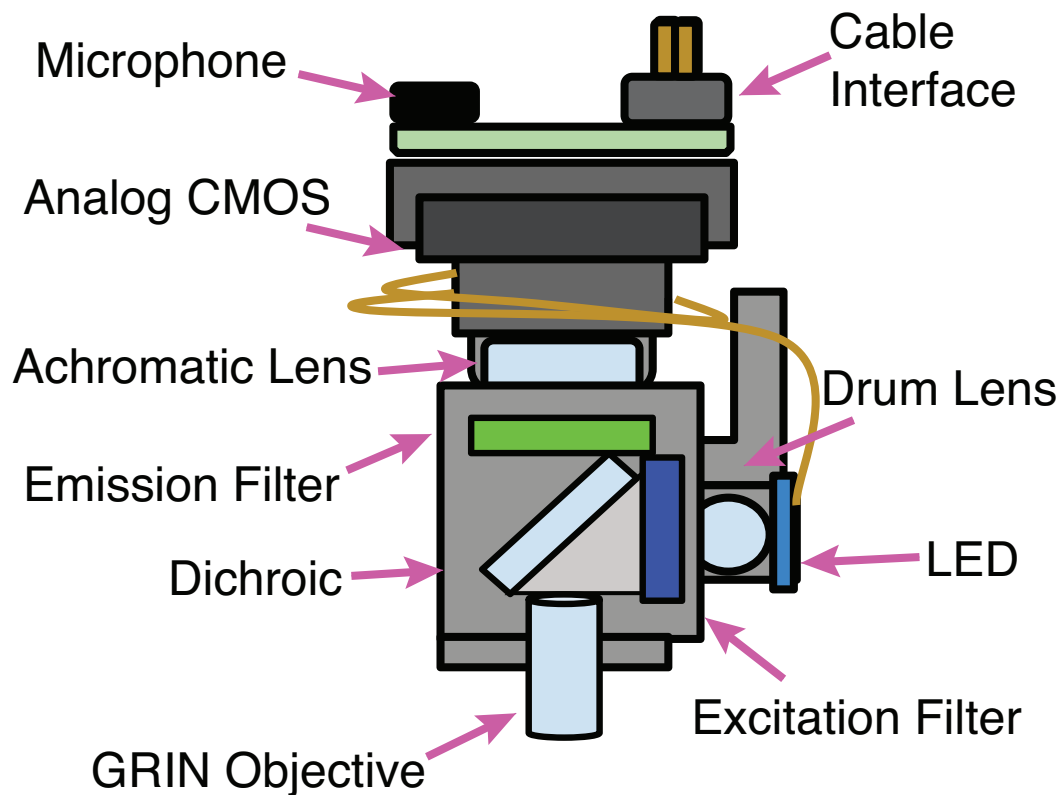


Figure 6-1: Miniature, head-mounted microscope with potential to record from fiber bundle. Existing head-mounted miniature microscopes have a compact design modeled on traditional single photon fluorescence microscopy. By adapting the objective optics, such a configuration could provide a stable, chronic interface for imaging through a bundle of optical microfibers. (Liberti III et al., 2017)

The biggest challenge to building a head mounted microscope for imaging via the fiber bundles is ensuring sufficient sensitivity to measure fluorescent signals and, ideally, to enable processing the signals via the described source separation techniques. As shown in chapter 4, existing sensory-evoked recordings have a low CBR, necessitating highly sensitive sensors and low noise recording environments. With further work, it may be possible to improve the CBR and may move into a regime where the fibers are compatible with the optics and sensors available for headed mounted microscopy.

If achieved, a head mounted microscope interface for recording from the fibers would offer a number of advantages and overcome some of the chronic recording challenges described in chapter 5. Specifically, an animal could be implanted such that only the fiber ferrule was exposed above the skull. The miniature microscope could either be permanently or temporarily fixed above the ferrule and polished imaging surface; if temporarily fixed, the fiber ferrule should likely be secured under a protective cap when the microscope is not in place to protected against accidental damage. Such a configuration would eliminate the vulnerable fibers and the risk of physical stress on the bundle. The shorter fibers will have less attenuation, and likely less degradation in attenuation over time. And given that the optics and microscope are fixed to the head, this would eliminate the need for both the optical commutator and the need to correct rotational motion (an electric commutator or wireless miniature microscope would still be needed). Overall, a head-mounted recording configuration has tremendous potential for longitudinally interfacing with awake behaving animals, without the risk of the animal getting tangled or damaging the fibers.

References

- The Meaning and Use of the Area under a Receiver Operating Characteristic (ROC) Curve. *pubs.rsna.org*.
- Adelsberger, H., Garaschuk, O., and Konnerth, A. (2005). Cortical calcium waves in resting newborn mice. *Nature Neuroscience*, 8(8):988–990.
- Adelsberger, H., Zainos, A., Alvarez, M., Romo, R., and Konnerth, A. (2014). Local domains of motor cortical activity revealed by fiber-optic calcium recordings in behaving nonhuman primates. *Proceedings of the National Academy of Sciences of the United States of America*, 111(1):463–468.
- Al-Juboori, S. I., Dondzillo, A., Stubblefield, E. A., Felsen, G., Lei, T. C., and Klug, A. (2013). Light Scattering Properties Vary across Different Regions of the Adult Mouse Brain. *PloS one*, 8(7):e67626–9.
- Andalman, A. S. and Fee, M. S. (2009). A basal ganglia-forebrain circuit in the songbird biases motor output to avoid vocal errors. *Proceedings of the National Academy of Sciences of the United States of America*, 106(30):12518–12523.
- Andermann, M. L., Gilfoy, N. B., Goldey, G. J., Sachdev, R. N. S., Wölfel, M., McCormick, D. A., Reid, R. C., and Levene, M. J. (2013). Chronic Cellular Imaging of Entire Cortical Columns in Awake Mice Using Microprisms. *Neuron*, 80(4):900–913.
- Atherton, T. J. and Kerbyson, D. J. (1999). Size invariant circle detection. *Image and Vision Computing*, 17(11):795–803.
- Ayberk Kurt, M., Ilker Kafa, M., Dierssen, M., and Ceri Davies, D. (2004). Deficits of neuronal density in CA1 and synaptic density in the dentate gyrus, CA3 and CA1, in a mouse model of Down syndrome. *Brain Research*, 1022(1-2):101–109.
- Barnett, L. M., Hughes, T. E., and Drobizhev, M. (2017). Deciphering the molecular mechanism responsible for GCaMP6m’s Ca²⁺-dependent change in fluorescence. *PloS one*, 12(2):e0170934–24.
- Barretto, R. P. J., Messerschmidt, B., and Schnitzer, M. J. (2009). In vivo fluorescence imaging with high- resolution microlenses. *Nature Methods*, 6(7):511–512.

- Betley, J. N., Xu, S., Cao, Z. F. H., Gong, R., Magnus, C. J., Yu, Y., and Sternson, S. M. (2015). Neurons for hunger and thirst transmit a negative-valence teaching signal. *Nature*, 521(7551):180–185.
- Biran, R., Martin, D. C., and Tresco, P. A. (2005). Neuronal cell loss accompanies the brain tissue response to chronically implanted silicon microelectrode arrays. *Experimental Neurology*, 195(1):115–126.
- Boas, D. A., Culver, J., Stott, J., and Dunn, A. (2002). Three dimensional Monte Carlo code for photon migration through complex heterogeneous media including the adult human head. *Optics express*, 10(3):159–170.
- Bottjer, S. W., Glaessner, S. L., and Arnold, A. P. (1985). Ontogeny of brain nuclei controlling song learning and behavior in zebra finches. *Journal of Neuroscience*, 5(6):1556–1562.
- Bouchet, A., Lemasson, B., Le Duc, G., Maisin, C., Bräuer-Krisch, E., Siegbahn, E. A., Renaud, L., Khalil, E., Rémy, C., Poillot, C., Bravin, A., Laissue, J. A., Barbier, E. L., and Serduc, R. (2010). Preferential effect of synchrotron microbeam radiation therapy on intracerebral 9L gliosarcoma vascular networks. *International journal of radiation oncology, biology, physics*, 78(5):1503–1512.
- Boyden, E. S., Zhang, F., Bamberg, E., Nagel, G., and Deisseroth, K. (2005). Millisecond timescale, genetically targeted optical control of neural activity. *Nature Neuroscience*, 8(9):1263–1268.
- Burgess, S. A., Bouchard, M. B., Yuan, B., and Hillman, E. M. C. (2008). Simultaneous multiwavelength laminar optical tomography. *Optics letters*, 33(22):2710–2712.
- Cai, D. J., Aharoni, D., Shuman, T., Shobe, J., Biane, J., Song, W., Wei, B., Veshkini, M., La-Vu, M., Lou, J., Flores, S. E., Kim, I., Sano, Y., Zhou, M., Baumgaertel, K., Lavi, A., Kamata, M., Tuszynski, M., Mayford, M., Golshani, P., and Silva, A. J. (2016). A shared neural ensemble links distinct contextual memories encoded close in time. *Nature*, 534(7605):1–16.
- Chen, T.-W., Wardill, T. J., Sun, Y., Pulver, S. R., Renninger, S. L., Baohan, A., Schreiter, E. R., Kerr, R. A., Orger, M. B., Jayaraman, V., Looger, L. L., Svoboda, K., and Kim, D. S. (2013). Ultrasensitive fluorescent proteins for imaging neuronal activity. *Nature*, 499(7458):295–300.
- Clancy, K. B., Koralek, A. C., Costa, R. M., Feldman, D. E., and Carmena, J. M. (2014). Volitional modulation of optically recorded calcium signals during neuroprosthetic learning. *Nature Neuroscience*, 17(6):807–809.

- Collombet, J.-M., Masqueliez, C., Four, E., Burckhart, M.-F., Bernabé, D., Baubichon, D., and Lallement, G. (2006). Early reduction of NeuN antigenicity induced by soman poisoning in mice can be used to predict delayed neuronal degeneration in the hippocampus. *Neuroscience Letters*, 398(3):337–342.
- Cui, G., Jun, S. B., Jin, X., Pham, M. D., Vogel, S. S., Lovinger, D. M., and Costa, R. M. (2013). Concurrent activation of striatal direct and indirect pathways during action initiation. *Nature*, 494(7436):238–242.
- D&A Instrument Company (text), Linda Worlton (layout) (2008). Light Absorption and Scattering in Water Samples Application Note. pages 1–6.
- Dana, H., Mohar, B., Sun, Y., Narayan, S., Gordus, A., Hasseman, J. P., Tsegaye, G., Holt, G. T., Hu, A., Walpita, D., Patel, R., Macklin, J. J., Bargmann, C. I., Ahrens, M. B., Schreiter, E. R., Jayaraman, V., Looger, L. L., Svoboda, K., and Kim, D. S. (2016). Sensitive red protein calcium indicators for imaging neural activity. *eLife*, 5:e12727.
- Deisseroth, K., Feng, G., Majewska, A. K., Miesenböck, G., Ting, A., and Schnitzer, M. J. (2006). Next-generation optical technologies for illuminating genetically targeted brain circuits. *The Journal of neuroscience : the official journal of the Society for Neuroscience*, 26(41):10380–10386.
- Deku, F., Cohen, Y., Joshi-Imre, A., Kanneganti, A., Gardner, T. J., and Cogan, S. (2017). Amorphous silicon carbide ultramicroelectrode arrays for neural stimulation and recording. *Journal of Neural Engineering*, pages 1–21.
- Denk, W., Strickler, J. H., and Webb, W. W. (1990). Two-photon laser scanning fluorescence microscopy. *Science (New York, N.Y.)*, 248(4951):73–76.
- Dombeck, D. A., Harvey, C. D., Tian, L., Looger, L. L., and Tank, D. W. (2010). Functional imaging of hippocampal place cells at cellular resolution during virtual navigation. *Nature Neuroscience*, 13(11):1433–1440.
- Duan, W., Zhang, Y.-P., Hou, Z., Huang, C., Zhu, H., Zhang, C.-Q., and Yin, Q. (2015). Novel Insights into NeuN: from Neuronal Marker to Splicing Regulator. *Molecular Neurobiology*, 53(3):1637–1647.
- Dunn, A. K., Bolay, H., Moskowitz, M. A., and Boas, D. A. (2001). Dynamic imaging of cerebral blood flow using laser speckle. *Journal of cerebral blood flow and metabolism : official journal of the International Society of Cerebral Blood Flow and Metabolism*, 21(3):195–201.
- Emiliani, V., Cohen, A. E., Deisseroth, K., and Hausser, M. (2015). All-Optical Interrogation of Neural Circuits. *Journal of Neuroscience*, 35(41):13917–13926.

- Flusberg, B. A., Jung, J. C., Cocker, E. D., Anderson, E. P., and Schnitzer, M. J. (2005). In vivo brain imaging using a portable 3.9 gram two-photon fluorescence microendoscope. *Optics letters*, 30(17):2272–2274.
- Freire, M. A. M., Morya, E., Faber, J., Santos, J. R., Guimaraes, J. S., Lemos, N. A. M., Sameshima, K., Pereira, A., Ribeiro, S., and Nicolelis, M. A. L. (2011). Comprehensive Analysis of Tissue Preservation and Recording Quality from Chronic Multielectrode Implants. *PloS one*, 6(11):e27554–15.
- Gerstner, K., Plichta, A., Schlatterbeck, D., Weisser, M., Brix, P., Sommer, M., Rubino Jr, R. A., Bonja, J. A., Strack, R., Henze, I., and Arsenault, P. (2004). Leached fiber bundle and method. US Patent Office.
- Ghosh, K. K., Burns, L. D., Cocker, E. D., Nimmerjahn, A., Ziv, Y., Gamal, A. E., and Schnitzer, M. J. (2011). Miniaturized integration of a fluorescence microscope. *Nature Methods*, 8(10):871–878.
- Gniel, H. M. and Martin, R. L. (2010). Changes in membrane potential and the intracellular calcium concentration during CSD and OGD in layer V and layer II/III mouse cortical neurons. *Journal of Neurophysiology*, 104(6):3203–3212.
- Gong, Y., Huang, C., Li, J. Z., Grewe, B. F., Zhang, Y., Eismann, S., and Schnitzer, M. J. (2015). High-speed recording of neural spikes in awake mice and flies with a fluorescent voltage sensor. *Science (New York, N.Y.)*, 350(6266):1361–1366.
- Goss-Varley, M., Dona, K. R., McMahan, J. A., Shoffstall, A. J., Ereifej, E. S., Lindner, S. C., and Capadona, J. R. (2017). Microelectrode implantation in motor cortex causes fine motor deficit: Implications on potential considerations to Brain Computer Interfacing and Human Augmentation. *Scientific Reports*, 7(1):1–12.
- Guitchounts, G., Markowitz, J. E., Liberti III, W. A., and Gardner, T. J. (2013). A carbon-fiber electrode array for long-term neural recording. *Journal of Neural Engineering*, 10(4):046016–14.
- Gunaydin, L. A., Grosenick, L., Finkelstein, J. C., Kauvar, I. V., Fenno, L. E., Adhikari, A., Lammel, S., Mirzabekov, J. J., Airan, R. D., Zalocusky, K. A., Tye, K. M., Anikeeva, P., Malenka, R. C., and Deisseroth, K. (2014). Natural neural projection dynamics underlying social behavior. *Cell*, 157(7):1535–1551.
- Guo, Q., Zhou, J., Feng, Q., Lin, R., Gong, H., Luo, Q., Zeng, S., Luo, M., and Fu, L. (2015). Multi-channel fiber photometry for population neuronal activity recording. *Biomedical Optics Express*, 6(10):3919–13.
- Gustafsson, M. G. (2000). Surpassing the lateral resolution limit by a factor of two using structured illumination microscopy. *Journal of microscopy*, 198(Pt 2):82–87.

- Gustafsson, M. G. L. (2005). Nonlinear structured-illumination microscopy: wide-field fluorescence imaging with theoretically unlimited resolution. *Proceedings of the National Academy of Sciences*, 102(37):13081–13086.
- Hahnloser, R. H. R., Kozhevnikov, A. A., and Fee, M. S. (2002). An ultra-sparse code underlies the generation of neural sequences in a songbird. *Nature*, 419(6902):65–70.
- Han, Z., Jin, L., Platisa, J., Cohen, L. B., Baker, B. J., and Pieribone, V. A. (2013). Fluorescent Protein Voltage Probes Derived from ArcLight that Respond to Membrane Voltage Changes with Fast Kinetics. *PloS one*, 8(11):e81295–9.
- Harris, J. P., Capadona, J. R., Miller, R. H., Healy, B. C., Shanmuganathan, K., Rowan, S. J., Weder, C., and Tyler, D. J. (2011). Mechanically adaptive intracortical implants improve the proximity of neuronal cell bodies. *Journal of Neural Engineering*, 8(6):066011–14.
- Hayn, L., Deppermann, L., and Koch, M. (2017). Reduction of the foreign body response and neuroprotection by apyrase and minocycline in chronic cannula implantation in the rat brain. *Clinical and Experimental Pharmacology and Physiology*, 44(2):313–323.
- Hayn, L. and Koch, M. (2015). Suppression of excitotoxicity and foreign body response by memantine in chronic cannula implantation into the rat brain. *Brain Research Bulletin*, 117:54–68.
- Helmchen, F., Fee, M. S., Tank, D. W., and Denk, W. (2001). A Miniature Head-Mounted Two-Photon Microscope. *Neuron*, 31(6):903–912.
- Heshmat, B., Lee, I. H., and Raskar, R. (2016). Optical brush: Imaging through permuted probes. *Scientific Reports*, 6:20217.
- Hillman, E. M. C., Boas, D. A., Dale, A. M., and Dunn, A. K. (2004). Lamellar optical tomography: demonstration of millimeter-scale depth-resolved imaging in turbid media. *Optics letters*, 29(14):1650–1652.
- Horton, N. G., Wang, K., Kobat, D., Clark, C. G., Wise, F. W., Schaffer, C. B., and Xu, C. (2013). In vivo three-photon microscopy of subcortical structures within an intact mouse brain. *Nature Photonics*, 7(3):205–209.
- Hyvärinen, A. and Oja, E. (2000). Independent component analysis: algorithms and applications. *Neural networks : the official journal of the International Neural Network Society*, 13(4-5):411–430.
- Jung, J. C., Mehta, A. D., Aksay, E., Stepnoski, R., and Schnitzer, M. J. (2004). In vivo mammalian brain imaging using one- and two-photon fluorescence microendoscopy. *Journal of Neurophysiology*, 92(5):3121–3133.

- Karatas, H., Erdener, S. E., Gursoy-Ozdemir, Y., Lule, S., Eren-Koçak, E., Sen, Z. D., and Dalkara, T. (2013). Spreading depression triggers headache by activating neuronal Panx1 channels. *Science (New York, N.Y.)*, 339(6123):1092–1095.
- Kass, R. E., Eden, U. T., and Brown, E. N. (2014). Point Processes. In *Analysis of Neural Data*, pages 563–603. Springer, New York, NY.
- Kim, T. H., Zhang, Y., Lecoq, J., Jung, J. C., Li, J., Zeng, H., Niell, C. M., and Schnitzer, M. J. (2016). Long-Term Optical Access to an Estimated One Million Neurons in the Live Mouse Cortex. *CellReports*, 17(12):3385–3394.
- Knuth, K. H. (2002). A Bayesian approach to source separation. *arXiv.org*.
- Kollias, N. and Gratzer, W. (1999). Tabulated molar extinction coefficient for hemoglobin in water. *Wellman Laboratories, Harvard Medical School, Boston*.
- Kosubek-Langer, J., Schulze, L., and Scharff, C. (2017). Maturation, Behavioral Activation, and Connectivity of Adult-Born Medium Spiny Neurons in a Striatal Song Nucleus. *Frontiers in Neuroscience*, 11:101–12.
- Kozai, T. D. Y., Langhals, N. B., Patel, P. R., Deng, X., Zhang, H., Smith, K. L., Lahann, J., Kotov, N. A., and Kipke, D. R. (2012). Ultrasmall implantable composite microelectrodes with bioactive surfaces for chronic neural interfaces. *Nature Materials*, 11(12):1065–1073.
- Krüger, J. (2010). Seven years of recording from monkey cortex with a chronically implanted multiple microelectrode. *Frontiers in Neuroengineering*, pages 1–9.
- Lee, S. A., Holly, K. S., Voziyanov, V., Villalba, S. L., Tong, R., Grigsby, H. E., Glasscock, E., Szele, F. G., Vlachos, I., and Murray, T. A. (2016). Gradient Index Microlens Implanted in Prefrontal Cortex of Mouse Does Not Affect Behavioral Test Performance over Time. *PLoS one*, 11(1):e0146533–19.
- Liberti III, W. A., Markowitz, J. E., Perkins, L. N., Liberti, D. C., Leman, D. P., Gutchounts, G., Velho, T., Kotton, D. N., Lois, C., and Gardner, T. J. (2016). Unstable neurons underlie a stable learned behavior. *Nature Neuroscience*, 19(12):1–10.
- Liberti III, W. A., Perkins, L. N., Leman, D. P., and Gardner, T. J. (2017). An open source, wireless capable miniature microscope system. *Journal of Neural Engineering*, 14(4):045001–10.
- Lin, M. Z. and Schnitzer, M. J. (2016). Genetically encoded indicators of neuronal activity. *Nature Neuroscience*, 19(9):1142–1153.
- Liu, X., Ramirez, S., Pang, P. T., Puryear, C. B., Govindarajan, A., Deisseroth, K., and Tonegawa, S. (2012). Optogenetic stimulation of a hippocampal engram activates fear memory recall. *Nature*, 484(7394):381–385.

- Long, M. A., Jin, D. Z., and Fee, M. S. (2010). Support for a synaptic chain model of neuronal sequence generation. *Nature*, 468(7322):394–399.
- Lowe, D. G. (1999). Object recognition from local scale-invariant features. In *Proceedings of the Seventh IEEE International Conference on Computer Vision*, pages 1150–1157. IEEE.
- Lowe, D. G. (2004). Distinctive Image Features from Scale-Invariant Keypoints. *International journal of computer vision*, 60(2):91–110.
- Makeig, S., Westerfield, M., Jung, T. P., Covington, J., Townsend, J., Sejnowski, T. J., and Courchesne, E. (1999). Functionally independent components of the late positive event-related potential during visual spatial attention. *Journal of Neuroscience*, 19(7):2665–2680.
- Markowitz, J. E., Liberti III, W. A., Guitchounts, G., Velho, T., Lois, C., and Gardner, T. J. (2015). Mesoscopic Patterns of Neural Activity Support Songbird Cortical Sequences. *PLOS Biology*, 13(6):e1002158–20.
- McConnell, G. C., Rees, H. D., Levey, A. I., Gutekunst, C.-A., Gross, R. E., and Bellamkonda, R. V. (2009). Implanted neural electrodes cause chronic, local inflammation that is correlated with local neurodegeneration. *Journal of Neural Engineering*, 6(5):056003–13.
- Mitianoudis, N. and Davies, M. E. (2003). Audio source separation of convolutive mixtures. *IEEE Transactions on Speech and Audio Processing*, 11(5):489–497.
- Mohammed, A. I., Gritton, H. J., Tseng, H.-a., Bucklin, M. E., Yao, Z., and Han, X. (2016). An integrative approach for analyzing hundreds of neurons in task performing mice using wide-field calcium imaging. *Scientific Reports*, 6:20986–16.
- Mukamel, E. A., Nimmerjahn, A., and Schnitzer, M. J. (2009). Automated Analysis of Cellular Signals from Large-Scale Calcium Imaging Data. *Neuron*, 63(6):747–760.
- Nagel, G., Ollig, D., Fuhrmann, M., Kateriya, S., Musti, A. M., Bamberg, E., and Hegemann, P. (2002). Channelrhodopsin-1: a light-gated proton channel in green algae. *Science (New York, N.Y.)*, 296(5577):2395–2398.
- Nakai, J., Ohkura, M., and Imoto, K. (2001). A high signal-to-noise Ca(2+) probe composed of a single green fluorescent protein. *Nature Biotechnology*, 19(2):137–141.
- Ochs, S. and Hunt, K. (1960). Apical dendrites and propagation of spreading depression in cerebral cortex. *Journal of Neurophysiology*, 23(4):432–444.

- Ölveczky, B. P., Andalman, A. S., and Fee, M. S. (2005). Vocal Experimentation in the Juvenile Songbird Requires a Basal Ganglia Circuit. *PLOS Biology*, 3(5):e153–8.
- Ozerov, A. and Fevotte, C. (2010). Multichannel Nonnegative Matrix Factorization in Convolutional Mixtures for Audio Source Separation. *IEEE Transactions on Audio, Speech and Language Processing*, 18(3):550–563.
- Pancrazio, J. J., Deku, F., Ghazavi, A., Stiller, A. M., Rihani, R., Frewin, C. L., Varner, V. D., Gardner, T. J., and Cogan, S. F. (2017). Thinking Small: Progress on Microscale Neurostimulation Technology. *Neuromodulation: Technology at the Neural Interface*, 84:203–8.
- Patel, P. R., Na, K., Zhang, H., Kozai, T. D. Y., Kotov, N. A., Yoon, E., and Chestek, C. A. (2015a). Insertion of linear 8.4 μm diameter 16 channel carbon fiber electrode arrays for single unit recordings. *Journal of Neural Engineering*, 12(4):046009.
- Patel, T. P., Man, K., Firestein, B. L., and Meaney, D. F. (2015b). Automated quantification of neuronal networks and single-cell calcium dynamics using calcium imaging. *Journal of neuroscience methods*, 243:26–38.
- Pearre, B., Perkins, L. N., Markowitz, J. E., and Gardner, T. J. (2017). A fast and accurate zebra finch syllable detector. *PloS one*, 12(7):e0181992–18.
- Pietrobon, D. and Moskowitz, M. A. (2014). Chaos and commotion in the wake of cortical spreading depression and spreading depolarizations. *Nature Reviews Neuroscience*, 15(6):379–393.
- Plumbley, M. D. (2003). Algorithms for nonnegative independent component analysis. *IEEE Transactions on Neural Networks*, 14(3):534–543.
- Pnevmatikakis, E. A., Soudry, D., Gao, Y., Machado, T. A., Merel, J., Pfau, D., Reardon, T., Mu, Y., Lacefield, C., Yang, W., Ahrens, M., Bruno, R., Jessell, T. M., Peterka, D. S., Yuste, R., and Paninski, L. (2016). Simultaneous Denoising, Deconvolution, and Demixing of Calcium Imaging Data. *Neuron*, 89(2):285–299.
- Polikov, V. S., Tresco, P. A., and Reichert, W. M. (2005). Response of brain tissue to chronically implanted neural electrodes. *Journal of neuroscience methods*, 148(1):1–18.
- Raabe, B. M., Artwohl, J. E., Purcell, J. E., Lovaglio, J., and Fortman, J. D. (2011). Effects of weekly blood collection in C57BL/6 mice. *Journal of the American Association for Laboratory Animal Science : JAALAS*, 50(5):680–685.

- Randlett, O., Wee, C. L., Naumann, E. A., Nnaemeka, O., Schoppik, D., Fitzgerald, J. E., Portugues, R., Lacoste, A. M. B., Riegler, C., Engert, F., and Schier, A. F. (2015). Whole-brain activity mapping onto a zebrafish brain atlas. *Nature Methods*, 12(11):1039–1046.
- Richards, K. L., Kurniawan, N. D., Yang, Z., Kim, T. H., Keller, M. D., Low, J., Ullmann, J. F. P., Cole, S., Foong, S., Galloway, G. J., Reid, C. A., Paxinos, G., Reutens, D. C., and Petrou, S. (2013). Hippocampal volume and cell density changes in a mouse model of human genetic epilepsy. *Neurology*, 80(13):1240–1246.
- Sakata, J. T. and Brainard, M. S. (2008). Online contributions of auditory feedback to neural activity in avian song control circuitry. *The Journal of neuroscience : the official journal of the Society for Neuroscience*, 28(44):11378–11390.
- Saxena, M., Eluru, G., and Gorthi, S. S. (2015). Structured illumination microscopy. *Advances in Optics and Photonics*, 7(2):241–35.
- Segev, E., Fowler, T., Faraon, A., and Roukes, M. L. (2015). Visible array waveguide gratings for applications of optical neural probes. In Hirschberg, H., Madsen, S. J., Jansen, E. D., Luo, Q., Mohanty, S. K., and Thakor, N. V., editors, *SPIE BiOS*, pages 93052L–6. SPIE.
- Segev, E., Reimer, J., Moreaux, L. C., Fowler, T. M., Chi, D., Sacher, W. D., Lo, M., Deisseroth, K., Tolia, A. S., Faraon, A., and Roukes, M. L. (2017). Patterned photostimulation via visible-wavelength photonic probes for deep brain optogenetics. *Neurophotonics*, 4(1):011002–16.
- Seymour, J. P. and Kipke, D. R. (2006). Fabrication of polymer neural probes with sub-cellular features for reduced tissue encapsulation. *Conference proceedings : ... Annual International Conference of the IEEE Engineering in Medicine and Biology Society. IEEE Engineering in Medicine and Biology Society. Annual Conference*, 1:4606–4609.
- Seymour, J. P. and Kipke, D. R. (2007). Neural probe design for reduced tissue encapsulation in CNS. *Biomaterials*, 28(25):3594–3607.
- Sitdikova, G., Zakharov, A., Janackova, S., Gerasimova, E., Lebedeva, J., Inacio, A. R., Zaynutdinova, D., Minlebaev, M., Holmes, G. L., and Khazipov, R. (2013). Isoflurane suppresses early cortical activity. *Annals of Clinical and Translational Neurology*, 1(1):15–26.
- Skocek, O., Bauer, T. N. x., Weilguny, L., Traub, F. M. x. n., Xia, C. N., Molodtsov, M. I., Grama, A., Yamagata, M., Aharoni, D., Cox, D. D., Golshani, P., and Vaziri, A. (2018). High-speed volumetric imaging of neuronal activity in freely moving rodents. *Nature Methods*, pages 1–9.

- Sober, S. J. and Brainard, M. S. (2009). Adult birdsong is actively maintained by error correction. *Nature Neuroscience*, 12(7):927–931.
- St-Pierre, F., Marshall, J. D., Yang, Y., Gong, Y., Schnitzer, M. J., and Lin, M. Z. (2014). High-fidelity optical reporting of neuronal electrical activity with an ultra-fast fluorescent voltage sensor. *Nature Neuroscience*, 17(6):884–889.
- Szarowski, D. H., Andersen, M. D., Retterer, S., Spence, A. J., Isaacson, M., Craighead, H. G., Turner, J. N., and Shain, W. (2003). Brain responses to micro-machined silicon devices. *Brain Research*, 983(1-2):23–35.
- Tervo, D. G. R., Hwang, B.-Y., Viswanathan, S., Gaj, T., Lavzin, M., Ritola, K. D., Lindo, S., Michael, S., Kuleshova, E., Ojala, D., Huang, C.-C., Gerfen, C. R., Schiller, J., Dudman, J. T., Hantman, A. W., Looger, L. L., Schaffer, D. V., and Karpova, A. Y. (2016). A Designer AAV Variant Permits Efficient Retrograde Access to Projection Neurons. *Neuron*, 92(2):1–12.
- Tischbirek, C., Birkner, A., Jia, H., Sakmann, B., and Konnerth, A. (2015). Deep two-photon brain imaging with a red-shifted fluorometric Ca²⁺-indicator. *Proceedings of the National Academy of Sciences*, 112(36):11377–11382.
- Tom, W. J., Ponticorvo, A., and Dunn, A. K. (2008). Efficient Processing of Laser Speckle Contrast Images. *IEEE Transactions on Medical Imaging*, 27(12):1728–1738.
- Tumer, E. C. and Brainard, M. S. (2007). Performance variability enables adaptive plasticity of ‘crystallized’ adult birdsong. *Nature*, 450(7173):1240–1244.
- Ünal-Çevik, I., Kılınc, M., Gursoy-Ozdemir, Y., Gurer, G., and Dalkara, T. (2004). Loss of NeuN immunoreactivity after cerebral ischemia does not indicate neuronal cell loss: a cautionary note. *Brain Research*, 1015(1-2):169–174.
- Vedaldi, A. and Fulkerson, B. (2008). VLFeat: An Open and Portable Library of Computer Vision Algorithms.
- Walton, C., Pariser, E., and Nottebohm, F. (2012). The Zebra Finch Paradox: Song Is Little Changed, But Number of Neurons Doubles. *Journal of Neuroscience*, 32(3):761–774.
- Wang, T., Wang, M., Feng, D. D., Horton, N. G., ndez, J. C. C.-H. a., Cheng, Y.-T., Reimer, J., Tolia, A. S., Nishimura, N., Ouzounov, D. G., and Xu, C. (2017). In vivo three-photon imaging of activity of GCaMP6-labeled neurons deep in intact mouse brain. *Nature Methods*, 14(4):1–5.
- Warden, M. R., Cardin, J. A., and Deisseroth, K. (2014). Optical Neural Interfaces. *Annual Review of Biomedical Engineering*, 16(1):103–129.

- Welkenhuysen, M., Andrei, A., Ameye, L., Eberle, W., and Nuttin, B. (2011). Effect of Insertion Speed on Tissue Response and Insertion Mechanics of a Chronically Implanted Silicon-Based Neural Probe. *IEEE Transactions on Biomedical Engineering*, 58(11):3250–3259.
- Winslow, B. D. and Tresco, P. A. (2010). Quantitative analysis of the tissue response to chronically implanted microwire electrodes in rat cortex. *Biomaterials*, 31(7):1558–1567.
- Wray, W. (2017). *Scalable Bundle Design for Massively Parallel Neuronal Recordings In Vivo*. PhD thesis, The Open University.
- Wu, F., Stark, E., Ku, P.-C., Wise, K. D., Buzsáki, G., and Yoon, E. (2015). Monolithically Integrated μ LEDs on Silicon Neural Probes for High-Resolution Optogenetic Studies in Behaving Animals. *Neuron*, 88(6):1136–1148.
- Xu, C., Zipfel, W., Shear, J. B., Williams, R. M., and Webb, W. W. (1996). Multiphoton fluorescence excitation: new spectral windows for biological nonlinear microscopy. *Proceedings of the National Academy of Sciences*, 93(20):10763–10768.
- Xu, N.-l., Harnett, M. T., Williams, S. R., Huber, D., O’Connor, D. H., Svoboda, K., and Magee, J. C. (2012). Nonlinear dendritic integration of sensory and motor input during an active sensing task. *Nature*, 492(7428):247–251.
- Yardeni, T., Eckhaus, M., Morris, H. D., Huizing, M., and Hoogstraten-Miller, S. (2011). Retro-orbital injections in mice. *Lab Animal*, 40(5):155–160.
- Yi, J. and Backman, V. (2012). Imaging a full set of optical scattering properties of biological tissue by inverse spectroscopic optical coherence tomography. *Optics letters*, 37(21):4443–4445.
- Yizhar, O., Fenno, L. E., Davidson, T. J., Mogri, M., and Deisseroth, K. (2011). Optogenetics in Neural Systems. *Neuron*, 71(1):9–34.
- Zong, W., Wu, R., Li, M., Hu, Y., Li, Y., Li, J., Rong, H., Wu, H., Xu, Y., Lu, Y., Jia, H., Fan, M., Zhou, Z., Zhang, Y., Wang, A., Chen, L., and Cheng, H. (2017). Fast high-resolution miniature two-photon microscopy for brain imaging in freely behaving mice. *Nature Methods*, 14(7):1–10.

CURRICULUM VITAE

